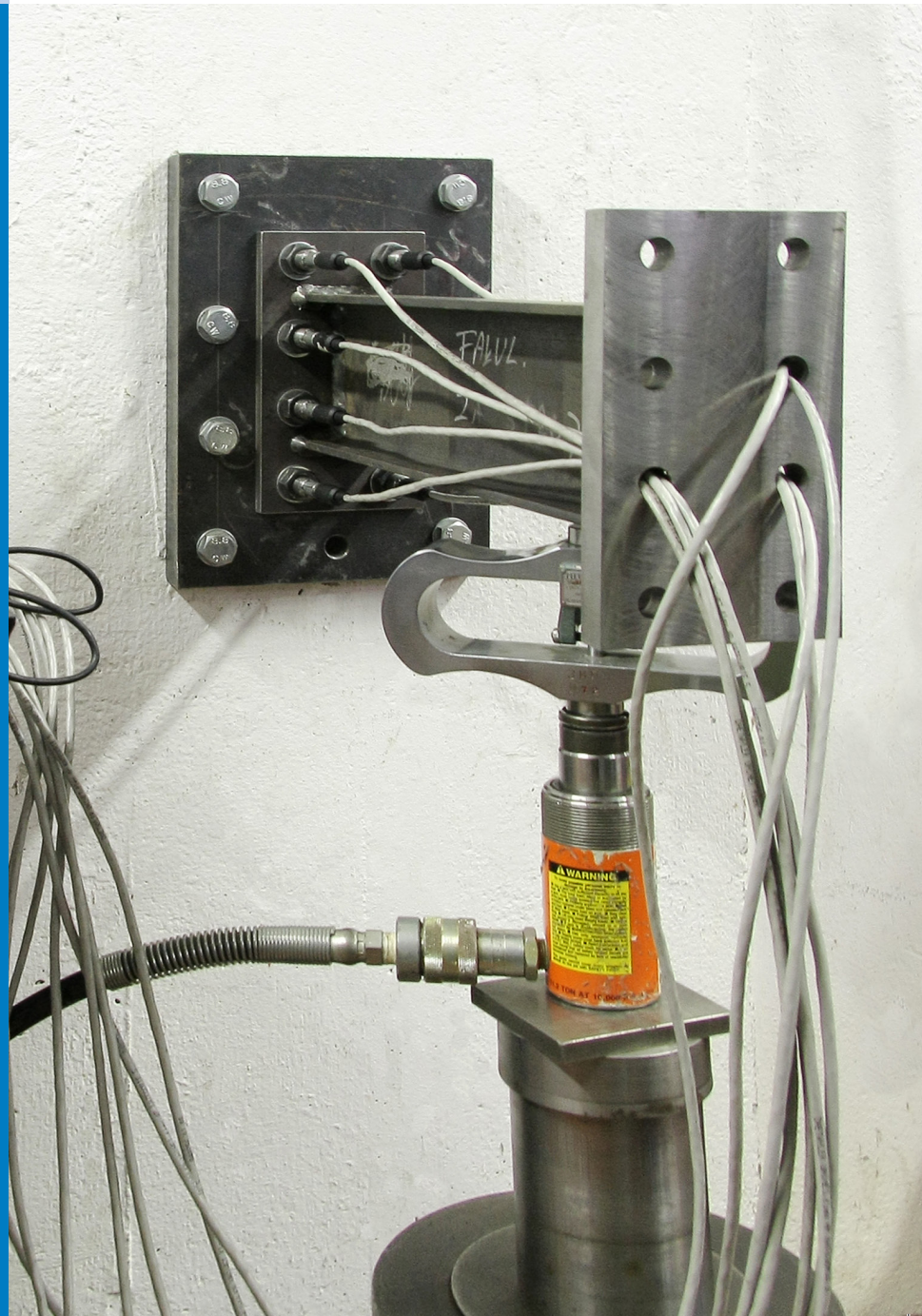




# Strojniški vestnik

## Journal of Mechanical Engineering



no. **11**  
year **2017**  
volume **63**

## Aim and Scope

The international journal publishes original and (mini)review articles covering the concepts of materials science, mechanics, kinematics, thermodynamics, energy and environment, mechatronics and robotics, fluid mechanics, tribology, cybernetics, industrial engineering and structural analysis.

The journal follows new trends and progress proven practice in the mechanical engineering and also in the closely related sciences as are electrical, civil and process engineering, medicine, microbiology, ecology, agriculture, transport systems, aviation, and others, thus creating a unique forum for interdisciplinary or multidisciplinary dialogue.

The international conferences selected papers are welcome for publishing as a special issue of SV-JME with invited co-editor(s).

## Editor in Chief

Vincenc Butala

University of Ljubljana, Faculty of Mechanical Engineering, Slovenia

## Technical Editor

Pika Škraba

University of Ljubljana, Faculty of Mechanical Engineering, Slovenia

## Founding Editor

Bojan Kraut

University of Ljubljana, Faculty of Mechanical Engineering, Slovenia

## Editorial Office

University of Ljubljana, Faculty of Mechanical Engineering  
SV-JME, Aškerčeva 6, SI-1000 Ljubljana, Slovenia

Phone: 386 (0)1 4771 137

Fax: 386 (0)1 2518 567

info@sv-jme.eu, <http://www.sv-jme.eu>

**Print:** Papirografika Bori, printed in 300 copies

## Founders and Publishers

University of Ljubljana, Faculty of Mechanical Engineering,  
Slovenia

University of Maribor, Faculty of Mechanical Engineering,  
Slovenia

Association of Mechanical Engineers of Slovenia  
Chamber of Commerce and Industry of Slovenia,  
Metal Processing Industry Association

## President of Publishing Council

Branko Širok

University of Ljubljana, Faculty of Mechanical Engineering, Slovenia

## Vice-President of Publishing Council

Jože Balič

University of Maribor, Faculty of Mechanical Engineering, Slovenia

## International Editorial Board

Kamil Arslan, Karabuk University, Turkey

Hafiz Muhammad Ali, University of Engineering and Technology, Pakistan

Josep M. Bergada, Polytechnical University of Catalonia, Spain

Anton Bergant, Litostroj Power, Slovenia

Miha Boltežar, UL, Faculty of Mechanical Engineering, Slovenia

Franci Čuš, UM, Faculty of Mechanical Engineering, Slovenia

Anselmo Eduardo Diniz, State University of Campinas, Brazil

Igor Emri, UL, Faculty of Mechanical Engineering, Slovenia

Imre Felde, Obuda University, Faculty of Informatics, Hungary

Janez Grum, UL, Faculty of Mechanical Engineering, Slovenia

Imre Horvath, Delft University of Technology, The Netherlands

Aleš Hribernik, UM, Faculty of Mechanical Engineering, Slovenia

Soichi Ibaraki, Kyoto University, Department of Micro Eng., Japan

Julius Kaplunov, Brunel University, West London, UK

Iyas Khader, Fraunhofer Institute for Mechanics of Materials, Germany

Jernej Klemenc, UL, Faculty of Mechanical Engineering, Slovenia

Milan Kljajin, J.J. Strossmayer University of Osijek, Croatia

Peter Krajnik, Chalmers University of Technology, Sweden

Janez Kušar, UL, Faculty of Mechanical Engineering, Slovenia

Gorazd Lojen, UM, Faculty of Mechanical Engineering, Slovenia

Thomas Lübben, University of Bremen, Germany

Janez Možina, UL, Faculty of Mechanical Engineering, Slovenia

George K. Nikas, KADMOS Engineering, UK

José L. Ocaña, Technical University of Madrid, Spain

Miroslav Plančak, University of Novi Sad, Serbia

Vladimir Popović, University of Belgrade, Faculty of Mech. Eng., Serbia

Franci Pušavec, UL, Faculty of Mechanical Engineering, Slovenia

Bernd Sauer, University of Kaiserslautern, Germany

Rudolph J. Scavuzzo, University of Akron, USA

Arkady Voloshin, Lehigh University, Bethlehem, USA

## General information

Strojniški vestnik – Journal of Mechanical Engineering is published in 11 issues per year (July and August is a double issue).

Institutional prices include print & online access: institutional subscription price and foreign subscription €100,00 (the price of a single issue is €10,00); general public subscription and student subscription €50,00 (the price of a single issue is €5,00). Prices are exclusive of tax. Delivery is included in the price. The recipient is responsible for paying any import duties or taxes. Legal title passes to the customer on dispatch by our distributor.

Single issues from current and recent volumes are available at the current single-issue price. To order the journal, please complete the form on our website. For submissions, subscriptions and all other information please visit: <http://en.sv-jme.eu/>.

You can advertise on the inner and outer side of the back cover of the journal. The authors of the published papers are invited to send photos or pictures with short explanation for cover content.

We would like to thank the reviewers who have taken part in the peer-review process.

The journal is subsidized by Slovenian Research Agency.

Strojniški vestnik - Journal of Mechanical Engineering is available on <http://www.sv-jme.eu>, where you access also to papers' supplements, such as simulations, etc.



### Cover:

The figure shows a dedicated test bench intended for analysing the prestressed bolt joint of the end-plate cantilever beam when an external bending load is applied.

### Image Courtesy:

Aleš Gosar, University of Ljubljana, Faculty of Mechanical Engineering, Slovenia

ISSN 0039-2480

© 2017 Strojniški vestnik - Journal of Mechanical Engineering. All rights reserved. SV-JME is indexed / abstracted in: SCI-Expanded, Compendex, Inspec, ProQuest-CSA, SCOPUS, TEMA. The list of the remaining bases, in which SV-JME is indexed, is available on the website.

## Contents

**Strojniški vestnik - Journal of Mechanical Engineering**  
**volume 63, (2017), number 11**  
**Ljubljana, November 2017**  
**ISSN 0039-2480**

**Published monthly**

### **Papers**

Simon Oman, Marko Nagode: Bolted Connection of an End-Plate Cantilever Beam: The Distribution of Operating Force	617
Jozef Kuczmaszewski, Ireneusz Zagorski, Olga Gziut, Stanislaw Legutko, Grzegorz M. Krolczyk: Chip Fragmentation in the Milling of AZ91HP Magnesium Alloy	628
Eyup Bagci, Ercüment U. Yüncüoğlu: The Effects of Milling Strategies on Forces, Material Removal Rate, Tool Deflection, and Surface Errors for the Rough Machining of Complex Surfaces	643
Jiangping Mei, Shenglong Xie, Haitao Liu, Jiawei Zang: Hysteresis Modelling and Compensation of Pneumatic Artificial Muscles using the Generalized Prandtl-Ishlinskii Model	657
Robert Panowicz, Marcin Konarzewski, Michał Trypolin: Analysis of Criteria for Determining a TNT Equivalent	666
Guohe Li, Yujun Cai, Houjun Qi, Meng Liu: Modelling of the Relationship of Adiabatic Shear and Cutting Conditions for Higher Cutting Speed Ranges	673



# Bolted Connection of an End-Plate Cantilever Beam: The Distribution of Operating Force

Simon Oman\* – Marko Nagode

University of Ljubljana, Faculty of Mechanical Engineering, Slovenia

*This paper presents an alternative method for calculating the operating forces on bolts in the bolted connections of the end-plate cantilever beams. Since operating force reduces pressure between the joined surfaces the influence of the operating force needs to be considered when determining the clamping force. Therefore, correctly defined operational force on each bolt is a base for all further calculations.*

*To evaluate proposed method, results of four existing analytical methods for calculating the operating forces in the bolted connections of the end-plate cantilever beams are compared with the results of the alternative method and the results gained by finite element analyses. Because finite element analysis take into account all influential parameters it is expected that the results obtained by finite element analyses are a good approximation to reality and can serve as a reference when comparing different analytical methods. It turns out that the results of the proposed method coincide with the results of finite element analyses the most. Only the proposed method correctly determines which bolts in the connection are subjected to the highest additional loads.*

**Keywords:** bolted connection; endplate connection; operating force; bolt pretension; structural steel; finite element method

## Highlights

- New method for calculating the distribution of operating forces on bolts is presented.
- Results gained by presented method coincide with the FEM analysis the most.
- Results were also confirmed by measurements of the actual forces in the bolts.
- The method, in contrast to existing analytical methods, correctly determines the most critical bolts for selected cases.

## 0 INTRODUCTION

Bolted connections of beams are very common joints in steel constructions. There are two basic bolted joint types that an engineer can use to connect two parts together: snug tight and prestressed joint. The two differences between these joints are the amount of mounting force achieved during installation, and the allowable movement between those surfaces in contact while in service. Since most steel constructions are dynamically loaded, prestressed joints are commonly used. In a prestressed joint, pressure between surfaces in contact and a coefficient of friction form a frictional force that prevents slippage. If no slippage is allowed, the frictional force in the worst load case has to be greater than a tangential force (i.e. a force occurring in a direction parallel to the joint surfaces) that appears as an outside load during operation. This is achieved by the proper determination of the clamping force (i.e. the mounting force of each bolt). For many prestressed joints a force component normal to the joint surfaces, the operating force, acts in addition to the tangential force (the operating force also being coincident with the axial direction of the bolts). This operating force reduces the pressure between the joined surfaces and hence reduces the sealing force [1] to [3] where the sealing force is the product of the pressure and the effective cross section. Consequently, the frictional

force is also reduced. Therefore the influence of the operating force needs to be considered when determining the clamping force [4]. For the end-plate cantilever beam discussed in this article (see Fig. 1), the joint is loaded with a tangential force and a normal force due to an applied bending moment. The difficulty in determining the necessary clamping force to prevent slippage occurs when estimating the distribution of the operating force across the bolts. The value of the operating force on each bolt is in fact dependent on many factors, particularly its location within the joint.

In practice several different analytical methods are currently used for calculating the operating forces in the bolted connections of the end-plate cantilever beams. All these methods are based on various assumptions, leading to diverse results. These methods are fundamentally different with respect to the assumed position of the neutral axis, which defines which bolts in the junction are more or less loaded due to the operating force. The first analytical method [5] is the simplest since it assumes that the neutral axis is located in the middle of the flange. It should be noted at this point that this method is appropriate only for flange connections of I-beams. The second method [6] sets the neutral axis at the lower edge of the flange and thus assumes all bolts are additionally loaded. The third method [7] assumes that the neutral

\*Corr. Author's Address: University of Ljubljana, Faculty of Mechanical Engineering, Aškerčeva 6, SI-1000 Ljubljana, Slovenia, simon.oman@fs.uni-lj.si

axis is positioned at a quarter of the flange height. The fourth method [8] sets the position of the neutral axis based on the thickness of the flange. It turns out that the fourth method [8] is the most accurate of the four, but even with this method the results may differ considerably from reality. With regard to the operating force the first method assumes it is equally distributed across the bolts above the neutral axis. The other three methods assume a linear distribution of the operating force across the bolts according to the distance from the neutral axis. Such a distribution would be possible only if the flange is absolutely rigid which in practice is simply not feasible. Therefore, we can conclude that these methods are very approximate and only the latter takes into account an additional parameter (the thickness of the flange) to determine the neutral axis position. However, we know that the actual distribution of the operating force across the bolts is mostly dependent on the bending stiffness of the flange, which is not constant due to the spot attachment via the bolts. Hence an alternative analytical method is presented here which accounts for this distribution of the operating force across the bolts.

where  $M$  is the bending moment at the beam-flange connection,  $F$  is the operating load in a tangential direction and  $r$  is the distance from the end of the beam to the point where the operating force is applied.

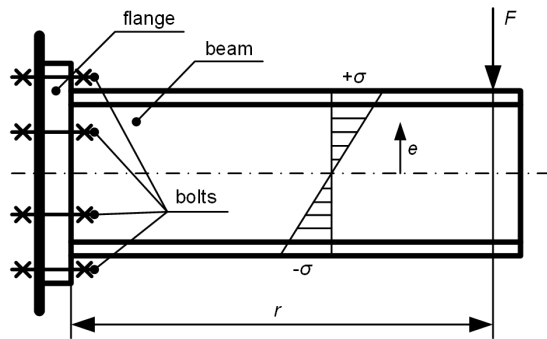


Fig. 2. Sketch of the end-plate cantilever beam

Theoretically normal stresses change from tension on one side of the beam to compression on the other, whilst remaining zero on the neutral axis. The stresses are calculated using the equation:

$$\sigma = \frac{M \cdot e}{I}, \tag{2}$$

where  $e$  is the distance from the neutral axis to the position of interest and  $I$  is the moment of inertia of the cross-section of the beam. In the next step, the normal stresses are converted into the total normal force separately for the tension and compression regions of the section. The total normal force is calculated using the equation:

$$F_N = \int_0^{e_{\max}} \frac{M \cdot e}{I} \cdot t \cdot de, \tag{3}$$

where  $e_{\max}$  is the distance from the neutral axis to the edge of the cross-section and  $t$  is the thickness of the cross-section. If the thickness of the cross-section is not constant, as is the case for an I-beam, Eq. (3) must be written separately for each thickness. The equation for calculating the total normal force in the case of an I-beam would be as follows:

$$F_N = \int_0^{e_1} \frac{M \cdot e}{I} \cdot t_1 \cdot de + \int_{e_1}^{e_2} \frac{M \cdot e}{I} \cdot (2 \cdot r + t_1 - 2 \cdot \sqrt{r^2 - (e - e_1)^2}) \cdot de + \int_{e_2}^{e_{\max}} \frac{M \cdot e}{I} \cdot t_2 \cdot de, \tag{4}$$

where  $t_1$  is the thickness of the beam web,  $t_2$  the width of the beam flange and  $r$  is the radius on the web-

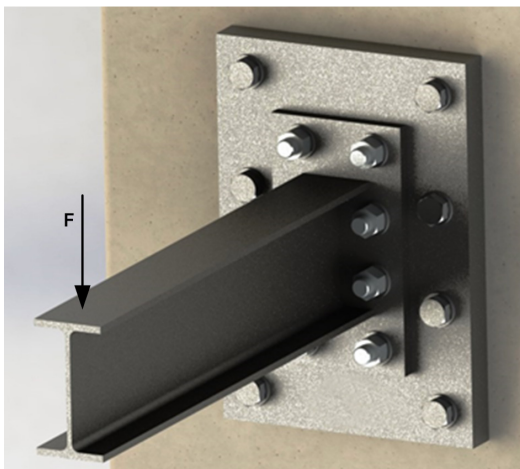


Fig. 1. Bolted connection of the end-plate cantilever beam

### 1 METHOD FOR CALCULATING THE OPERATING FORCE ON BOLTS

The idea of the method is as follows. First normal stresses in the beam at the connection with the flange (see Fig. 2) due to the applied bending moment are calculated. The bending moment is calculated using the equation:

$$M = F \cdot r, \tag{1}$$

flange connection. Further, the location of application of the total normal force has to be calculated separately for the tension and compression regions. The point of force application is calculated using the following equation:

$$M_R = F_N \cdot y \rightarrow y = \frac{M_R}{F_N}, \quad (5)$$

where  $y$  is the distance from the neutral axis to the point of the force application and  $M_R$  is the moment of one of the regions (tension or compression) calculated using the following equation:

$$M_R = \int_0^{e_{\max}} \frac{M \cdot e^2}{I} \cdot t \cdot de. \quad (6)$$

Once again the equation for calculation of moment needs to be applied separately to each section if the thickness of the cross-section is not constant. Knowing the values and the points of application of the total normal forces that actually represent the outside loads on the flange (see Fig. 3) the operating force on the bolts can be calculated. In the next step of the method it is assumed that the total tension force is distributed only across those bolts among which it is located. For the example shown in Fig. 3 this means the total tension force is distributed across the upper four bolts. It is further assumed that the distribution of the operating force across these four bolts depends on its vertical distance from the total normal force application point. For the example in Fig. 3 the operating force for the first line of the bolts can be calculated using the equation:

$$F_{O1} = \left( F_N \cdot \frac{a}{a+b} \right) / n_1, \quad (7)$$

where  $F_{O1}$  is the operational force on one bolt in the first line,  $a$  and  $b$  are distances of the bolt's location from the point of application of the total normal force (see Fig. 3), and  $n_1$  the number of bolts in the first line. For the second line the equation is as follows:

$$F_{O2} = \left( F_N \cdot \frac{b}{a+b} \right) / n_2. \quad (8)$$

Furthermore it is assumed that the total compression force is distributed across the remaining bolts. In Fig. 3 this means the total compression force is distributed across the lower four bolts. For compression, the normal force is transferred through the flange directly to that surface which the flange is connected to. Therefore the bolts are not additionally loaded but are relieved by an amount corresponding to the deformation (flattening) of the flange at the location of the bolt. Since bolts are

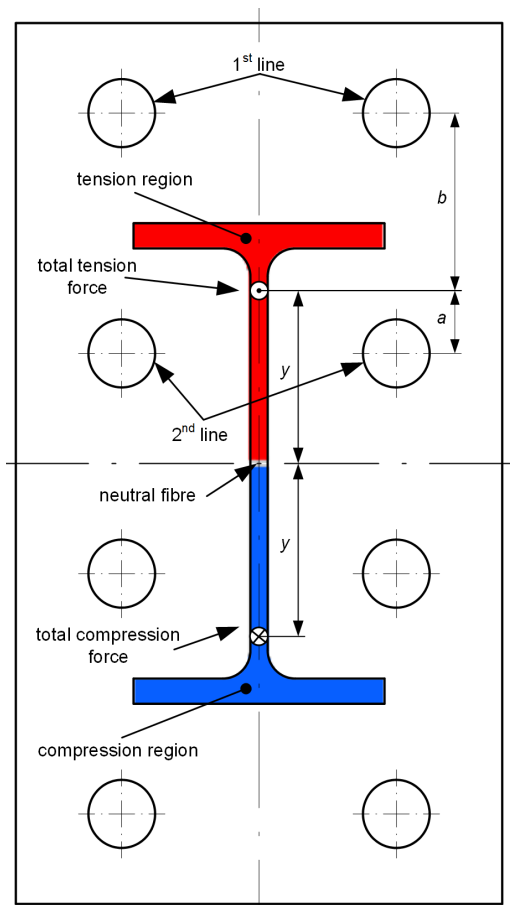


Fig. 3. Sketch of the normal forces acting on the flange

usually located more than one bolt diameter from the nearest point of the beam cross-section and the fact that the compression stiffness of the flange is high, the deformation of the flange around bolts located in the compression region is negligible. Consequently, the difference in total bolt load for all bolts in the compression region is also negligible. Therefore our method assumes that the clamping and thus the sealing force of the bolts in the compression zone does not change despite the action of the operational force, hence the initial prestressed state can be considered for all further calculations. The assumption that the total normal force is distributed only across those bolts among which it is located holds when the stiffness of the bolts compared to the bending stiffness of the flange is much higher. In this case the clamping force is selected so that, despite the action of the operational force, the surfaces in the bolt region remain in contact. Since the bolted connection of the end-plate cantilever beam is usually designed so as to prevent slippage the above mentioned conditions are normally fulfilled

and our assumptions are acceptable. The method here assumes that the neutral axis of the beam is located at the centre of mass of the beam cross-section. However, due to differences in bending stiffness of the flange in the tension and compression regions the neutral axis is shifted towards the total compression force. The reason for this is that in the compression region deformation of the flange is restrained over the whole surface by the surface to which it is fixed, whilst in the tension region the flange is restrained locally by the bolts. As a consequence the value and location of the total tension and compression forces also change. The neutral axis is located at the centre of mass only for cases where the flange is totally rigid which in reality is not possible. Therefore the neutral axis location is always slightly shifted. The value of this shift depends on numerous parameters such as the location of the bolts, flange thickness, flange material, the value of the clamping force and dimensions of the bolts, etc. To incorporate all of these parameters into a calculation would be a very demanding task that would not alter the results significantly as the shift of the neutral axis would be relatively small. Hence the proposed method, despite the assumption that the neutral axis is located at the centre of mass of the beam cross-section, gives better results than previous methods, as discussed in Section 3.

## 2 SIMULATION OF AN END-PLATE CANTILEVER BEAM BY THE FINITE ELEMENT METHOD

The stress strain state of the flange and bolts in the bolted connection of the end-plate cantilever beam is very hard to determine. Therefore, it is practically

impossible to take into account all the influential parameters when calculating the distribution of the operating force across the bolts using an analytical model. However using the finite element (FE) method all such parameters can be taken into account. For this reason, in past years, finite element models [9] to [14] have been largely applied to simulate structural elements and structures. Therefore it is expected that the results obtained by finite element analysis are a good approximation to reality and will serve as a reference when comparing the new analytical method with previous methods of calculation. All finite element analyses are performed using ABAQUS software.

### 2.1 Finite Element Model

To determine the distribution of the operating force across the bolts, the end-plate cantilever beam FE model (see Fig. 4) is composed of several parts: beam, flange, support plate, bolts, nuts and washers.

Plastic material properties are used to define the material characteristics of all the parts. For the beam, flange and support plate, construction steel S235 properties are used; for bolts, nuts and washers a quality of 10.9 with a yield strength of 900 N/mm<sup>2</sup> is assumed. The beam and the flange are connected together using a tie connection property. The flange is connected to the support plate by the prestressed bolts. Flange - support plate, support plate - washer and washer - nut contacts are simulated using frictional contacts with a coefficient of friction of 0.2. Bolt - nut and bolt - support plate connections are simulated as tie connections. In the first step of the analysis the

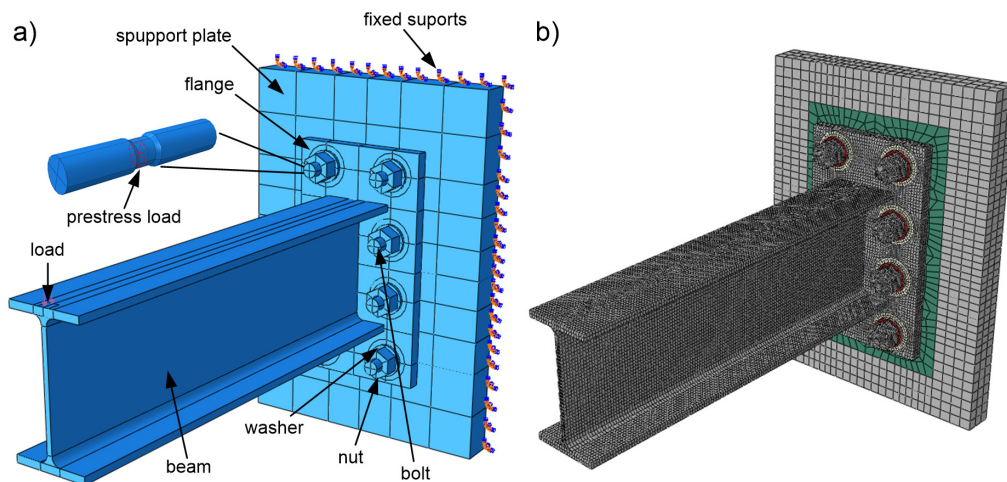
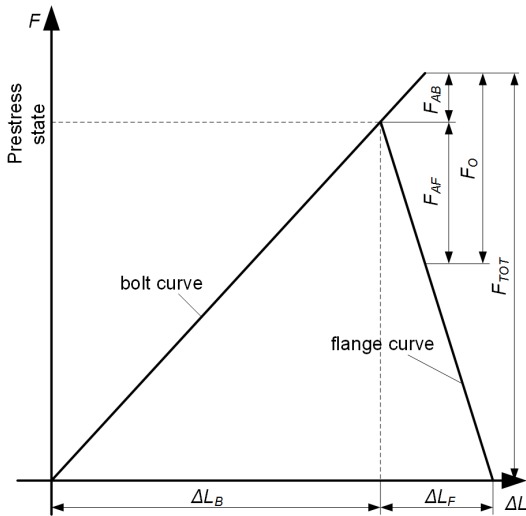


Fig. 4. Finite element model: a) parts, and b) mesh

prestress is applied to each bolt using the bolt load property. The value of the prestress is defined in such a way that prevents sliding between the connected surfaces, in this case 32 kN. In the second step, a 10 kN load is applied to the end of the beam in the vertical direction. The result of the analysis gives the additional load at each bolt. Since the bolted connection is a connection of two elastic elements the total operating force on the connection is divided into two parts. The first is the additional load on the bolt and the second is the relief of the flange. The value of each part depends on the ratio of the bolt and flange elasticity and a load application factor (see Fig. 5).



**Fig. 5.** Diagram of prestressed bolt joint ( $F_O$  operating force,  $F_{AB}$  additional bolt load,  $F_{AF}$  relief of the flange,  $F_{TOT}$  total or maximum bolt load,  $\Delta L_B$  bolt deformation at prestress state,  $\Delta L_F$  flange deformation at prestress state)

Assuming that the operating load is applied directly to the bolt head or nut, which means that the load application factor is 1, the total operating force can be calculated from the additional bolt load using the following equation [15]:

$$F_O = F_{AB} \cdot \frac{\delta_B + \delta_F}{\delta_F}, \quad (9)$$

where  $F_{AB}$  is the additional bolt load,  $\delta_B$  bolt elasticity and  $\delta_F$  flange elasticity. Bolt and flange elasticity can be calculated using Eqs. (10) to (11) [15].

$$\delta_B = \sum_{i=1}^n \delta_i + \delta_T + \delta_U + \delta_H + \delta_N = \frac{1}{E_B} \sum_{i=1}^n \frac{l_i}{A_i} + \frac{l_T}{A_T} + \frac{l_U}{A_3} + \frac{l_H + l_N}{A_d}, \quad (10)$$

$$\delta_F = \frac{2 \cdot \ln \left[ \frac{(d_w + d_h) \cdot (d_w + w \cdot l_k \cdot \tan \varphi - d_h)}{(d_w - d_h) \cdot (d_w + w \cdot l_k \cdot \tan \varphi + d_h)} \right]}{w \cdot E_F \cdot \pi \cdot d_h \cdot \tan \varphi}, \quad (11)$$

- $\delta_i$  [mm/N] Elasticity of those parts of the bolt with a constant cross-section  $A_i$
- $\delta_T$  [mm/N] Elasticity of the threaded part of the bolt
- $\delta_U$  [mm/N] Elasticity of the co-operating part of the bolt screwed into the nut
- $\delta_H$  [mm/N] Elasticity of the co-operating part of the bolt head
- $\delta_N$  [mm/N] Elasticity of the co-operating part of the nut
- $E_B$  [MPa] Young's modulus of the bolt
- $l_i$  [mm] Length of those parts of the bolt with a constant cross-section  $A_i$
- $l_T$  [mm] Length of the threaded part of the bolt between the bolt head and the nut
- $l_U$  [mm] Length of the co-operating part of the bolt screwed into the nut
- $l_H$  [mm] Length of the co-operating part of the bolt head
- $l_N$  [mm] Length of the co-operating part of the nut
- $A_T$  [mm<sup>2</sup>] Supporting cross-section of the thread
- $A_3$  [mm<sup>2</sup>] Size of the bolt thread core screwed into the nut
- $A_d$  [mm<sup>2</sup>] Nominal cross-section of the bolt
- $d_w$  [mm] Diameter of the bolt resting on the surface of the flange
- $d_h$  [mm] Diameter of the hole
- $w$  [/] Factor of the bolted connection type (here  $w = 2$ )
- $l_k$  [mm] Thickness of the flange
- $\varphi$  [°] Angle of the pressure cone under the bolt head
- $E_F$  [MPa] Young's modulus of the flange material

In order to facilitate the comparison of the results of FEM analyses with analytical methods, the results of the additional bolt load obtained by FEM analyses are converted into the operational force using Eq. (9) taking into account the elasticity of the bolts and flanges from Table 1.

**Table 1.** Bolts and flanges elasticity

Thickness of the flange $l_k$ [mm]	12	20
$\delta_B$ [mm/N]	$1.5243 \cdot 10^{-6}$	$8.7479 \cdot 10^{-8}$
$\delta_F$ [mm/N]	$1.7675 \cdot 10^{-6}$	$1.2353 \cdot 10^{-7}$

## 2.2 Finite Element Results

Finite element analyses of four combinations of beam shape and flange thickness were carried out. The results show that both parameters (beam shape and flange thickness) have an influence on the distribution of the operational force across the bolts.

This then means they also influence the location of the neutral axis that divides the tension and compression parts of the contact area between the beam and the flange. Theoretically the neutral axis is located at the centre of mass of the beam cross section, but this is only true when the flange on which the beam is connected to is rigid. In reality the neutral axis is moved towards the compression region due to differences in bending stiffness of the flange in regions of tension and compression (see Fig. 6a). The analyses also show that for an appropriate clamping force (i.e. the clamping force is sufficient to prevent slippage but not so high as to prevent plastic deformation of the bolts) there is no gap between the flange and the support plate around the bolts despite the application of the operating force (see Figs. 6b and c). Therefore only bolts in the tension region can be additionally loaded. From the deformation of the flange (see Figs. 6b and c) it is obvious that the bending stiffness of the flange is much smaller than the tensional stiffness of the bolts which is the main reason why the total operational force is distributed only across the bolts in the tension region. As said before, a linear distribution of the operational force across the bolts would only be possible if a very stiff flange were used. Because

of relatively large deformations of the flange (see Fig. 6b) the actual load on the affected bolts is not purely tensional but a combination of tension and bending. Therefore the distribution of the axial stress in the bolt cross-section is not symmetrical which is clearly visible in Fig. 7.

## 3 RESULTS AND DISCUSSION

The four existing analytical methods [5] to [8] presented in the introduction are compared to both the method presented in this paper and the FE analyses described in the previous section. The methods have been applied to four samples wherein the thickness of the flange and the shape of the beam are the changing parameters. The thickness of the flange is either 12 mm or 20 mm and either an IPE 120-beam or a custom T-beam is used. The dimensions of the flange, bolt positions and beam dimensions are shown in Fig. 8. The point of application of the vertical force is the same for all cases (400 mm from the support plate). To fix the beam to the support plate, specialised M16 bolts are used.

### 3.1 Comparison of Results

The results for each analytical method together with the FE analysis are shown in Table 2 and Fig. 9. Since the first method [5] is intended solely for flange joints of I-beams, the data for T-beam joints are not presented in the table. The results deviate quite a lot from each other. If the FE analysis is considered as a reference, it

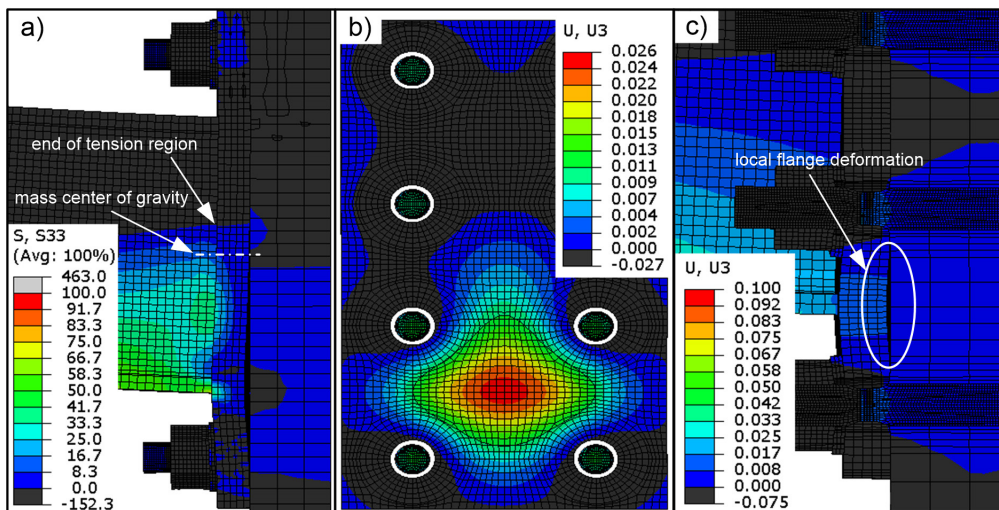
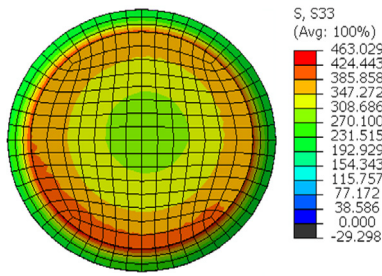


Fig. 6. Finite element analysis results for I-beam welded to the flange with a thickness of 12 mm:

- a) stresses in a normal direction to the joint surface,
- b) deformation of the flange in a normal direction to the joint surface,
- c) deformation of the flange and bolts in a normal direction to the joint surfaces



**Fig. 7.** Calculated stresses in a 2<sup>nd</sup> line bolt axial direction after a 10 kN load is applied to the end of the beam ( $F_O = 11163.5\text{ N}$ ,  $F_{AB} = 605.9\text{ N}$ ,  $\overline{S_{33}} = 343.1\text{ MPa}$ )

is obvious that the bolts in the 2<sup>nd</sup> line are subjected to the largest total operating force and not bolts in the 1<sup>st</sup> line as suggested by all four previous methods. This is clearly shown in Fig. 9 where the previous methods show deviations from the FE prediction for the second line of bolts, in some cases by over 100 %. However the new method presented here correctly identifies those bolts subjected to the highest loads. For the second line of bolts, only this method gives similar results to the FE analysis. Very similar experimental and finite element results were also gained by other researchers dealing with the pretensioned bolted end-plate connections [9], [13], [16] to [21]

Based on the results it can be concluded that the analytical method presented in this paper is the most accurate. Nevertheless these results do deviate slightly from the FE analysis but these deviations are acceptable. In particular, it is very difficult to determine how much the bolts in the compressional region are relieved. Since our method assumes that bolts in the compressional region stay at the clamping level even when an additional load is applied, there are some larger deviations compared to the results of FE analysis. Since all the bolts are usually dimensioned based on the one that is loaded the most and the most loaded bolt is always in the tensional region, this deviation does not have any critical meaning as far as safety is concern.

#### 4 EXPERIMENTS

In order to verify the results of the FE Analyses and the proposed analytical method, measurements of the actual forces in the bolts of bolted connections of end-plate cantilever beams were made. Measurements were performed on an IPE 120 beam welded to flanges of different thickness on each end (see Fig. 10). The flanged beam was connected to the support plate using eight pre-tensioned bolts with a clamping force of 32 kN ± 200 N. After pre-tensioning, an outside load of 10 kN was applied to the beam in a vertical direction.

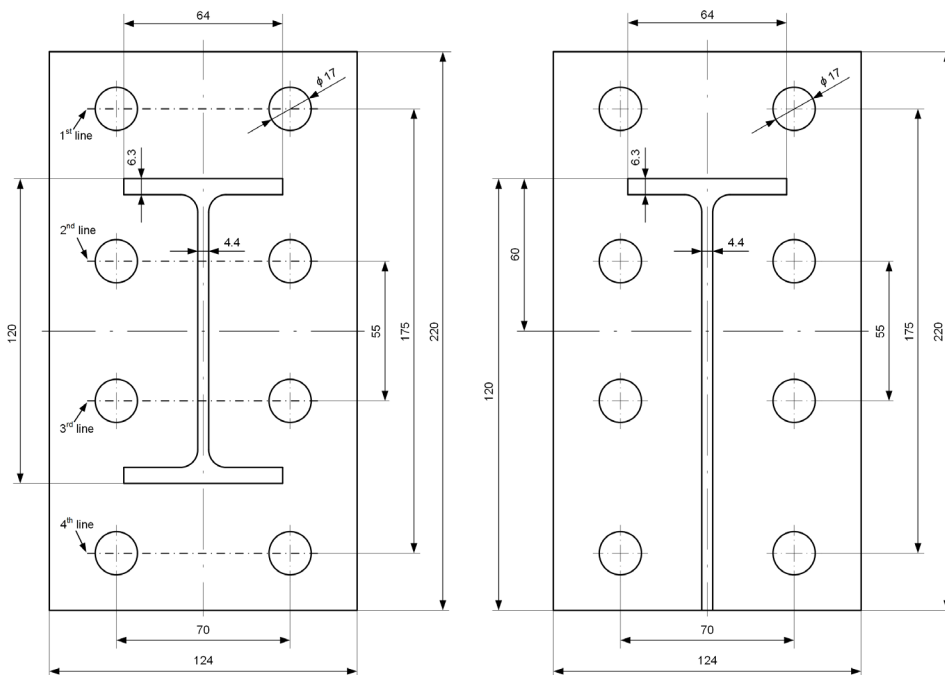


**Fig. 8.** Dimensions of the flanges and beams

**Table 2.** Comparison of the calculated operational force on bolts by different methods

Operational force [N] on bolts at:	Calculation method						
	Kržič	Hamrock	Matek	Aghayere	Oman	FEM Analysis	
Analysis 1: I-beam, flange thickness = 12 mm	1 <sup>st</sup> line	8795.1	6056.0	10226.5	7567.5	7670.4	8922.1
	2 <sup>nd</sup> line	8795.1	4216.2	5920.6	4650.3	10867.1	11163.5
	3 <sup>rd</sup> line	-8795.1	2529.7	1973.5	1976.2	0.0	-61.5
	4 <sup>th</sup> line	-8795.1	689.9	-2332.4	-940.9	0.0	-24.6
Analysis 2: I-beam, flange thickness = 20 mm	1 <sup>st</sup> line	8795.1	6056.0	10226.5	7567.5	7512.2	8761.2
	2 <sup>nd</sup> line	8795.1	4216.2	5920.6	4650.3	10643.0	10825.9
	3 <sup>rd</sup> line	-8795.1	2529.7	1973.5	1976.2	0.0	-1556.6
	4 <sup>th</sup> line	-8795.1	689.9	-2332.4	-940.9	0.0	-973.3
Analysis 3: T-beam, flange thickness = 12 mm	1 <sup>st</sup> line	NA	6056.0	10226.5	7567.5	6535.9	7196.7
	2 <sup>nd</sup> line	NA	4216.2	5920.6	4650.3	8982.4	8974.3
	3 <sup>rd</sup> line	NA	2529.7	1973.5	1976.2	0.0	212.6
	4 <sup>th</sup> line	NA	689.9	-2332.4	-940.9	0.0	279.9
Analysis 4: T-beam, flange thickness = 20 mm	1 <sup>st</sup> line	NA	6056.0	10226.5	7387.7	6401.1	6735.3
	2 <sup>nd</sup> line	NA	4216.2	5920.6	4615.3	8797.2	8134.1
	3 <sup>rd</sup> line	NA	2529.7	1973.5	2073.9	0.0	847.1
	4 <sup>th</sup> line	NA	689.9	-2332.4	-698.6	0.0	-677.4

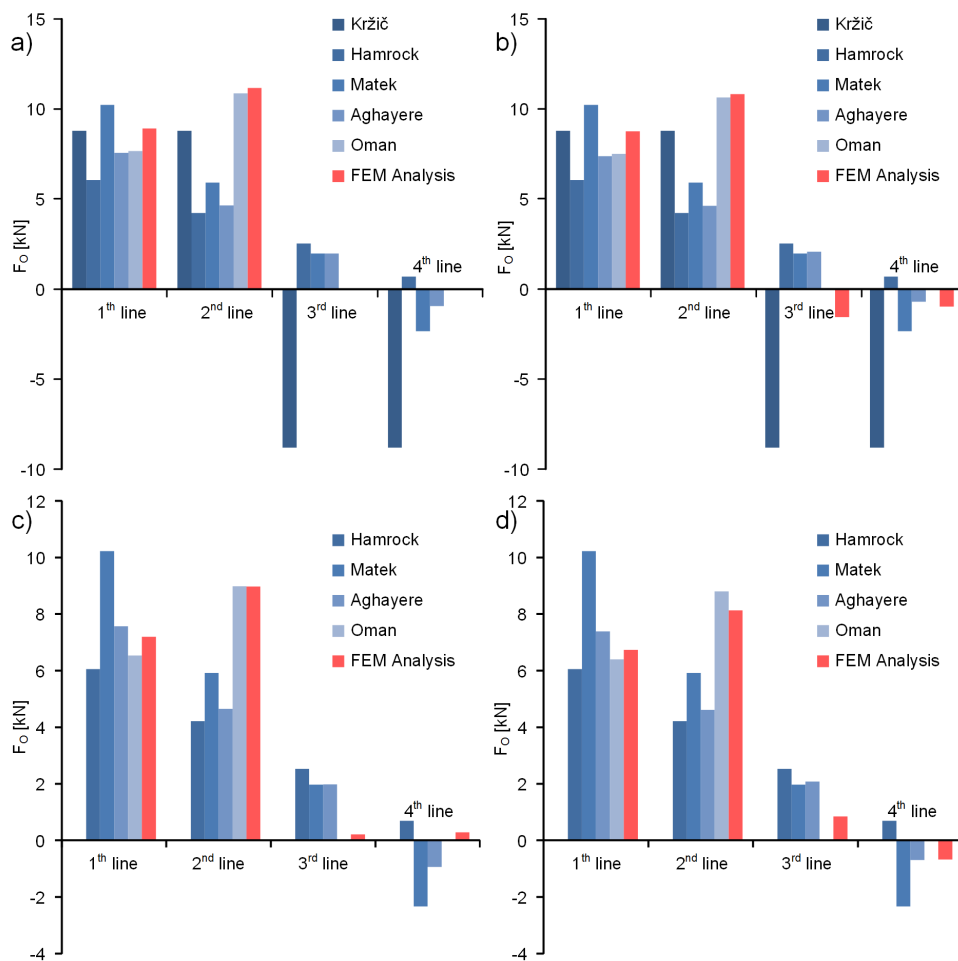


**Fig. 9.** Comparison of calculated operational force on bolts by different methods: a) I-beam with flange thickness of 12 mm, b) I-beam with flange thickness of 20 mm, c) T-beam with flange thickness of 12 mm, d) T-beam with flange thickness of 20 mm

The load was applied in the centre of the beam flange, 400 mm from the support plate. A difference in force (the additional force) in each bolt before and after application of an outside vertical force was thus obtained.



Fig. 10. Discussed cantilever beam with measurement and loading equipment

### 5.1 Measuring Equipment

Specially designed bolts equipped with strain gauges (see Fig. 11b) were used to measure the axial forces in the bolts. Strain gauges were connected in a half Wheatstone bridge circuit (see Fig. 11a) in order to compensate for bending loads [22] and [23]. Temperature was not compensated for since it was assumed that temperature does not change significantly over the duration of the measurement (the measurement lasts a few seconds). A National Instruments PXI-1033 amplifier equipped with NI PXI-4220 cards was used to perform the

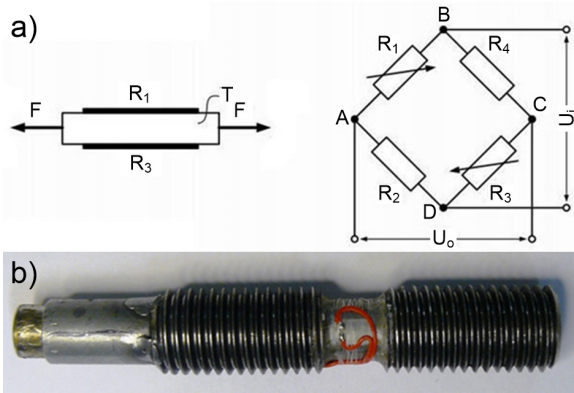


Fig. 11. Bolt equipped with strain gauges: a) strain gauge connection, b) specially designed bolt

measurements. It was controlled with a specially made application in Lab View that allows on-line monitoring and data acquisition.

Measuring sensors were calibrated over a range of 0 kN to 35 kN using a Schenk reference device. Based on the hysteresis loop of the calibration, the accuracy of the sensors and accumulated errors during a measurement were determined [24]. The accuracy is estimated as 1 % of the measuring range.

The vertical force on the beam was applied using a hydraulic valve. To measure the exact force, a load cell was installed between the hydraulic valve and the beam.

### 4.2 Experimental Results

Whilst reproducibility is poor, the overall result is very similar to the FE analysis. The additional load is mostly transferred to the bolts in the second line and a little less to the bolts in first line (see Fig. 12), while the force in the bolts in the third and fourth lines stays almost on the level of the clamping force.

During the measurements an interesting phenomenon was observed. When the additional force is applied to the beam for the first time (after pre-tensioning), the measurements of additional forces in bolts are significantly lower compared to those measurements taken when the additional force is applied for the second or more times (see Fig 12). This shows that the system somehow depresses when the force is applied for the first time and is afterwards stable.

Several conclusions have been drawn as to why the experimental results do not coincide completely with the results of FE analysis and are only poorly reproducible. Firstly, the estimated sensor accuracy is 1 % of its measuring range, the range here being approximately 35 kN. On the other hand, the maximum expected additional load of the bolt is around 450 N. Since the measured force is only slightly bigger than the estimated accuracy of 350 N, the measured values of the force are likely to have significant errors. Secondly, FE analysis shows that the additional load of the bolts is not purely tensional but a combination of tension and bending with a ratio of around 1:1. In principle this should not be a problem since the sensors were made to compensate for bending. This compensation is correct if the strain gauges are positioned ideally on the measuring sensor. However, it is not possible to place them in the ideal position, which means the sensors are somewhat sensitive to the bending. This can be shown by applying 5 Nm (i.e. the maximum expected value) of bending

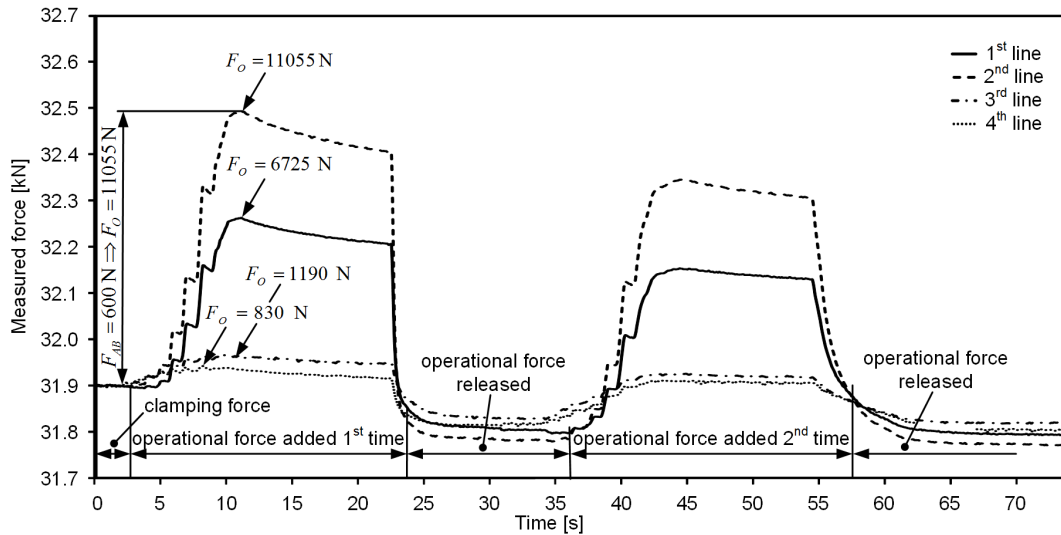


**Fig. 12.** Results of measured force on bolts during additional loading for flange thickness of 12 mm (measured force is an average of two bolts on each line)

moment on the sensors. When the bending moment is applied in a plane that crosses the strain gauge centre mark, the sensor registers 5 N and 80 N when applied perpendicular to the plane that crosses the strain gauges centre mark. Although the bolts were oriented to reduce the influence of bending moment on axial force measurements, this does contribute to errors. Based on the results and these facts it was concluded that experimental results are not very reliable and were therefore not used for a direct comparison with FE analyses and analytical methods. However, the results of the measurements are sufficiently accurate to determine which bolts take the largest share of the additional load, namely those bolts in the second line (see Fig. 12).

## 5 CONCLUSIONS

It turns out that previous methods dealing with specific prestressed bolt connections are not very accurate when calculating the operational force distribution across the bolts in the joint. Since the operational force influences the value of the sealing force and consequently the allowable tangential force at which no sliding appears in the contact, knowing the exact values of the operational forces on each bolt is very important. Therefore a new method for calculating the operating force across individual bolts for bolted connections of an end-plate cantilever beam is presented. The method is based on the following assumptions:

- the value of the clamping force is sufficient to prevent the formation of a gap between the connected surfaces around the bolts despite the action of the outside load,
- the bending stiffness of the flange is much lower than the axial stiffness of the bolts,
- the bending stiffness of the support plate is much higher than the bending stiffness of the flange.

If standards [4] and recommendations [3] for designing such joints are followed, all these assumptions are justified. Previous methods and the new method have been compared with FE analyses of such joints and the new method gives much more favourable results. Variations between the results of the FE analysis and the new method are due to numerous parameters e.g. bolt location, bolt dimension, bolt pre-tension, support plate stiffness, and geometrical ratios all of which have some influence on the actual operating force distribution but are not considered in the method as yet. Such parameters have an impact on the position of the neutral axis of the beam which separates the regions where tension and compression stresses appear. The neutral axis is shifted from its theoretical position because the bending stiffness of the flange is not the same in the tension and compression regions. This is due to complete support of the flange by the support plate in the compression region and only spotted supports by those bolts in the tension region. Deformation of the flange between the bolts is therefore allowed and is clearly visible in Fig. 6. As mentioned above this effect is not considered in

the new method to date although it should be noted that the effects on the results would only be minor.

The study also showed that bolts in the compression region do not affect the distribution of the operating force or additional force across the bolts in the tension region, because the operating force in the compression region is not transferred to the bolts but directly to the support plate. Therefore it can be assumed that bolts in the compression region remain at the level of the initial prestressing. In reality, these bolts are slightly relieved so consequently the sealing force on these bolts is actually slightly increased. In terms of movement between the connected surfaces the calculation gives conservative results if this assumption is considered.

## 6 ACKNOWLEDGMENTS

The research described in this paper was financially supported by the Slovenian Research Agency.

## 7 REFERENCES

- [1] Beg, D. (1999). *Design of Steel Structures According to ENV 1993-1-1, 2<sup>nd</sup> ed.*, University of Ljubljana, Faculty of Civil and Geodetic Engineering, Ljubljana.
- [2] Mott, R.L. (2006). *Machine Elements in Mechanical Design, 4<sup>th</sup> ed. in SI units*. Pearson Education South Asia, Singapore.
- [3] VDI 2230 Part1 (2003). *Systematic Calculation of High Duty Bolted Joints, Joints with One Cylindrical Bolt*. VDI – Verein Deutscher Ingenieure, Berlin.
- [4] DIN 2505-1 (1990). *Calculation of Flanged Joints*. Deutsches Institut für Normung E.V., Berlin.
- [5] Kržič, F. (1994). *Steel Structures 1*. University of Ljubljana, Faculty of Architecture, Civil and Geodetic Engineering, Ljubljana. (in Slovene)
- [6] Hamrock, B.J., Jacobson, B.O., Schmid, S.R. (1999). *Fundamentals of Machine Elements*, WCB/McGraw-Hill, Singapore.
- [7] Matek, W., Muhs, D., Witte, H., Becker, M., Roloff, H. (1995). *Roloff/Matek Maschinenelemente Braunschweig*. Vieweg & Sohn, Wiesbaden. (in German)
- [8] Aghayere, A. Vigil, J. (2009). *Structural Steel Design, A Practice-oriented Approach*, Pearson education, New Jersey.
- [9] Shi, G., Shi, Y., Wang, Y., Bradford, M.A. (2008). Numerical simulation of steel pretensioned bolted end-plate connections of different types and details. *Engineering Structures*, vol. 30, no. 10, p. 2677-2686, DOI:10.1016/j.engstruct.2008.02.013.
- [10] Díaz, C., Victoria, M., Martí, P., Querín, O.M. (2011). FE model of beam-to-column extended end-plate joints. *Journal of Constructional Steel Research*, vol. 67, p. 1578-1590, DOI:10.1016/j.jcsr.2011.04.002.
- [11] Drosopoulos, G.A., Stavroulakis, G.E., Abdalla, K.M. (2012). 3D finite element analysis of end-plate steel joints. *Steel and Composite Structures*, vol. 12, no. 2, p. 93-115, DOI:10.12989/scs.2012.12.2.093.
- [12] Wang, M., Shi, Y., Wang, Y., Shi, G. (2013). Numerical study on seismic behaviours of steel frame end-plate connections. *Journal of Constructional Steel Research*, vol. 90, p. 140-152, DOI:10.1016/j.jcsr.2013.07.033.
- [13] Saberi, V., Gerami, M., Kheyroddin, A. (2014). Comparison of bolted end plate and T-stub connection sensitivity to component thickness. *Journal of Constructional Steel Research*, vol. 98, p. 134-145, DOI:10.1016/j.jcsr.2014.02.012.
- [14] El-Khoriby, S., Sakr, A.M., Khalifa, T.M., Eladly, M.M. (2017). Modeling and behaviour of beam-to-column connections under axial force and cyclic bending. *Journal of Constructional Steel Research*, vol. 129, p. 171-184, DOI:10.1016/j.jcsr.2016.11.006.
- [15] Steinhilper, W., Sauer, B. (2012). *Konstruktionselemente des Maschinenbaus 1*, Springer - Verlag Berlin Heidelberg on, Berlin. (in German)
- [16] Bahaari, M.R., Sherbourne, A.N. (2000). Behavior of eight-bolt large capacity endplate connections. *Computers & Structures*, vol. 77, no. 3, p. 315-325, DOI:10.1016/S0045-7949(99)00218-7.
- [17] Shi, Y., Shi, G., Wang, Y. (2007). Experimental and theoretical analysis of the moment-rotation behaviour of stiffened extended end-plate connections. *Journal of Constructional Steel Research*, vol. 63, no. 9, p. 1279-1293, DOI:10.1016/j.jcsr.2006.11.008.
- [18] Abidela, A., Bouchair, A., Kerdal, D.E. (2012). Experimental and analytical behaviour of bolted end-plate connections with or without stiffeners. *Journal of Constructional Steel Research*, vol. 76, p. 13-27, DOI:10.1016/j.jcsr.2012.04.004.
- [19] Dessouki, A.K., Youssef, A.H., Ibrahim, M.M. (2013). Behavior of I-beam bolted extended end-plate moment connections. *Ain Shams Engineering Journal*, vol. 4, p. 685-699, DOI:10.1016/j.asej.2013.03.004.
- [20] Prinz, G.S., Nussbaumer, A., Borges, L., Khadka, S. (2014). Experimental testing and simulation of bolted beam-column connections having thick extended endplates and multiple bolts per row. *Engineering Structures*, vol. 59, p. 434-447, DOI:10.1016/j.engstruct.2013.10.042.
- [21] Katula, L., Dunai, L. (2015). Experimental study on standard and innovative bolted end-plate beam-to-beam joints under bending. *Steel and Composite Structures*, vol. 18, no. 6, p. 1423-1450, DOI:10.12989/scs.2015.18.6.1423.
- [22] Hoffmann, K. (1987). *An Introduction to Measurements using Strain Gages*, Hottinger Baldwin Messtechnik GmbH, Darmstadt.
- [23] Hoffmann, K. (1989). *Applying the Wheatstone Bridge Circuit*, Hottinger Baldwin Messtechnik GmbH, Darmstadt.
- [24] Holman, J.P. (2007), *Experimental Methods for Engineers, 7<sup>th</sup> ed.*, McGraw-Hill, Auckland.

# Chip Fragmentation in the Milling of AZ91HP Magnesium Alloy

Jozef Kuczmaszewski<sup>1</sup> – Ireneusz Zagorski<sup>1</sup> – Olga Gziut<sup>1</sup> – Stanislaw Legutko<sup>2</sup> – Grzegorz M. Krolczyk<sup>3,\*</sup>

<sup>1</sup> Lublin University of Technology, Faculty of Mechanical Engineering, Poland

<sup>2</sup> Poznan University of Technology, Faculty of Mechanical Engineering and Management, Poland

<sup>3</sup> Opole University of Technology, Faculty of Mechanical Engineering, Poland

*This paper presents new approaches to safety assessment in the milling of magnesium alloy. The objective of the study is to determine the effect of milling parameters and end mill geometry on machining safety, defined as the minimum probability of chip self-ignition. The assessment of safety and effectiveness in the milling of magnesium must include analysis of chip fractions formed during the milling process. The paper presents the state of the art of magnesium alloy machinability in terms of chip formation (chip fragmentation). Furthermore, the paper investigates the correlation between the quantity of distinguished chip fractions and variations in the parameters  $v_c$  and  $f_z$  as well as in the rake angle  $\gamma_o$ . In addition, the results of the dimensions of individual chip fractions are reported. The study was conducted on AZ91HP magnesium cast alloy, and the milling process was performed using carbide tools with varying rake angles ( $\gamma_o = 5^\circ$  and  $\gamma_o = 30^\circ$ ). It has been found that chip fragmentation increases by increasing the above parameters, i.e. the feed rate  $f_z$  and the cutting speed  $v_c$ . The observed chip fragmentation (the quantity of chip fractions) is lower at the tool rake angle  $\gamma_o = 30^\circ$ . Finally, technological recommendations are formulated based on the quantity of chip fractions generated at particular settings. The results do not unequivocally demonstrate that chip dimensions increase or decrease by increasing the operational parameters of the milling process. In terms of their application, it is vital that machining processes be simultaneously effective and safe.*

**Keywords:** high-speed dry milling, magnesium alloys, machinability, magnesium chips, end-mill geometry

## Highlights

- Chip shape and number of fractions of magnesium alloys has been analysed.
- Chips formed during AZ91HP magnesium cast alloy milling for selected chip fractions have been evaluated and analysed.
- Effect of technological parameters on the chip length has been determined.
- Effect of technological parameters on the chip width has been examined.

## 0 INTRODUCTION

Magnesium alloys are light metals that have attracted the interest of engineers in recent years [1] and [3]. Due to its low density, magnesium is widely used in the automotive and aerospace industry [4]. In addition to obvious advantages, such as low weight, the advantages of this metal included the wide availability of magnesium alloys [5] and good machining properties in comparison to other structural materials. However, chips formed during the machining of magnesium alloys might pose a serious threat and lead to uncontrollable ignition. The risk of magnesium ignition occurs when the temperature reaches 450 °C, whereas the danger of imminent explosion occurs when magnesium particles (chips) of a size lower than 500 µm are generated during the milling process [6]. In addition, magnesium alloys react with water to form magnesium oxide and hydrogen, which makes them potentially explosive [7]. It is, therefore, recommended to avoid the use of water-based cutting fluids in the machining of magnesium [8]. During the dry high-speed cutting of magnesium, thin and light chips are produced [9]. These kinds of chips are prone to cause ignition because of low heat capacity and high

thermal expansion [10]. Moreover, dust chips forming during milling has a detrimental effect on machine elements such as bearings or guide ways; therefore, it is necessary to develop a milling technology which can ensure controlled chip fraction formation. At present, magnesium alloy machining is often done by modern high-speed machining technologies, such as HSM, HPC, and HSC. These technologies enable, among others, shorter machining time and lower production of non-deformed chips, which reduces the amount of heat transferred to the element being machined (heat generated in machining is removed with chips) [11]. In HSM, the tribological conditions influence the wear mechanisms, dramatically reducing tool life [12] and [13].

An important part of machining is the process of chip formation [14]. There are several factors essential for machining process safety, including temperature in the cutting area, quantity of chip fractions generated during milling, chip morphology, shape and mass of chips, thermal deformation, or heat marks on the surface of chips, ignition initiation analysis at low depths of cut, and the ignition point of a given type of Mg alloy. Due to practical reasons, surface roughness is often examined [15] and [16], both on the end face

and lateral surface after end milling. Moreover, when producing innovative (biodegradable) elements made of magnesium alloys, e.g. from the Mg-Ca group [17], particular attention should be paid to the final quality of the machined surface. The improvement of surface quality is an important industrial task because it has direct influence on the performance and tribological properties of product [18] and [19]. Regarding changes in the cutting parameters such as cutting speed and depth of cut, the application of the PKD end mill produces a roughness parameter  $Ra$ , which is equal to about 0.5  $\mu\text{m}$ . Researchers have also investigated the cutting forces that are directly correlated with temperature in the cutting area.

Regarding the theoretical considerations (for the purposes of modelling the milling process), it is necessary to determine non-deformed chip thickness. The classical model of chip thickness assumes a cylindrical tool path. Li et al. [20] proposed a new approach to the determination of non-deformed chip thickness during milling. By analysis of the real trajectory of the end mill (trochoid tool path), a real momentary non-deformed chip thickness can be defined by solving the so-called deduced transcendental equation. Instead of a numerical method, it is possible to develop the function into a Taylor's series, which ensures higher accuracy compared to the traditional method. Errors (resulting from the application of the traditional method) are related with the number of end mill teeth, feed per tooth and machining tool diameter.

Sai et al. [21] proposed the modelling of non-deformed chip thickness with respect to end mill trajectory by circular (not linear, as previously) interpolation. During the circular trajectory of tool motion, chip thickness increases with a decrease in the radius of motion trajectory. This phenomenon can have both thermal and mechanical impact, which can, in turn, affect the roughness of the surface being machined.

The problems of non-deformed chip thickness, tool flank temperature, and partial melting of edges in Mg alloy chips were also investigated by Fang et al. [22]. They found that an increase in the cutting forces results in a higher thickness of deformed chips. When the non-deformed chip thickness decreases, the shear angle decreases too, leading to an increase in the temperature in the shear plane. The proposed method for measuring temperature (using k-type thermocouples) enables the measurement of the so-called "mean temperature of tool flank". Both in turning and milling, attempts were made to control chips in order to produce chips which are not easily

flammable. The studies [23] and [24] report ignition in the milling of magnesium alloys (AM50A, AZ91D) at a very small depth of cut  $a_p$ , ranging from several  $\mu\text{m}$  to several hundred  $\mu\text{m}$ . During these cutting tests, sparks, flares, and rings of fire were observed. Although the depth of cut of 1  $\mu\text{m}$  to 80  $\mu\text{m}$  applied in [25] is not generally used in the industry, the results provide significant insight into the problem. Chip ignition is hindered by increasing Al content, particularly when combined with an increase in small depths of cut and higher cutting speeds. Given that sparks or flares (hence, chip ignition) occur at lower cutting speeds and feed per tooth, ignition risk can be controlled by changing depth of cut, cutting speed and feed per tooth [26].

An interesting parameter connected with machining safety is the so-called ignition point of a given grade of magnesium alloy. Lin et al. [27] investigated the effect of cerium (Ce) and aluminium (Al) on the ignition point and oxidation resistance of magnesium alloys. The highest ignition temperatures were, respectively, 535 °C for AM50 alloy and 525 °C for AZ91D alloy for 0.25 wt.% Ce. Zhou et al. [28] investigated the effect of Ce addition and the effect of particle (chip) size on the ignition point of Mg alloy AZ91D. It was found that the cerium content has a stronger impact on the ignition point than the particle size does. The content of Ce changed in the range 0.15 wt.% to 0.45 wt.%. The particle size was 58  $\mu\text{m}$  to 270  $\mu\text{m}$ . The lowest ignition temperature (ignition point) was observed for 0.25 wt.% of Ce; it was about 525 °C for the particle size of about 150  $\mu\text{m}$ . In contrast, according to Liu et al. [29], the ignition point for popular magnesium alloys: WE43, AZ31 and AZ91, is 644 °C for WE43, 628 °C for AZ31 and 600 °C for AZ91, respectively. However, the ignition temperature significantly depends on experimental details. Ravi Kumar et al. [30] also investigated the ignition resistance of pure Mg and its two alloys: AZ91 and WE43. The resistance to ignition (oxidation) depends on the presence of yttrium (Y), which affects the so-called ignition point. Ignition resistance depends on factors such as specimen geometry, as a large specimen surface can promote ignition. The specimens were subjected to induction heating, and the temperature was measured with a thermocouple. The ignition of WE43 alloy was not observed until 750 °C. The ignition point of pure Mg was about 630 °C, while that of AZ91 alloy was about 580 °C to 590 °C.

The chips formed during milling can be classified according to the criteria established in the ISO 3685:1993 standard. This classification

should, however, serve only as an example because the number of potential chip shapes is virtually infinite [31]. Chip fragmentation depends to a certain extent on each milling parameter. An undesirable impact of an increased quantity of intermediate chip fractions formed during milling can be observed at increasing  $f_z$  and decreasing  $a_p$ , as well as under the conditions of excessive increase in the cutting speed  $v_c$  [32]. Magnesium alloys can also be used as orthopaedic materials and biomaterials (Mg-Ca alloys) for the production of implants. Clinical tests on the biocompatibility of Mg-Ca alloys produced very interesting results. It was found that these alloys do not generate any toxic, carcinogenic, or mutagenic products, so they can be freely used from a physiological point of view. Salahshoor and Guo in [33] investigated the milling and burnishing of an MgCa0.8 alloy. They examined the effect of technological parameters on surface roughness, microhardness, microstructure and stresses after machining. Furthermore, the authors [17] investigated the formation of flank build-up (FBU), lamellas and (using the FEM method) chip temperature in milling. The temperature expected on the tool-chip contact surface can be close to the melting point ( $\sim 650$  °C) for MgCa0.8 alloy. Magnesium alloys have a distinctive morphology, as they are of a lamellar structure on one side, while the other side of their surface is smooth and shiny due to chip-tool contact.

Aside from conventional machining methods, such as milling, it is often necessary to perform the finishing of part edges made of Mg and Al alloys, e.g. by wire brushing. Wire brushing parameters must be selected to ensure effective removal of burrs, formation of the required edge, and shaping of the required surface layer properties. The authors of the study [34] investigated the state of edges (corner radius) and surface roughness of the edges.

Factories producing parts for aircraft or car manufacturers constantly demand increased manufacturing effectiveness, which cannot be achieved without intensification of technological parameters of machining (predominantly  $v_c$  and  $f_z$ ). The production of the majority of such elements is aided by milling. Dynamic advances in the field of manufacturing and constant development of machinery, e.g. machine tools (machining centres) and cutting-edge machining tools, ensure high milling speed, high feed rate, and high-quality surface finish at the same time. Therefore, it appears vital to search for the most beneficial solutions which would provide excellent surface roughness and effectiveness, without compromising process safety. The key factors ensuring the safety in milling are: size, mass, shape, dimensions, and quantity of formed chips.

## 1. METHODOLOGY, OBJECTIVE, AND SCOPE OF THE RESEARCH

This study predominantly consists of an analysis of selected technological parameters,  $v_c$  and  $f_z$ , and effect on the risk of chip ignition as defined by the analysed indicators. Establishing a suitable relation between the parameters in question is of paramount importance towards attaining superior effectiveness and safety of the machining process. The secondary objective of the study is to analyse chip fractions formed during the milling of magnesium alloys. Fig. 1 shows a plan of the experiments performed by tools of varying cutting-edge geometry (different tool rake angle  $\gamma_o$ ).

A schematic diagram of the experimental set-up is shown in Fig. 2a. The main aim of the experiment was to determine safe yet effective technological parameters of a down-milling process. Fig. 2b shows an example image of a chip with its dimensions. These dimensions are, in fact, orthogonal projections

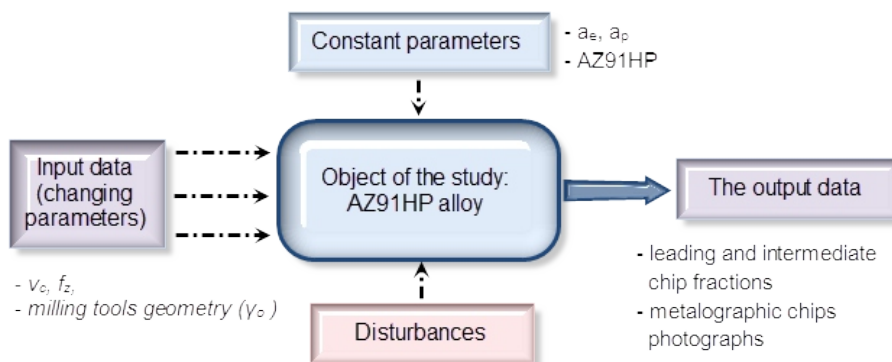


Fig. 1. Design of the experiment for determination of impact of  $v_c$ ,  $f_z$  and  $\gamma_o$  on chip form

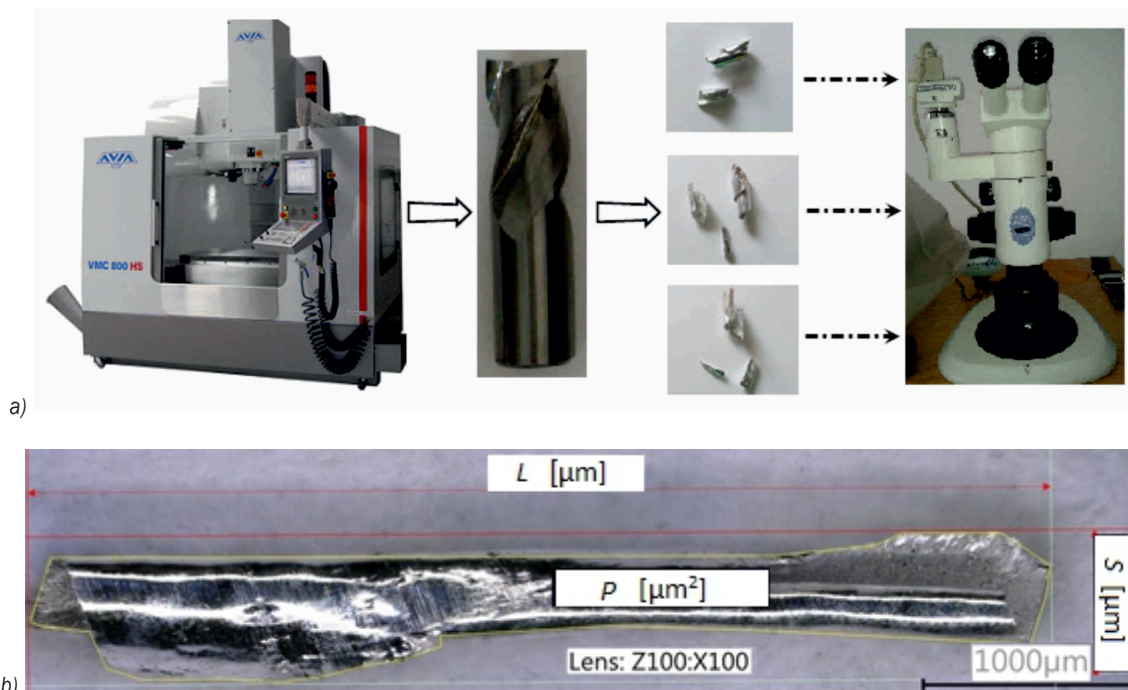


Fig. 2. Schematic diagram of the: a) experimental set-up, b) chip dimensions

Table 1. Cutting conditions in the experiment

No	$f_z$ [mm/tooth]	$v_c$ [m/min]	$n$ [rev/min]	$v_f$ [mm/min]	$a_p$ [mm]	$z$	$a_e$ [mm]
1	0.15	400	7958	3581	6	3	14
2		800	15915	7162			
3		1200	23873	10743			
4	0.05	800	15915	2387			
5	0.15			7162			
6	0.3			14324			

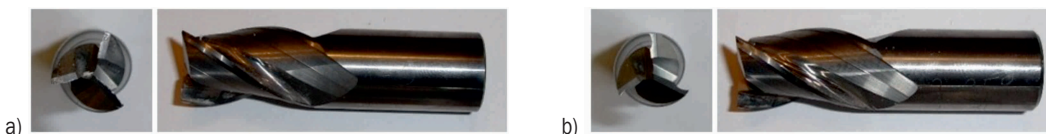


Fig. 3. Three-tooth carbide end mill described by angle: a)  $\gamma_0 = 5^\circ$ , b)  $\gamma_0 = 30^\circ$

of the chip onto the plane. To simplify the description, however, hereinafter the following terms are used: chip length  $L$ , chip width  $S$  and chip area  $P$ .

The research was performed on an Avia VMC800HS vertical machining centre. The following constant cutting conditions were applied: radial depth of cut  $a_e = 14$  mm, axial depth of cut  $a_p = 6$  mm. The variable technological parameters of the milling process examined in the study included:  $f_z = 0.05$  mm/tooth to 0.3 mm/tooth,  $v_c = 400$  m/min to 1200 m/min, and the rake angle  $\gamma_0 = 5^\circ$  to  $30^\circ$ . Table

1 lists the ranges of parameters applied during the milling of AZ91HP.

For the purpose of description, the following definitions are applied:

- *fraction* – a population of elements of a particular size or dimensions,
- *fragmentation* – formation of an intermediate chip fraction of different shape and mass during machining, alongside the leading (prevailing and characteristic) fraction.

The tests were conducted on AZ91HP magnesium cast alloy. Carbide tools with varying rake angles are

shown in Fig. 3. The tool used was a 16 mm carbide end mill.

The tests were conducted for the above technological parameters of milling. The division into the leading and intermediate fractions was based on the shape and size of chips, Fraction A being the biggest and Fraction D the smallest. The term “leading fraction” was ascribed to Fraction A, while smaller fractions were referred to as ‘intermediate fractions’. Furthermore, the tests provided information about the percentage of a particular chip fraction at different cutting speeds  $v_c$  and feed rates  $f_z$ . The point of reference for the chip fraction division was provided by the Polish Standard PN ISO 3685:1996, which is a classification originally referring to the turning of steel.

The first step of chip fraction division involved selecting a leading fraction based on chip shape. The leading fraction had the highest unit mass and was the most representative in terms of quantity. Next, other intermediate chip fractions were selected (also based on their shape). Moreover, the intermediate fraction was defined in two ways: as a fraction with a different shape (compared to that of the leading fraction or the preceding intermediate fraction) and as a fraction with a lower mass (in most cases) by about 50 % of that of the leading fraction or the preceding intermediate chip fraction.

## 2 RESULTS AND DISCUSSION

Table 2 shows the impact of the cutting speed  $v_c$  on the form of chips and the quantity of chip fractions distinguished in set conditions at the cutting tool rake angle  $\gamma_o = 5^\circ$ . At the cutting speed  $v_c = 400$  m/min, two chip fractions were determined, whereas three fractions can be observed at the speeds of  $v_c = 800$  m/min and  $v_c = 1200$  m/min. The shape of chips categorized as Fraction B (cutting speed  $v_c = 400$  m/min) was described as loose arc, and Fraction A chips were described as short conical helical and, similarly to Fraction A, they were produced at  $v_c = 800$  m/min. Fractions B and C consisted of loose arc chips, however, in the case of Fraction C the chips were tighter, which was not the only difference, as they also differed in terms of the size. At the cutting speed  $v_c = 1200$  m/min, loose arc chips were observed (Fraction B and C) along with short tight tubular chips.

Fig. 4 shows the percentage of particular chip fractions at different cutting speeds.

At the lowest cutting speed, two chip fractions were distinguished, with A being the leading one with a 79 % share of the total percentage of chips. In the case of the two other cutting speed values, A was also the leading fraction, containing the largest chips. The percentage of smaller fractions in the examined cases was also similar. Fraction B (arc chips), which amounted to 21 % at  $v_c = 400$  m/min and increase

**Table 2.** Impact of cutting speed on chip shape and quantity of fractions (AZ91HP magnesium cast alloy):

a)  $v_c = 400$  m/min, b)  $v_c = 800$  m/min, c)  $v_c = 1200$  m/min, at  $f_z = 0.15$  mm/tooth,  $a_p = 6$  mm and  $\gamma_o = 5^\circ$

Fraction $v_c$ [m/min]	Fraction				
	All fractions	Leading fraction A	Intermediate fraction B	Intermediate fraction C	Intermediate fraction D
a) $v_c = 400$ m/min				no fraction detected	no fraction detected
b) $v_c = 800$ m/min					no fraction detected
c) $v_c = 1200$ m/min					no fraction detected

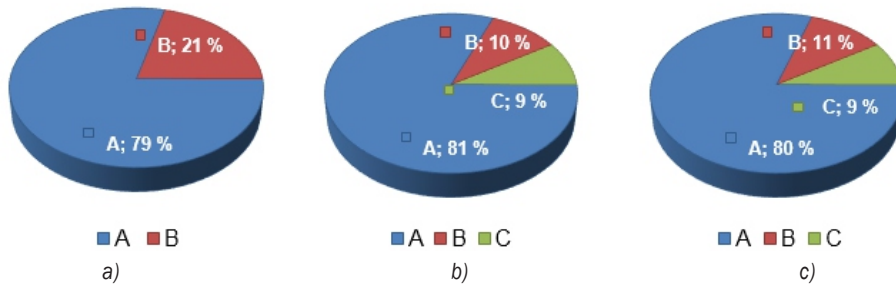


Fig. 4. Percentage of particular chip fractions versus cutting speed in the milling of AZ91HP magnesium alloy at carbide tool rake angle  $\gamma_0 = 5^\circ$

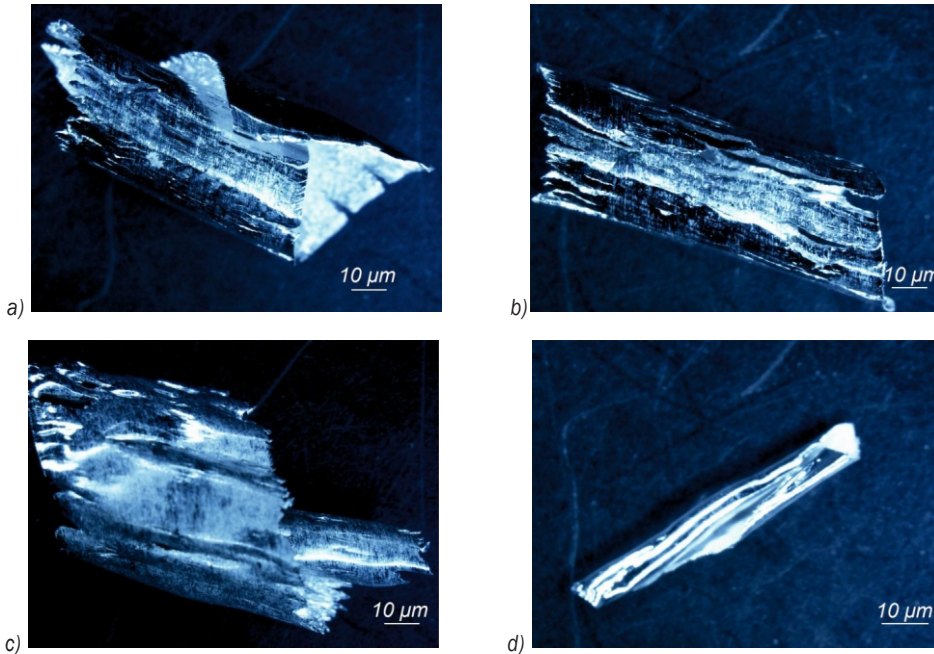


Fig. 5. Chips formed during AZ91HP magnesium cast alloy milling for selected chip fractions and different cutting speeds  $v_c$ : a)  $v_c = 400$  m/min, Fraction A, b)  $v_c = 400$  m/min, Fraction B, c)  $v_c = 1200$  m/min, Fraction A, d)  $v_c = 1200$  m/min, Fraction C

in speed to  $v_c = 800$  m/min, was divided into two fractions: B and C (both consisting of arc chips, however of different sizes), amounting to the total of 19 %. A similar distinction could be observed at  $v_c = 1200$  m/min.

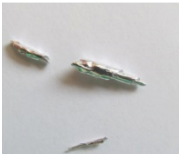
Fig. 5 shows chip shapes formed during milling performed at different cutting speeds  $v_c$ .

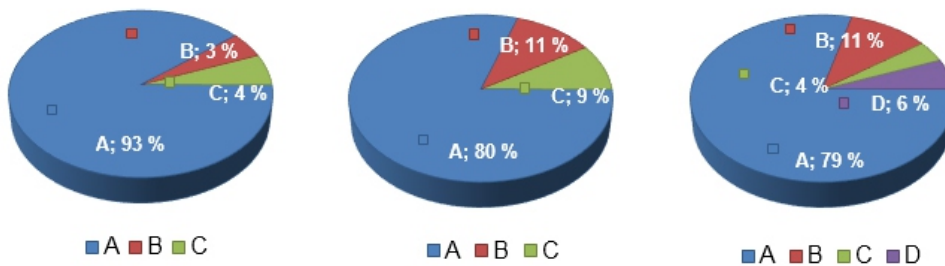
Fig. 5 shows chips classified as the smallest and largest fractions obtained at limit cutting speeds. The chips in question should generally be referred to as segmented, mainly due to the discontinuous character of the milling process. It should be noted that with increasing the milling speed  $v_c$ , the quality of the outer surface of the chip (which became rough) decreased. In the case of small fractions, the chips became tighter with increasing speed, and the cutting speed  $v_c = 400$  m/min produced arc chips. An opposite effect was

observed in the case of larger chips, which tend to have a tighter helix when the cutting speed is lower,  $v_c = 400$  m/min. In addition, built-up edges in the formed chips were observed. The distinguished chip forms are desirable from the point of view of chip removal from the working space.

Table 3 provides information about the effect of the feed rate  $f_z$  on the chip form and the quantity of chip fractions observed in the tests at given parameters. The lowest value of the feed tooth resulted in Fraction A dominating other chip forms. Leading fraction chips were described as short conical helical. Another fraction distinguished at these settings comprised chips of a distinctly different size and shape (short, tight and tubular). At the feed per tooth of  $f_z = 0.15$  mm/tooth the following chips forms were singled out: Fraction A – short conical helical chips, B – arc loose

**Table 3.** Impact of cutting speed on chip shape and quantity of fractions (AZ91HP magnesium cast alloy):a)  $f_z = 0.05$  mm/tooth, b)  $f_z = 0.15$  mm/tooth, c)  $f_z = 0.3$  mm/tooth, at  $v_c = 800$  m/min,  $a_p = 6$  mm and  $\gamma_o = 5^\circ$ 

$f_z$ [mm/tooth]	Fraction				
	All fractions	Leading fraction A	Intermediate fraction B	Intermediate fraction C	Intermediate fraction D
a) $f_z = 0.05$ mm/tooth					no fraction detected
b) $f_z = 0.15$ mm/tooth					no fraction detected
b) $f_z = 0.3$ mm/tooth					

**Fig. 6.** Percentage of particular chip fractions versus feed per tooth in the milling of AZ91HP magnesium alloy at carbide tool rake angle  $\gamma_o = 5^\circ$ , a)  $f_z = 0.05$  mm/tooth, b)  $f_z = 0.15$  mm/tooth, and c)  $f_z = 0.3$  mm/tooth

chips (bigger), C – loose arc chips (smaller). Finally, at the feed per tooth  $f_z = 0.3$  mm/tooth the following chip fractions were distinguished: A – short conical helical chips, B and C - loose arc chips, D – needle chips.

Fig. 6 shows the percentage of particular chip fractions at different rates of feed per tooth  $f_z$ .

At the feed per tooth  $f_z = 0.05$  mm/tooth, three fractions were distinguished, the leading one being Fraction A, accounting for 97 % of the total percentage of chips. An increase in this parameter produced a higher number of observed fractions, e.g. at  $f_z = 0.3$  mm/tooth four chip fractions could be distinguished. In both cases, the percentage of the leading fraction was approximately 80 %.

Fig. 7 shows chip shapes formed during milling performed at different feed per tooth rates; it also shows chips obtained from the smallest and largest

fractions at the limit feed per tooth value  $f_z$ . When comparing the leading fractions produced at different feed per tooth values, it can be observed that at  $f_z = 0.05$  mm/tooth, the outer surface of the chip is quite frayed (numerous small dents). Increasing the value of the feed per tooth results in increasing smoothness of the surface. A similar observation was made in the case of the smallest fractions: the outer surface is rougher at  $f_z = 0.05$  mm/tooth. The shape of chips of the leading fraction formed when the feed per tooth value was changed is advantageous for transport and storage.

Table 4 shows the impact of the cutting speed on the form of chips and the number of fractions distinguished during milling with the tool rake angle  $\gamma_o = 30^\circ$ . Fraction A chips (produced at  $v_c = 400$  m/min) are described as short conical helical and Fraction B chips as loose arc. A similar distinction was made

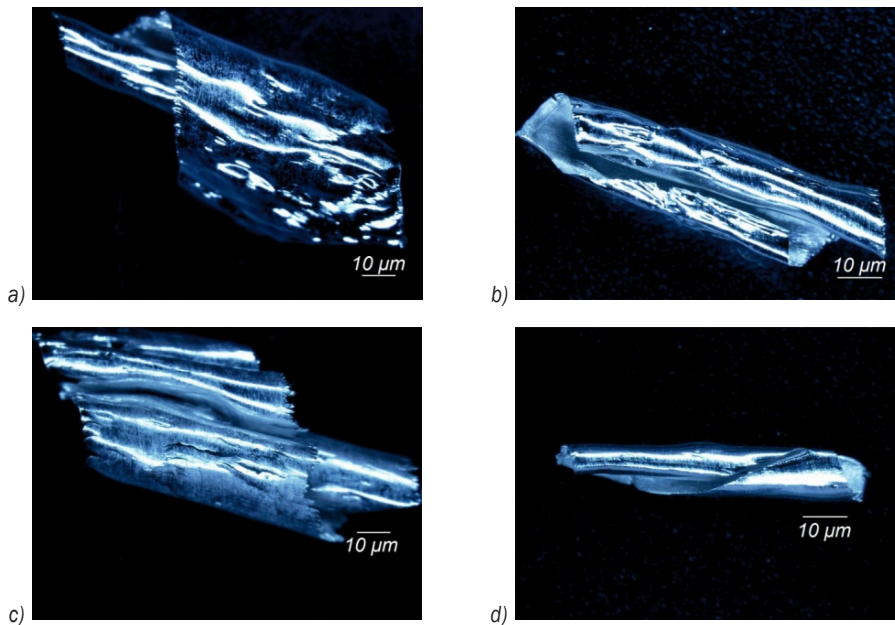


**Fig. 7.** Chips formed during AZ91HP magnesium cast alloy milling for selected chip fractions and different feed per tooth  $f_z$ : a)  $f_z = 0.05$  mm/tooth, fraction A b)  $f_z = 0.05$  mm/tooth, fraction B c)  $f_z = 0.3$  mm/tooth, fraction A, d)  $f_z = 0.05$  mm/tooth, fraction D

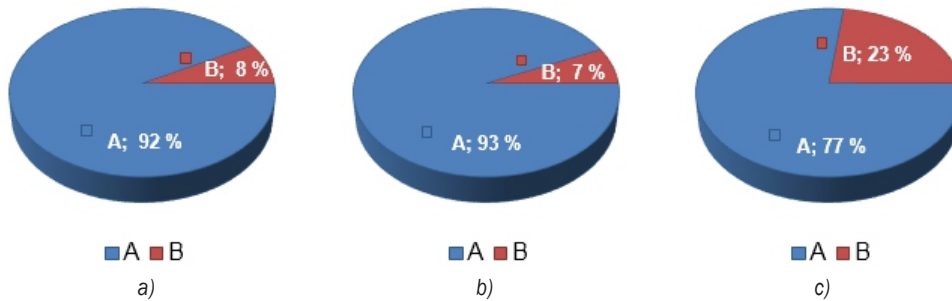
**Table 4.** Impact of cutting speed on chip shape and quantity of fractions (AZ91HP magnesium cast alloy): a)  $v_c = 400$  m/min, b)  $v_c = 800$  m/min, c)  $v_c = 1200$  m/min, at  $f_z = 0.15$  mm/tooth,  $a_p = 6$  mm and  $\gamma_o = 30^\circ$

$v_c$ [m/min]	Fraction				
	All fractions	Leading fraction A	Intermediate fraction B	Intermediate fraction C	Intermediate fraction D
a) $v_c = 400$ m/min				no fraction detected	no fraction detected
b) $v_c = 800$ m/min				no fraction detected	no fraction detected
c) $v_c = 1200$ m/min				no fraction detected	no fraction detected

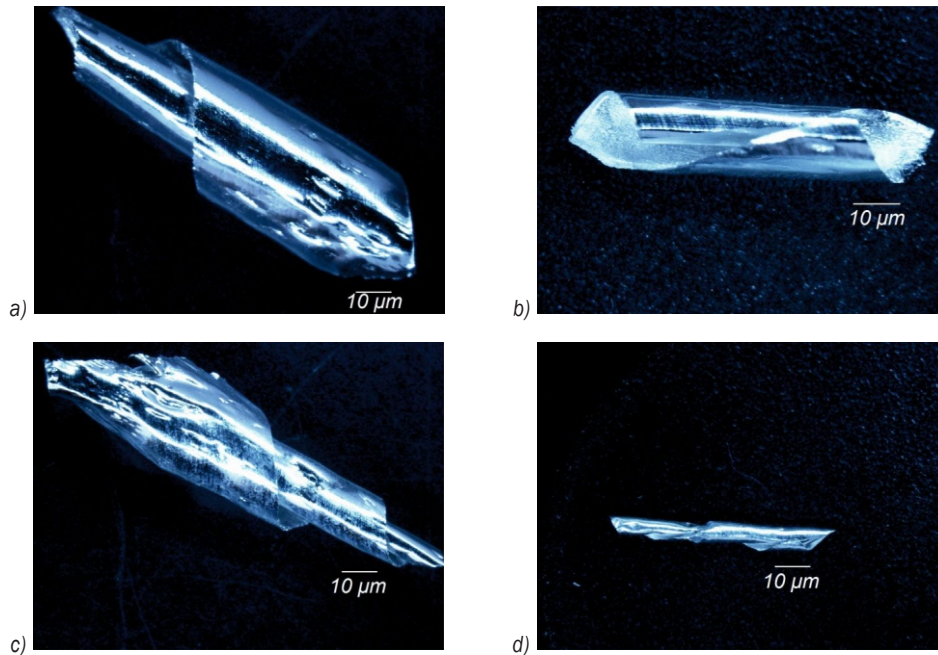
for the speed  $v_c = 800$  m/min. At the speed  $v_c = 1200$  m/min, Fraction A consisted of short conical helical chips, whereas needle chips could be observed in Fraction B.

Fig. 8 shows the percentage of particular chip fractions versus cutting speed in the milling of AZ91HP magnesium alloy.

As can be seen in Fig. 8, two fractions are determined per each cutting speed, and the percentage of particular chip fractions is virtually identical as at  $v_c = 400$  and  $v_c = 800$  m/min. At the speed  $v_c = 1200$  m/min, A remained the leading fraction; however, a distinct decrease in the number of chips belonging to Fraction B can be observed.



**Fig. 8.** Percentage of particular chip fractions versus cutting speed in the milling of AZ91HP magnesium alloy at carbide tool rake angle  $\gamma_o = 30^\circ$



**Fig. 9.** Chips formed during AZ91HP magnesium cast alloy milling for selected chip fractions and different cutting speeds  $v_c$ : a)  $v_c = 400$  m/min, Fraction A, b)  $v_c = 400$  m/min, Fraction B, c)  $v_c = 1200$  m/min, Fraction A, d)  $v_c = 1200$  m/min, Fraction B

Fig. 9 shows chip shapes observed during the milling process performed at different cutting speeds  $v_c$  at the tool rake angle  $\gamma_o = 30^\circ$ .

Fig. 9 shows the chips of the smallest and the biggest fractions, distinguished at the limit cutting speeds ( $v_c = 400$  m/min and  $v_c = 1200$  m/min). The representative chips can be described as segmented. With an increase in the cutting speed  $v_c$ , a tighter helix can be noted, as demonstrated by Fraction B (Figs. 7b and d). The outer surface of the chips is shiny and smooth when machined at a slower speed. The edges of the chips formed at the tool rake angle  $\gamma_o = 30^\circ$  are less built-up than those of the chips machined at the tool rake angle  $\gamma_o = 5^\circ$ .

The photographs in Table 5 show the variations in chip form and the quantity of chip fractions versus the feed tooth  $f_z$ . The shape of the chips formed when only the feed rate was changed does not reveal any great differences. One can predominantly observe short conical helical chips (Fractions A and B at  $f_z = 0.05$  mm/tooth, Fractions A and B at  $f_z = 0.15$  mm/tooth and Fraction A at  $f_z = 0.3$  mm/tooth). However, the greatest difference can be observed with respect to chip size. In Fractions C (the slowest feed) and B (the fastest feed), needle chips can be distinguished.

Fig. 10 shows the percentage of particular chip fractions at different rates of feed per tooth  $f_z$ .

The number of fractions was the highest at the lowest feed per tooth value, and in the remaining

**Table 5.** Impact of cutting speed on chip shape and quantity of fractions (AZ91HP magnesium cast alloy):

a)  $f_z = 0.05$  mm/tooth, b)  $f_z = 0.15$  mm/tooth, c)  $f_z = 0.3$  mm/tooth, at  $v_c = 800$  m/min,  $a_p = 6$  mm and  $\gamma_o = 30^\circ$

$f_z$ [mm/tooth]	Fraction				
	All fractions	Leading fraction A	Intermediate fraction B	Intermediate fraction C	Intermediate fraction D
a) $f_z = 0.05$ mm/tooth					no fraction detected
b) $f_z = 0.15$ mm/tooth				no fraction detected	no fraction detected
b) $f_z = 0.3$ mm/tooth				no fraction detected	no fraction detected

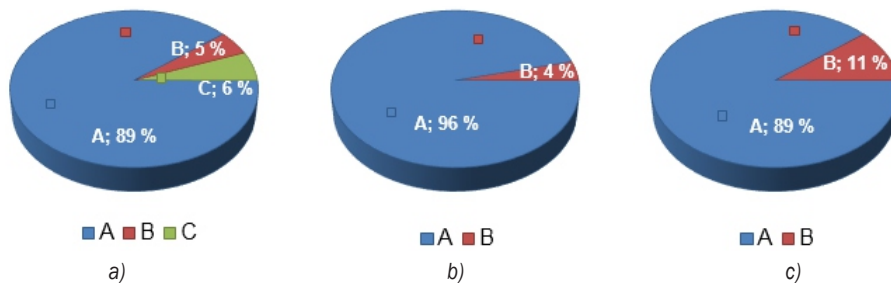


Fig. 10. Percentage of particular chip fractions versus feed per tooth in the milling of AZ91HP magnesium alloy at carbide tool rake angle  $\gamma_o = 30^\circ$

cases two fractions were noted. Out of three fractions distinguished at  $f_z = 0.05$  mm/tooth, Fraction A is the most numerous, while the percentages of Fractions B and C are comparable. At  $f_z = 0.15$  mm/tooth, Fraction A is the leading one (96 %), whereas the share of B is insignificant. Needle chips (Fraction B) constituted mere 11 %, and Fraction A remains the leading fraction at  $f_z = 0.3$  mm/tooth.

Fig. 11 shows chip shapes formed during milling performed at different values of feed per tooth  $f_z$ .

Fig. 11 show chips of the smallest and largest fractions produced at the limit feed values ( $f_z = 0.05$  mm/tooth and  $f_z = 0.3$  mm/tooth). The outer surface of the chips changed from wavy (Figs. 11a and b) to smooth (Figs. 11c and d).

The technological factors which contributed to reducing chip fragmentation to a minimum were cutting speed and feed tooth; in addition, it was observed that the rake angle  $\gamma_o = 30^\circ$  led to limiting the number of chip fractions. Moreover, the characteristic

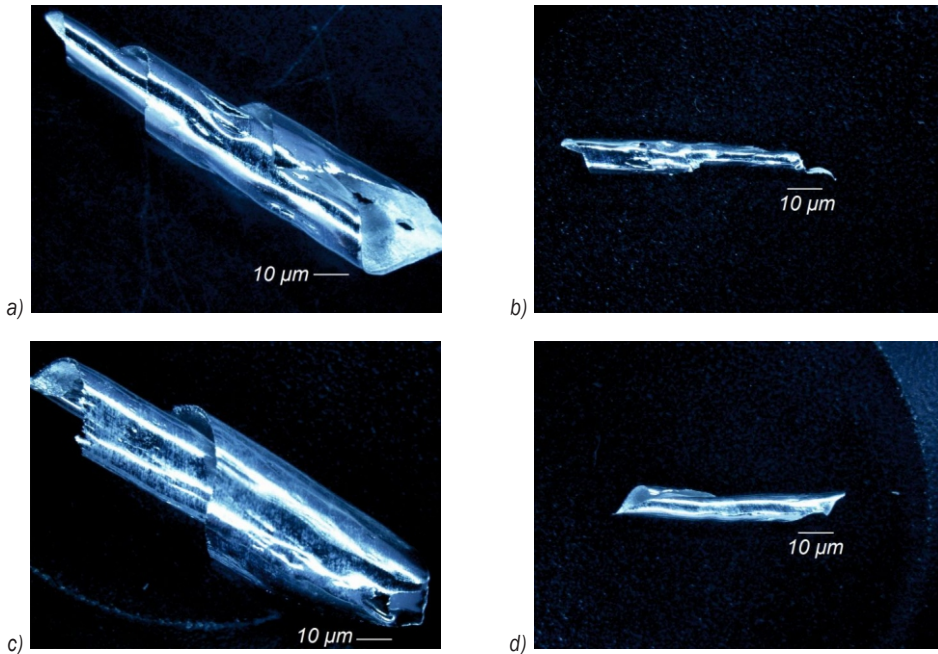
dimensions of the produced chips, including chip length L, chip width S and chip surface area P, were examined.

Fig. 12 illustrates the effect of the cutting speed  $v_c$  and the feed per tooth  $f_z$  on the length of the chip, both in the leading and intermediate chip fractions. An increase in the parameters  $v_c$  and  $f_z$  does not have an unequivocal effect on increasing or decreasing the length, width or surface area of chips. A more detailed analysis of the effect of the above parameters is feasible only for chip fractions, which occur at all values of  $v_c$  and  $f_z$ .

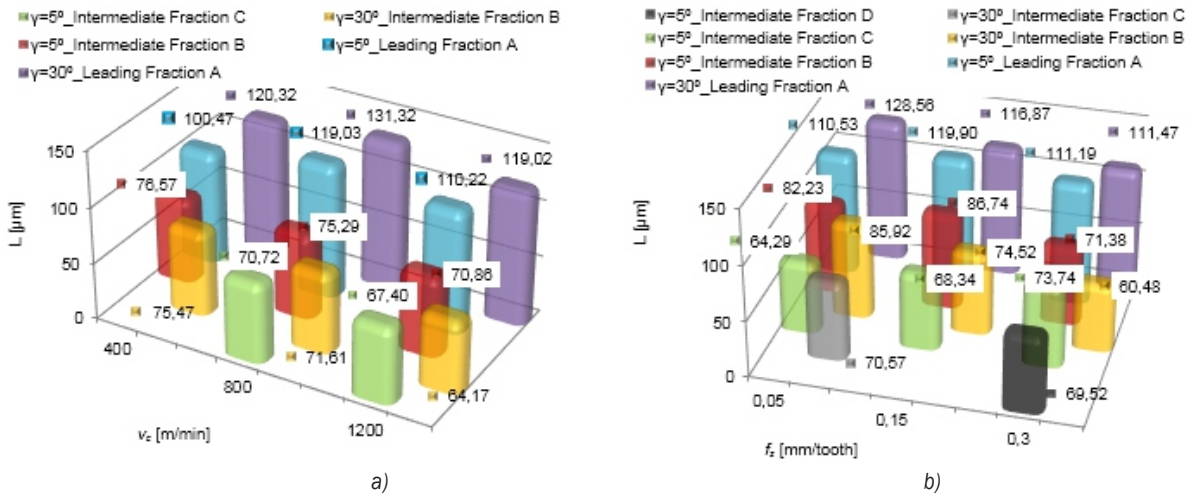
Fig. 13 illustrates the effect of the cutting speed  $v_c$  and the feed per tooth  $f_z$  on chip width.

Fig. 14 illustrates the effect of the cutting speed  $v_c$  and the feed per tooth  $f_z$  on chip area.

The examination of the dimensions of chips produced by milling using tools with a varying rake angle  $\gamma_o$  allow us to make the following observations with respect to the leading fraction:



**Fig. 11.** Chips formed during AZ91HP magnesium cast alloy milling for selected chip fractions and different values of feed per tooth  $f_z$ : a)  $f_z = 0.05$  mm/tooth, Fraction A b)  $f_z = 0.05$  mm/tooth, Fraction C, c)  $f_z = 0.3$  mm/tooth, Fraction A, d)  $f_z = 0.3$  mm/tooth, Fraction B



**Fig. 12.** Effect of technological parameters on chip length  $L$ : a)  $v_c$ , b)  $f_z$

- on changing  $v_c$ , the chip length  $L$  first increases and then decreases, both at  $\gamma_o = 5^\circ$  and  $\gamma_o = 30^\circ$ ,
  - on changing  $f_z$ , the chip length  $L$  first increases and then decreases at  $\gamma_o = 5^\circ$  and decreases in the entire range of change in the feed per tooth  $f_z$  at  $\gamma_o = 30^\circ$ ,
  - on changing  $v_c$ , the chip width  $S$  first decreases and then increases, both at  $\gamma_o = 5^\circ$  and  $\gamma_o = 30^\circ$ ,
  - on changing  $f_z$ , the chip width  $S$  first slightly decreases and then remains stable at  $\gamma_o = 5^\circ$  and increases at  $\gamma_o = 30^\circ$ ,
  - on changing  $v_c$ , the chip surface area  $P$  increases at  $\gamma_o = 5^\circ$  and decreases at  $\gamma_o = 30^\circ$ ,
  - on changing  $f_z$ , the chip surface area first increases and then increases at  $\gamma_o = 5^\circ$  and increases at  $\gamma_o = 30^\circ$ .
- We did not observe an unequivocal tendency for an increase or decrease in the dimensions of the leading chip fraction with increasing the cutting speed  $v_c$  and feed per tooth  $f_z$ .
- A detailed analysis of the intermediate fraction can only be done provided that this fraction occurs in

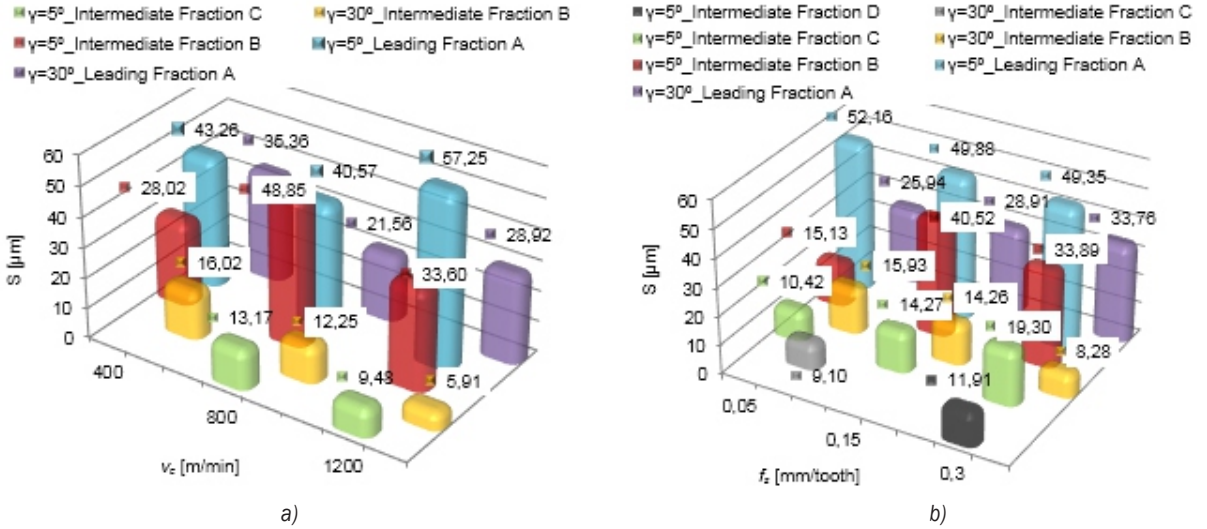


**Fig. 13.** Effect of technological parameters on chip width S: a)  $v_c$ , b)  $f_z$

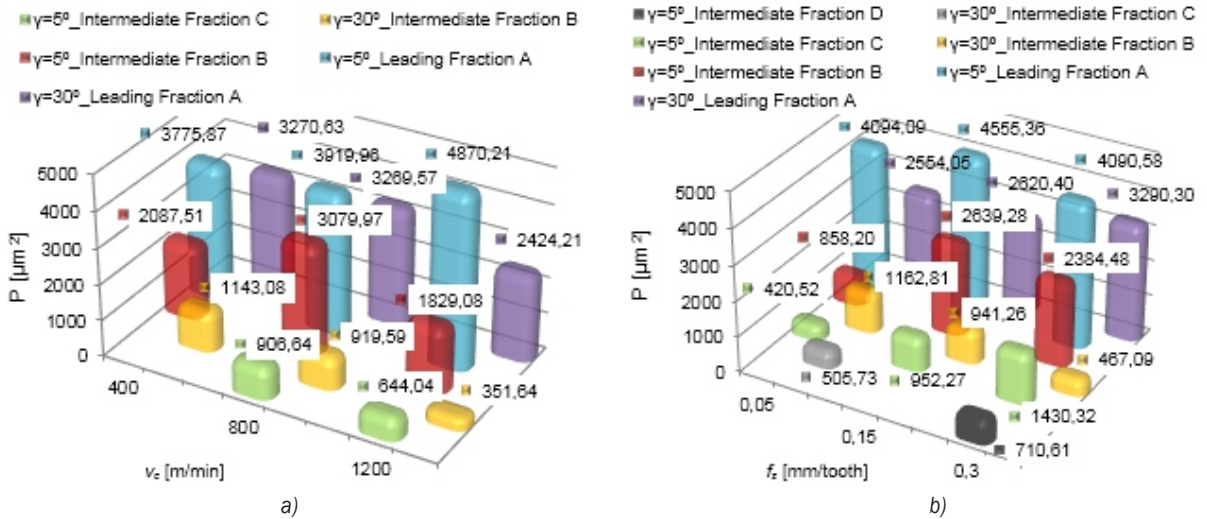


**Fig. 14.** Effect of technological parameters on chip area P: a)  $v_c$ , b)  $f_z$

the entire range of the investigated milling variables. This occurs for:

- on changing  $v_c$ , the chip length L of intermediate Fraction B decreases both at  $\gamma_o = 5^\circ$  and  $\gamma_o = 30^\circ$ ,
- on changing  $f_z$  in intermediate Fraction B ( $\gamma_o = 5^\circ$  and  $\gamma_o = 30^\circ$ ) and intermediate Fraction C ( $\gamma_o = 5^\circ$ ), the following trends can be observed: the chip length of Fraction B first increases and then decreases at  $\gamma_o = 5^\circ$ , the chip length of Fraction B decreases at  $\gamma_o = 30^\circ$ , the chip length of Fraction C increases at  $\gamma_o = 5^\circ$ ,
- on changing  $v_c$ , the chip width S of intermediate Fraction B first increases and then decreases at  $\gamma_o = 5^\circ$  and decreases at  $\gamma_o = 30^\circ$ ,
- on changing  $f_z$ , in intermediate chip Fraction B ( $\gamma_o = 5^\circ$  and  $\gamma_o = 30^\circ$ ), intermediate chip Fraction C ( $\gamma_o = 5^\circ$ ), the following trends can be observed: the chip width B of Fraction B first increases and then decreases at  $\gamma_o = 5^\circ$ , and decreases at  $\gamma_o = 30^\circ$ , while the chip width of Fraction C increases at  $\gamma_o = 5^\circ$ ,
- on changing  $v_c$ , the surface area P of intermediate Fraction B first increases and then decreases at  $\gamma_o = 5^\circ$  and decreases at  $\gamma_o = 30^\circ$ ,
- on changing  $f_z$ , in intermediate chip Fractions B ( $\gamma_o = 5^\circ$  and  $\gamma_o = 30^\circ$ ) and intermediate Fraction C ( $\gamma_o = 5^\circ$ ) the following trends can be observed: the surface area of chip Fraction B first increases and then decreases at  $\gamma_o = 5^\circ$ , the surface area of

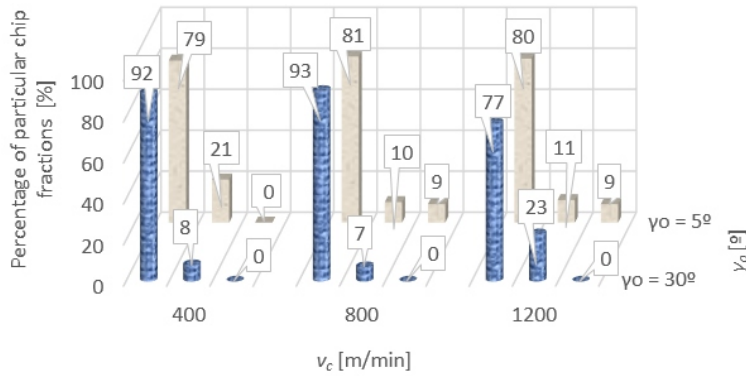


Fig. 15. Chip fraction percentage versus rake angle  $\gamma_o$  and cutting speed  $v_c$

Fraction B decreases at  $\gamma_o = 30^\circ$ , the surface area of Fraction C increases at  $\gamma_o = 5^\circ$ .

The analysed changes in the technological parameters of milling included the cutting speed  $v_c$  and the feed per tooth  $f_z$ . The tests investigated the impact of the aforementioned parameters and the rake value  $\gamma_o$  on the quantity of chip fractions generated during the milling of AZ91HP magnesium alloy. It was found that it is possible to determine the desired milling conditions to ensure control of the number of chip fractions. The conducted tests allowed us to formulate recommendations for effective and safe milling of AZ91HP magnesium alloy with respect to chip ignition hazard.

The experimental results about the degree of chip fragmentation indicate that fewer fractions were generated at the rake angle  $\gamma_o = 30^\circ$ .

On balance, the most beneficial milling conditions are ensured at the cutting speed  $v_c = 800$  m/min and  $v_c = 1200$  m/min, the feed per tooth values of  $f_z = 0.15$  mm/tooth and  $f_z = 0.3$  mm/tooth and the depth of cut of  $a_p = 6$  mm.

Regarding machining safety (including ignition risk), it is desirable to have the largest share of chip fractions. Additionally, Fig. 15 illustrates the relationship between the chip fraction share in total percentage depending on the applied rake angle and cutting speed.

It can be observed that increasing the rake angle and cutting speed leads to a decrease in the quantity of chips in the leading fraction, particularly at  $\gamma_o = 30^\circ$ . In contrast, the quantity of chips in the intermediate Fraction B increases. This observation is vital for process safety and effectiveness of the cutting process. It is therefore recommended, due to the fragmentation of chips, to use tools with a smaller rake angle ( $\gamma_o = 5^\circ$ ), particularly in higher cutting speed ranges that are typical of HSM processes.

### 3 CONCLUSIONS

Based on the experimental observations, the authors have formulated the following conclusions:

- I. fewer chip fractions (less fragmentation) are generated at the tool rake angle  $\gamma_o = 30^\circ$ .
- II. The most advantageous chip in terms of removal from the milling machine working space and storage is formed at the following parameters: depth of cut  $a_p = 6$  mm, feed per tooth  $f_z = 0.05$  mm/tooth and  $f_z = 0.15$  mm/tooth, cutting speed  $v_c = 400$  m/min and  $v_c = 800$  m/min.
- III. The results demonstrate that the biggest possible depth of cut and feed per tooth should be applied provided that quality requirements are adhered to. This observation is confirmed by the analysis of formed chip fractions.
- IV. It is impossible to state unequivocally whether chip dimensions increase or decrease with increasing the values of technological parameters ( $v_c$  and  $f_z$ ).
- V. The variations in chip dimensions are directly connected with decohesion (separation) of the machined layer into machining effects in the form of individual leading and intermediate chip fractions.

### 4 NOMENCLATURE

$v_c$	cutting speed, [m/min]
$n$	rotational speed, [rev/min]
$f_z$	feed per tooth, [mm/tooth]
$a_p$	axial depth of cut, [mm]
$a_e$	radial depth of cut, [mm]
$\gamma_o$	rake angle (in plane $P_o$ ), [°]
L	length of chip, [ $\mu\text{m}$ ]
S	width of chip, [ $\mu\text{m}$ ]
P	surface area of chip, [ $\mu\text{m}^2$ ]

## 5 REFERENCES

- [1] Wang, L., Zhou, J., Liang, J., Chen, J. (2013). Thermal control coatings on magnesium alloys prepared by plasma electrolytic oxidation. *Applied Surface Science*, 280, p. 151-155, DOI:10.1016/j.apsusc.2013.04.115.
- [2] Rashid, R.A.R., Sun, S., Wang, G., Dargusch M.S. (2013). Experimental investigation of laser assisted machining of AZ91 magnesium alloy. *International Journal of Precision Engineering and Manufacturing*, vol. 14, no. 7, p. 1263-1265, DOI:10.1007/s12541-013-0172-1.
- [3] Bagheri, H.R., Aliofkhaezaei, M., Gheyfani, M., Masiha, H.R., Sabour Rouhaghdam, A., Shahrahi, T. (2015). Growth and internal microstructure of micro-arc oxidized MgO-based nanocomposite coating. *Surface and Coatings Technology*, vol. 283, p. 1-9, DOI:10.1016/j.surfcoat.2015.10.041.
- [4] Wang, J., Liu, Y.B., An, J., Wang, L.M. (2008). Wear mechanism map of uncoated HSS tools during drilling die-cast magnesium alloy. *Wear*, vol. 265, no. 5-6, p. 685-691, DOI:10.1016/j.wear.2007.12.009.
- [5] Carou, D., Rubio, E.M., Lauro, C.H., Davim, J.P. (2014). Experimental investigation on finish intermittent turning of UNS M11917 magnesium alloy under dry machining. *The International Journal of Advanced Manufacturing Technology*, vol. 75, no. 9-12, p. 1417-1429, DOI:10.1007/s00170-014-6215-7.
- [6] Weinert, K., Inasaki, I., Sutherland, J.W., Wakabayashi, T. (2004). Dry machining and minimum quantity lubrication. *CIRP Annals - Manufacturing Technology*, vol. 53, no. 2, p. 511-537, DOI:10.1016/S0007-8506(07)60027-4.
- [7] Tomac, N., Tonnessen, K., Rasch, F.O. (1991). Formation of flank build-up in cutting magnesium alloys. *CIRP Annals - Manufacturing Technology*, vol. 40, no. 1, p. 79-82, DOI:10.1016/S0007-8506(07)61938-6.
- [8] Kulekci, M.K. (2008). Magnesium and its alloys applications in automotive industry. *The International Journal of Advanced Manufacturing Technology*, vol. 39, no. 9-10, p. 851-865, DOI:10.1007/s00170-007-1279-2.
- [9] Shi, K., Zhang, D., Ren, J. (2015). Optimization of process parameters for surface roughness and microhardness in dry milling of magnesium alloy using Taguchi with grey relational analysis. *The International Journal of Advanced Manufacturing Technology*, vol. 81, no. 1-4, p. 645-651, DOI:10.1007/s00170-015-7218-8.
- [10] Hou, J., Zhao, N., Zhu, S. (2011). Influence of cutting speed on flank temperature during face milling of magnesium alloy. *Materials and Manufacturing Processes*, vol. 26, no. 8, p. 1059-1063, DOI:10.1080/10426914.2010.536927.
- [11] Oczóś, K.E. (2009). Extension of the magnesium alloys application range. *Mechanik*, 5-6, p. 386-400, <http://www.mechanik.media.pl/archiwum,2009,50.html> (in Polish)
- [12] Wojciechowski, S., Twardowski, P., Pelic, M., Maruda, R.W., Barrans, S., Krolczyk, G.M. (2016). Precision surface characterization for finish cylindrical milling with dynamic tool displacements model. *Precision Engineering*, vol. 46, p. 158-165, DOI:10.1016/j.precisioneng.2016.04.010.
- [13] Wojciechowski, S., Maruda, R.W., Nieslony, P., Krolczyk, G.M. (2016). Investigation on the edge forces in ball end milling of hardened steel. *International Journal of Mechanical Sciences*, vol. 119, p. 360-369, DOI:10.1016/j.ijmecsci.2016.10.034.
- [14] Maruda, R.W., Krolczyk, G.M., Nieslony, P., Wojciechowski, S., Michalski, M., Legutko, S. (2016). The influence of the cooling conditions on the cutting tool wear and the chip formation mechanism. *Journal of Manufacturing Processes*, vol. 24, p. 107-115, DOI:10.1016/j.jmapro.2016.08.006.
- [15] Gziut, O., Kuczmaszewski, J., Zagórski, I. (2016). Surface quality assessment following high performance cutting of AZ91HP magnesium alloy. *Management and Production Engineering Review*, vol. 6, no. 1, p. 4-9, DOI:10.1515/mp-2015-0001.
- [16] Józwick, J., Mika, D. (2015). Diagnostics of workpiece surface condition based on cutting tool vibrations during machining. *Advances in Science and Technology Research Journal*, vol. 9, no. 26, p. 57-65, DOI:10.12913/22998624/2365.
- [17] Guo, Y.B., Salahshoor, M. (2010). Process mechanics and surface integrity by high-speed dry milling of biodegradable magnesium-calcium implant alloys. *CIRP Annals - Manufacturing Technology*, vol. 59, no. 1, p. 151-154, DOI:10.1016/j.cirp.2010.03.051.
- [18] Ruggiero, A., D'Amato, R., Gómez, E., Merola, M. (2016). Experimental comparison on tribological pairs UHMWPE/TIAL6V4 alloy, UHMWPE/AISI316L austenitic stainless and UHMWPE/AL203 ceramic, under dry and lubricated conditions. *Tribology International*, vol. 96, p. 349-360, DOI:10.1016/j.triboint.2015.12.041.
- [19] Ruggiero, A., D'Amato, R., Gómez, E. (2015). Experimental analysis of tribological behavior of UHMWPE against AISI420C and against TiAl6V4 alloy under dry and lubricated conditions. *Tribology International*, vol. 92, 154-161, DOI:10.1016/j.triboint.2015.06.005.
- [20] Li, H.Z., Liu, K., Li., X.P. (2001). A new method for determining the undeformed chip thickness in milling. *Journal of Materials Processing Technology*, vol. 113, no. 1-3, p. 378-384, DOI:10.1016/S0924-0136(01)00586-6.
- [21] Saï, L., Bouzid, W., Zghal, A. (2008). Chip thickness analysis for different tool motions: for adaptive feed rate. *Journal of Materials Processing Technology*, vol. 204, no. 1-3, p. 213-220, DOI:10.1016/j.jmatprotec.2007.11.094.
- [22] Fang, F.Z., Lee, L.C., Liu, X.D. (2005). Mean flank temperature measurement in high speed dry cutting. *Journal of Materials Processing Technology*, vol. 167, no. 1, p. 119-123, DOI:10.1016/j.jmatprotec.2004.10.002.
- [23] Hou, J.Z., Zhou, W., Zhao, N. (2010). Methods for prevention of ignition during machining of magnesium alloys. *Key Engineering Materials*, vol. 447-448, p. 150-154, DOI:10.4028/www.scientific.net/KEM.447-448.150.
- [24] Zhao, N., Hou, J., Zhu, S. (2011). Chip ignition in research on high-speed face milling AM50A magnesium alloy. *2nd International Conference on Mechanic Automation and Control Engineering*, no. 5987127, p. 1102-1105, DOI:10.1109/MACE.2011.5987127.
- [25] Hou, J.Z., Zhou, W., Zhao, N. (2010). Effect of cutting parameters on ignition of AM50A mg alloy during face milling. *Materials and Manufacturing Processes*, vol. 25, no. 10, p. 1048-1051, DOI:10.1080/10426910903496870.

- [26] Akyuz, B. (2011). Machinability of magnesium and its alloys. *The Online Journal of Science and Technology*, vol. 1, no. 3, p. 31-38.
- [27] Lin, P.Y., Zhou, H., Li, W., Li, W.P., Sun., N., Yang, R. (2008). Interactive effect of cerium and aluminium on the ignition point and the oxidation resistance of magnesium alloy. *Corrosion Science*, vol. 50, no. 9, p. 2669-2675, DOI:10.1016/j.corsci.2008.06.025.
- [28] Zhou, H., Li, W., Wang, M., Zhao, Y. (2005). Study of ignition proof AZ91D magnesium alloy chips with cerium addition. *Journal of Rare Earths*, vol. 23, p. 466-469, available from [https://www.researchgate.net/publication/279539824\\_Study\\_on\\_ignition\\_proof\\_AZ91D\\_magnesium\\_alloy\\_chips\\_with\\_cerium\\_addition](https://www.researchgate.net/publication/279539824_Study_on_ignition_proof_AZ91D_magnesium_alloy_chips_with_cerium_addition) accessed on 2017-02-21.
- [29] Liu, M., Shih, D.S., Parish, C., Atrens, A. (2012). The ignition temperature of Mg alloys WE43, AZ31 and AZ91. *Corrosion Science*, vol. 54, p. 139-142, DOI:10.1016/j.corsci.2011.09.004.
- [30] Ravi Kumar, N.V., Blandin, J.J., Suéry, M., Grosjean, E. (2003). Effect of alloying elements on the ignition resistance of magnesium alloys. *Scripta Materialia*, vol. 49, no. 3, p. 225-230, DOI:10.1016/S1359-6462(03)00263-X.
- [31] ISO 3685:1993. *Tool-life testing with single-point turning tools*. International Organization for Standardization, Geneva
- [32] Kuczmaszewski, J., Zagórski, I. (2014). Investigation of chips fragmentation during magnesium alloys milling. *Mechanik*, 8-9, p. 321-328, from [http://www.mechanik.media.pl/pliki/do\\_pobrania/artykuly/13/viii\\_sos.pdf](http://www.mechanik.media.pl/pliki/do_pobrania/artykuly/13/viii_sos.pdf), accessed on 2017-02-21. (in Polish)
- [33] Salahshoor, M., Guo, Y.B. (2011). Surface integrity of magnesium-calcium implants processed by synergistic dry cutting-finish burnishing. *Procedia Engineering*, vol. 19, p. 288-293, DOI:10.1016/j.proeng.2011.11.114.
- [34] Matuszak, J., Zaleski, K. (2014). Edge states after wire brushing of magnesium alloys. *Aircraft Engineering and Aerospace Technology*, vol. 86, no. 4, p. 328-335, DOI:10.1108/AEAT-09-2012-0155.

# The Effects of Milling Strategies on Forces, Material Removal Rate, Tool Deflection, and Surface Errors for the Rough Machining of Complex Surfaces

Eyup Bagci\* – Ercüment U. Yüncüoğlu

Naval Architecture and Maritime Faculty, Yıldız Technical University, Turkey

*The high-performance machining of curved surfaces is a highly critical process that is crucial in modern engineering applications. Different methodologies and CAM tools have been developed by manufacturers to improve the efficiency of the sculptured surface milling. The determination of appropriate tool path strategies and milling conditions is crucial in ensuring a high productivity rate, meeting the better surface texture values, and lower cutting forces, tool deflection, and surface errors. The objective of this research is to analyse the effect of tool path strategies on dynamic tool deflection, cutting forces, machining time, effective cutter diameter (ECD), cutter/workpiece engagement (CWE) area, instantaneous material removal rate (IMRR), and machining errors in rough machining of a sculptured surface. The B-rep solid modeling-based simulation and the optimization system were developed and integrated with the commercial CAD/CAM software for 3-axis ball-end milling. The experimental results clearly show the influence of the cutter path strategies on machining times and their importance for reducing time needed and, consequently, costs. It was observed that the profiles of deflection, IMRR values, cutting forces, machining errors and ECD values match very well for cutting strategies. Machining strategies employed include various degrees of zig-zag, profiling, and spiral. The conclusion is that the 90° zig-zag strategy provokes the lowest cutting forces, tool deflection, and surface error values. The in-house NC simulation system performed well in determining values and the location of milling form errors on the surface.*

**Keywords:** milling, free-form surfaces, MRR, machining errors, cutting strategies

## Highlights

- The data presented in this work have shown that the use of different milling strategies when rough ball end milling of free-form surfaces has a significant effect on the on-tool deflection, cutting forces, instantaneous material removal rate, machining time and surface errors
- B-Rep based simulation/optimization system was developed and integrated with CAM software to calculate the effective cutter diameter, cutter/workpiece engagement area, instantaneous material removal rate, and milling errors.
- The 90° zig-zag cutter path appears to provide preferred results in terms of tool deflection, surface errors, and lower cutting forces. Tool deflection and cutting forces have quantitative and qualitative influence on machining surface errors.
- The proposed B-rep simulation approach is experimentally verified to predict the machining errors.

## 0 INTRODUCTION

Sculptured/curved surfaces, today, are widely used in several industries, for instance, automotive, aerospace, bio-medical components, precision machine design and die-mould industries. Recent improvements in CAM software have allowed the manufacturing of complex curved geometries. The ball-end/nose milling is a flexible process that is capable of milling both convex and concave part surfaces with rough, semi-rough and finish processes. The sculptured surface milling is mostly realized by the repeated motion of a rotating cutter along pre-defined trajectories. Manufacturing engineers can choose the cutter paths generation approach from a set of typical paths (zig, zig-zag, concentric, radial tool paths, etc.) in commercial CAM software. In addition, these strategies cannot be optimized for all complex surfaces to be milled. A substantial number of studies have examined this subject, and many path-generation

approaches have been developed, as shown in Fig. 1 [1] and [2].

The strategies can be sorted into three basic categories: offset, single direction, and raster. In offset milling, the cutter starts at the periphery of the face and then proceeds spirally inwards. In a raster milling strategy (zig, zig-zag, or sweep) the cutting tool moves back and forth across the milled workpiece [3]. In spiral milling, the cutter returns to the start-point of each cycle and then cuts outwards to the next outer cycle. When using a spiral strategy, the cutting time is hugely decreased. The selection of the proper milling strategy in the process of milling will decrease cutting time, improve the surface quality of the finished part and tool life and reduce machining costs and cutting forces. Kurt and Bagci [4] and Lasemi et al. [5] reviewed the recent research literature on milling of complex-curved surfaces and feed-rate optimization approaches. Chen et al. proposed a real-time monitoring system with error compensation to

\*Corr. Author's Address: Naval Architecture and Maritime Faculty, Yıldız Technical University, Turkey, eyupbagci@gmail.com

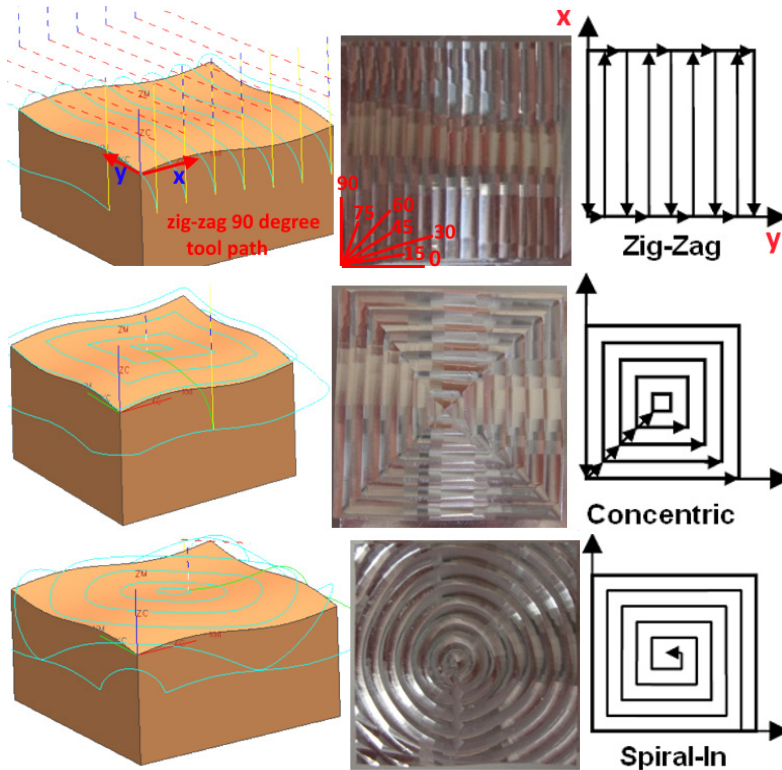


Fig. 1. Representation of cutting patterns and tool-path strategies

enhance dimensional accuracy in the production of complex components. They created a method for the combination of the on-line inspection and the compensation of the machining errors and verified the method by experiments. [6]. Habibi et al. modelled the machining process for force/deflection calculations in a 3D simulation environment. They found that the accuracy of machined features can be improved by about 8 to 10 times a single pass by using a new method [7]. Desai and Rao determined the effect of variable curvature geometries by machining from both parametric directions and using cutters of different diameters. They determined that a considerable amount of shift in the location of peak cutting forces with the change in cutting direction and cutter diameter, particularly in concave regions of the workpiece geometry [8]. Alberti et al. [9] compared the dimensional part errors with cutting time in the milling of Al alloy. They suggested that the tool holder has considerable influence over dimensional accuracy and that type of interpolation appreciably affects the cycle time. Erdim et al. published a method to adjust the feed-rate according to milling force in order to reduce machining time. They concluded that a forced-based feed-rate scheduling technique gives controllable force magnitudes and surface errors [10].

Kaymakci and Lazoglu proposed a new model to predict the cutting forces, free-form surface topographies, error distributions and cycle times for various tool paths with the integrated milling software [11]. Brooks et al. experimentally investigated the surface metrology of a 12.70-mm-thick curved plate platform of AISI SS304 material during milling on a vertical three-axis milling machine with three different tool path strategies: ramp, contour, and peripheral. Cutting mechanics and cutting forces were analysed for the defined values of the strategies [12]. Gok et al. focused on investigating optimum cutting parameter values in ball end milling of tool steel with three coated cutters. The effects of tool path styles in the ball end milling of inclined surfaces have been determined. They found that TiC coating for cutting forces was the most rapidly deteriorating one [13]. Shajari et al. investigated different machining strategies in 3-axis milling of a typical curved geometry part and also developed an approach to the mathematical model to measure the scallop height size and distribution. They determined the optimized strategy based on the results [14]. Vila et al. examined the power consumption of different cutting strategies in face milling operations in order to evaluate the efficiency of each cutting strategy. They found that the

optimal cutting strategy to ensure a predefined quality specification [15]. Shajari et al. developed a cutting force as a new decision criterion for the best selection of tool paths on convex surfaces. They concluded that the radial strategy provokes the best surface texture and the lowest cutting forces and the spiral strategy signifies the worst surface texture and the highest cutting forces [16]. Izol et al. studied comparison and evaluation of the milling strategies to produce components with freeform surfaces. They suggested a guideline for the production process of tools with sculptured surfaces, such as tools for metal sheet forming, dies, moulds for plastics and many others [17]. Matras et al. presented the analysis results of machining accuracy after the free-form surface milling simulations for different machining strategies. They suggested a guideline of the usage CAD/CAM software in order to measure the machining accuracy for the selected strategies and cutting data [18]. Hassanpour et al. investigated the effect of raster, 3D-offset, spiral and radial tool path strategies and machining parameters on microhardness of a typical curved surface (convex) of stainless steel 1.4903. They found that the spiral strategy provided the maximum hardness and the radial strategy the minimum hardness [19]. Pahole et al. studied the influence of the CNC machining direction during high-speed milling on the durability of the engraving within the forging tool. They found that the correct milling strategy can often cause an increase in the durability of a forging tool by about one third [20]. Schützer et al. developed a method to use free-form features to improve the automatic generation of high-speed machining information for specific geometric areas to create HSC free-form manufacturing features. Their approach reduces significantly the programming time to produce HSC appropriate tool paths for the same quality [21]. Lazoglu et al. developed an approach to generate optimized tool paths for free-form surfaces. They claim that their approach is the first method for generating the tool paths based on process mechanics for globally minimizing the cutting forces for any given free-form surface [22]. Zang et al. examined 3D tool paths' effects on the CNC efficiency, surface quality and form accuracy. It is found that the parallel tool path, which is one of the 3D tool path strategies with a 2-axes driving mode, can improve the surface quality and form accuracy in the actual milling of a complex freeform surface [23]. Wei et al. studied an integrated form error compensation approach for ball-end milling of sculptured surface with a z-level contouring tool path and presented the approach reduce form error in ball-end milling of the

sculptured surface according to experimental results [24]. Cao et al. examined the curvature radius effect on machining productivity and found that curvature radius has an obvious effect on machining productivity and quality by using experiments [25]. Tan et al. examined the influence of cutter path orientation and the cutting forces, tool life, tool wear, and surface integrity for finish milling of TC17 alloy; they suggested that the horizontal downward orientation produced the highest cutting forces, and vertical downward orientation provided the best tool life, with cut lengths 90 % to 380 % longer than for all other orientations [26]. Uhlmann et al. examined the error sources of freeform surface milling processes, for the decisive factors that significantly influence the productivity and the workpiece quality. They concluded that each error sources proportion may be related to the deviations measured in particular regions of the machined surface [27]. Scandiffio et al. focused an investigation of free-form milling of hard material AISI D6 tool steel using a ball-end cemented carbide cutting tool and created a guideline for cutting tools life [28]. The simulation of the process of NC milling is of main importance in CAM systems. The virtual simulation of machining processes has started to become more important in order to minimize the dissimilarities between the designed and real milled surfaces, and one of the critical technologies for advancing the efficiency and quality of the cutting process is to design and produce. Various approaches to NC milling simulation have been described in the literature, and they can be categorized into three major approaches: solid modeling, spatial partitioning, and discrete vectors. In NC milling, as the cutter moves along the tool trajectories, it forms a swept volume, and a portion of the workpiece is removed. During the tool motion, it is in contact with the workpiece over an instantaneous common surface which is called cutter workpiece engagement (CWE) area. It is required to have an accurate geometric representation of the engagement surface in order to calculate cutting forces, energy consumption, power, cutter deflections, surface quality (texture and errors), and chatter.

Tunc and Stoddart focused evaluating and selecting tool path patterns, offered by the existing CAM packages, for increased chatter-free MRR and the proposed approach. They performed simulations and experiments to show applications of approach [29]. Scandiffio et al. studied the influence of effective cutting speed and tool-surface contact on tool wear and surface roughness. Contrary of other studies, they found that contact between the centre of the tool tip and the workpiece can increase tool life and

reduce roughness when milling free-form surfaces in hardened steel [30]. Cao et al. proposed a cutting force model considering influence of radius of curvature. They compared analytically estimated cutting forces and actual cutting forces obtained through experiments [31]. Miao et al. studied an efficient solid-based geometric NC simulation approach and performed consecutive Boolean subtractions to simulate the cutting process. Then, they validated simulation by experiment [32]. Li et al. developed a three-axis milling process simulation system based on quadtree-array representation and used to evaluate the performance of the presented method. Their method improved the simulation efficiency significantly [33]. Aras et al. focused a solid modelling-based methodology for finding cutter-workpiece engagements (CWE) generated in five-axis milling of free-form surfaces. They plotted the CWE boundaries from Euclidean 3D space to a parametric space defined by the engagement angle and the depth-of-cut for a given tool geometry [34]. Lee and Nestler presented a methodology to generate a virtual workpiece (VWP). They validated the VWP model by material removal processes, milling and micro-EDM operations [35]. Boz et al. studied two different methods of obtaining CWE maps for three- and five-axis flat and ball-end milling. They verified the methods experimentally and computationally [36].

This paper presents a B-rep solid modeling-based NC simulation and optimization system, which is integrated with the commercial CAM software due to calculation of THE instantaneous material removal rate (IMRR), effective cutter diameter, cutter/workpiece engagement area (CWE), and machining errors. In this system, simulation of the cutting process is based on solid models of a workpiece, its blank, and a cutter created with modeling functions of a commercial CAD/CAM system and cutting paths generated by the CAM application of the same system. The main objective of this work is to analyse the influence of tool path strategies on dynamic tool

deflection, cutting forces, instantaneous material removal rate, effective cutter diameter, machining time and surface errors have been analysed by experimentally and computationally for 3-axis ball-end milling.

## 1 EXPERIMENTAL WORKS

### 1.1 Cutting Tools and Workpiece Materials

The cutting tools used were chosen from the Sandvik Coromat Catalog to machine Aluminium 7075-T651. The chemical composition and mechanical properties of the Al 7075-T6 material are given in Table 1. Cutting tools of 12 mm diameter, with two teeth, were employed for milling the experimental surfaces. Details of the tools are given in Fig. 2 and Table 2. The cutters were held in a BT-40 taper tool holder. In this work, tool wear was not considered as a criterion affecting the result of the cutting process since the material being utilized is soft.

The experiments were conducted using a CNC Johnford VMC Model three-axis CNC milling machine equipped with a maximum spindle speed of 12,000 rpm and a 10-kW drive motor, as shown in Fig. 3. This machine was designed to make 3-axis linear and circular interpolations via ISO format programs in metric and imperial units. Its control unit was a FANUC series O-M. The experiments used rectangular samples (100 mm × 53 mm × 30 mm) of Al 7075-T651 aerospace alloy. The machined surface is shown in Fig. 4. Several program packages were used in the evaluation of the data and in the experimental design of the study. The specimen was designed in CATIA V5 R17. The same software was also employed, on a personal computer containing an Intel Pentium IV chip and operating at 2.80 GHz, for the creation of the CNC part-manufacturing programs used in the study.

**Table 1.** Chemical composition and mechanical properties of material

Chemical composition [wt%]	Si	Fe	Cu	Mn	Mg	Cr	Ag	B
	0.393	0.260	1.26	0.044	1.94	0.288	0.0067	0.005
	Be	Bi	Ca	Co	Ni	Zn	Ti	Sn
	0.0028	0.001	0.048	0.032	0.027	5.92	0.086	0.0035
Mechanical properties	V	Al	Li	Na	Pb	Sr	Zr	Cd
	0.0087	89	0.347	0.015	0.0058	0.211	0.0014	0.0001
	Tensile strength [MPa]	Yield strength [MPa]	Elongation [%]	Shear modulus [MPa]	Tensile Modulus [GPa]			
	503	434	13	303	72			

**Table 2.** The dimensional properties of the tool

Tool Diameter	12 mm
Flute	2 flutes
Tool Length	120 mm
Helix Angle	30°
Shank Type	Cylindrical

**Table 3.** Cutter path strategies for machining

Tool path strategies	Test	
0°	1	
15°	2	
30°	3	
Zig-Zag	4	
60°	5	
75°	6	
90°	7	
Concentric/ contour parallel	on Part surface- B1 Step over- constant 3D	8
	on Plane- B2 Step over- constant 2D	9
Spiral	Spiral-C1	10

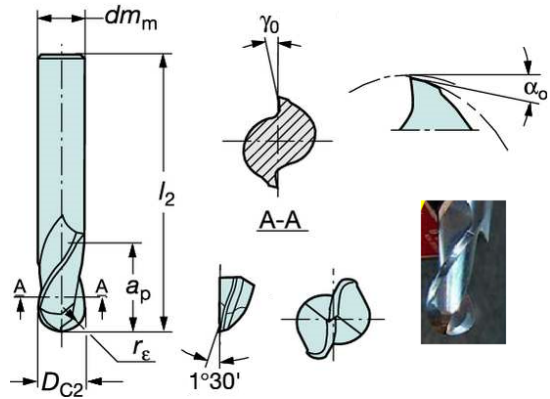


**Fig. 2.** The ball end milling tool

**1.2 Cutting Conditions**

Three tool path patterns are applied to free-form surface in Fig. 1 and Table 3. Besides these three alternatives, the zig-zag type is used together with six different cut angles. The cut angle is measured

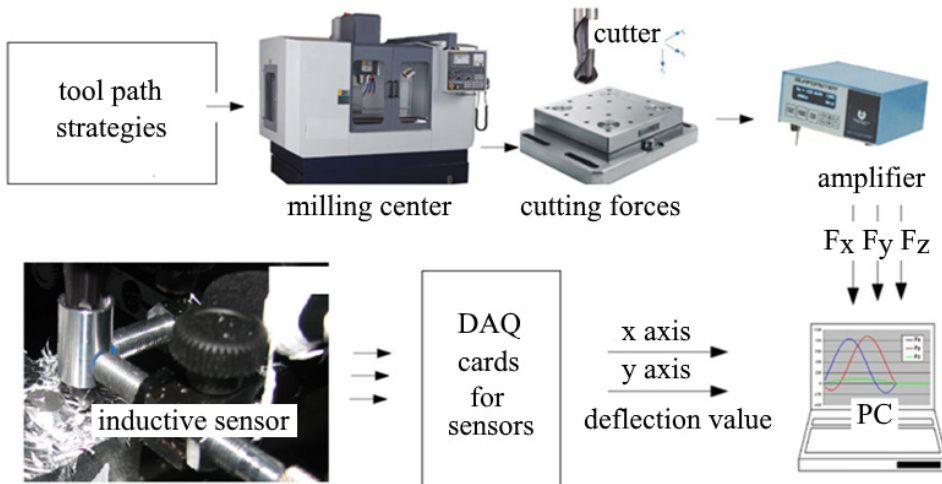


**Fig. 3.** Experimental setup for measurement of forces and deflection

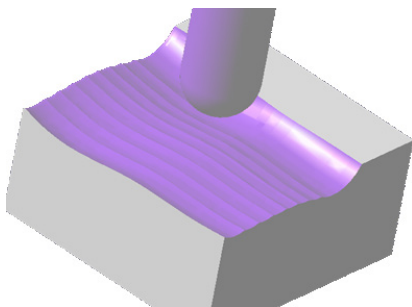


**Fig. 4.** CAD geometry of used in the experiments

with respect to the X axis in the X-Y plane of the coordinate axis. The angle is projected to the floor plane. Tool-path strategies were compared in terms of cutting force, deflection, IMRR, dimensional error values and milling time. The machining parameters are summarized in Table 3. Constant pick feed of 3 mm was used for all cases. In cutting tests, spindle speed, feedrate and feed per tooth were 600 rpm, 96 mm/min and 0.08 mm, respectively. The cutter is parallel to the Z axis, and the maximum and minimum

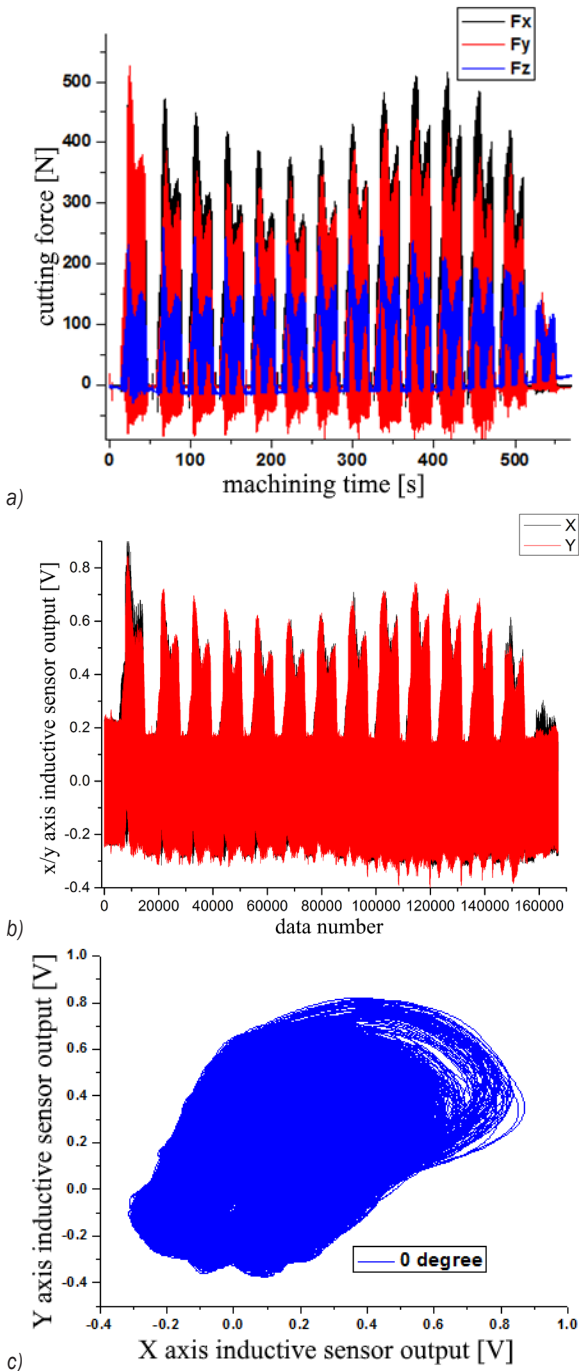


Fig. 5. a) Cutting forces and b), c) the tool deflection for 0° zig-zag tool path

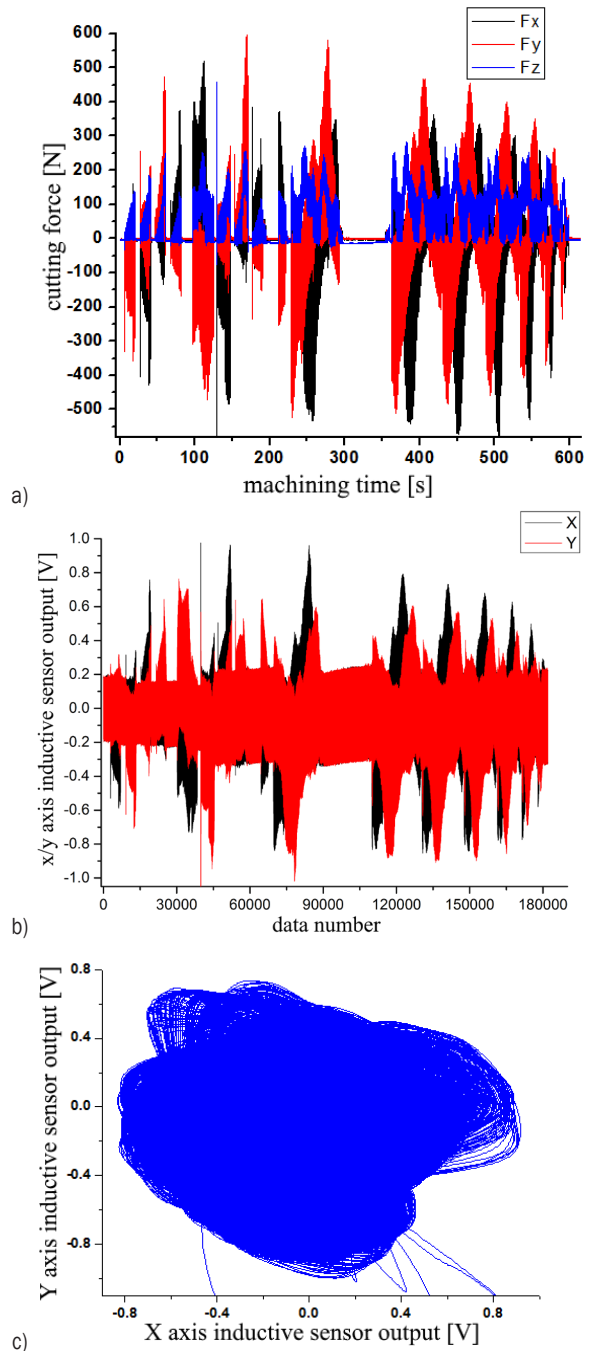


Fig. 6. a) Cutting forces and b), c) the tool deflection for spiral tool path

depths are 5.5 mm and 1.5 mm respectively for this part. The machined workpieces can also be seen with the tool path alternatives in Figs.1 and 8.

### 1.3 Cutting Forces and Tool Deflection Measurements

Cutting force measurements ( $F_x$ ,  $F_y$ , and  $F_z$ ) are made using a Kistler 3-component piezoelectric type 9257A platform dynamometer. The whole system was checked and calibrated prior to use. The cutting

force data is downloaded from oscilloscope, and information on cutting force signatures is stored onto a PC; after processing of the cutting force data, an analysis is performed using the software as shown in Figs. 5a and 6a.

Cutter deflection measurement has been carried out using two precision inductive displacement sensors placed at 90° one from the other as shown in Fig. 7. For cutter deflection measurement, an aluminium ring was fitted to the flute part of the cutter and machined after being clamped in the spindle. Figs. 5b and c and 6b and c show the experimental results for cutter deflection measurement for spiral and 0° zig-zag machining strategies. Tool deflection and cutting forces values showed similar tendencies.

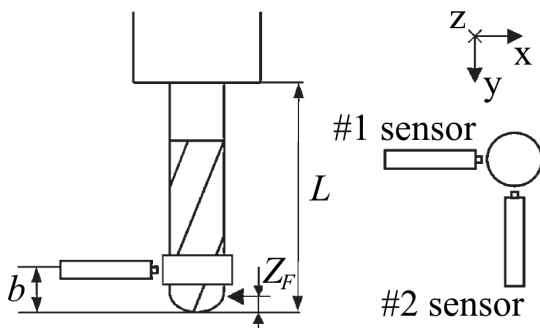


Fig. 7. Tool deflection measurement setup

**1.4 Measurement of Machining Errors**

A 3D optical measuring system based on fringe projection was used to determine the machining errors in the workpieces by analysing the different textural properties to the body [37]. 3-D optical scanning

provided point cloud, curves, and meshed data. The obtained data were indexed into the CAD software, which computed and displayed the deviations between the two data sets, as shown in Fig. 8.

**1.5 Development of B-Rep Based NC Simulation System**

The basic input to the BRep-based NC simulation system is the NC cutter path either in cutter location (CL) format or G/M-code format. After the CL data are interpreted, the swept volume of the cutter is intersected with the blank at every small sampling interval along the tool path and the intersection is considered as the undeformed chip. The geometric simulation of machining calculates the instantaneous contact area between the cutter and work piece at any time. The solid approach-based CWE model and a model to calculate real IMRR, ECD and prediction of milled surface errors were examined. Data related to the milling process was obtained using an in-house application programmer’s interface (API) software based on B-rep. After the in-process workpiece geometry was obtained for each G code line, the contact area, and generated surface between the tool and workpiece can be extracted by using the in-house API as shown in Fig. 9. The IMRR value can be obtained by determining the intersection geometry between cutter swept volume and workpiece during the tooth passing period ( $t_p$ ) and the volume is divided by  $t_p$  to compute the average MRR [38]. The chip thickness at any location on the cutting tool is computed as shown in Eq. (1) by dividing the scalar product of the feed ( $f$ ) with the surface normal vector ( $N_s$ ) by the number of cutter teeth ( $n_t$ ), multiplied by the tool rotation values (N-rpm)[4]:

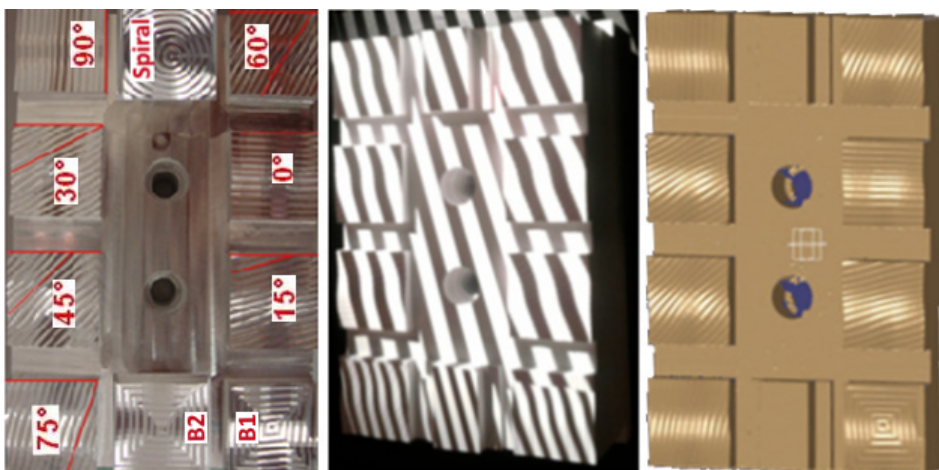


Fig. 8. Real part, fringe projection application and CAD model of machined surfaces

$$MRR = \frac{\int h(\phi, z) dA}{t_p}, h(\phi, z) = \frac{f(\phi, z) \cdot N_s(\phi, z)}{n_r N} \quad (1)$$

The chip volume varies according to the surface curvature, feed-rate, and cusp height generated via the

previous line of G code. ECD is the main factor used to calculate the required spindle speed and cutting inputs. ECD is explained as the real diameter of the cutter at the axial DoC- line.

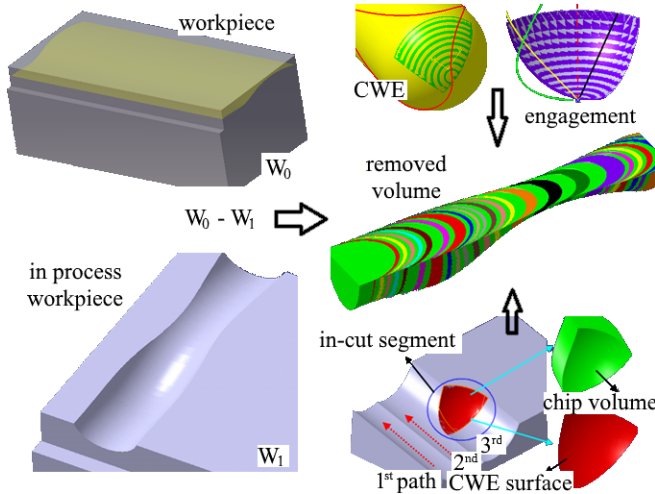


Fig. 9. Calculation of the removed volume, CWE, chip geometry, and workpiece in the developed simulation system

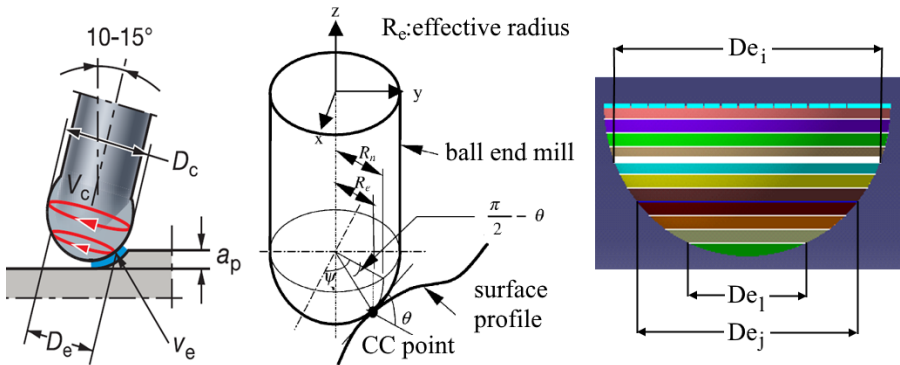


Fig. 10. Relationship between cutter effective radius and surface gradient [4]

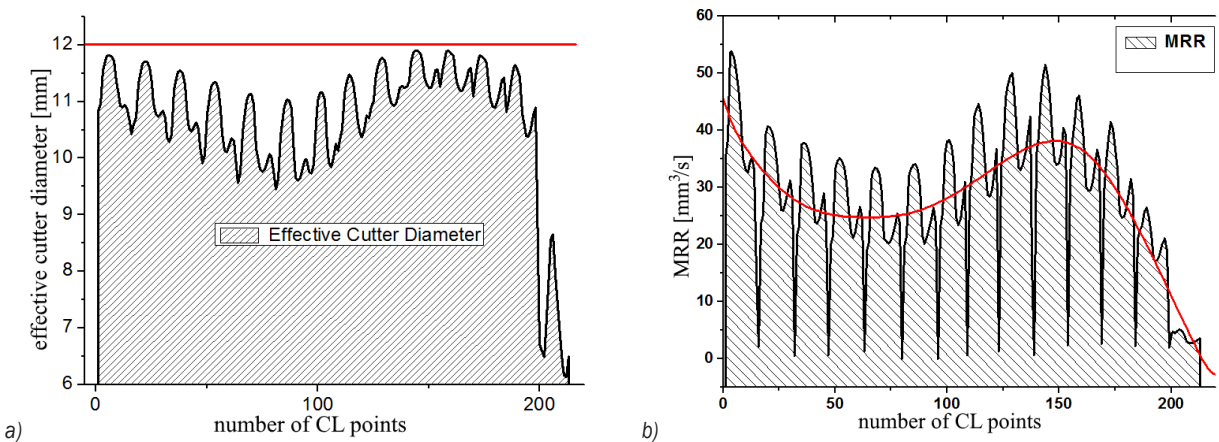


Fig. 11. a) ECD and b) IMRR values for 0° zig-zag tool path

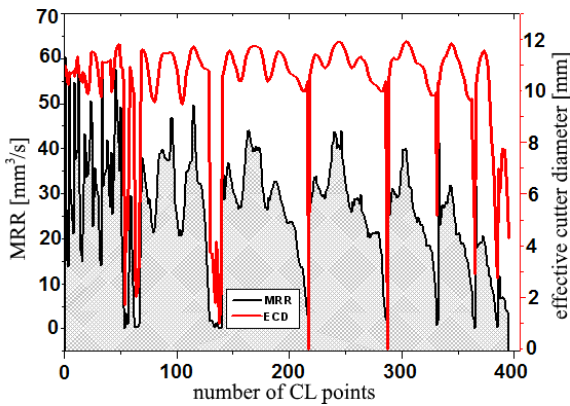


Fig. 12. MRR and ECD values for spiral cutting strategy

The ECD is affected by two factors: cutter radius and axial DoC values. ECD values at each CL point were directly obtained directly from the simulated B-rep interface as shown in Fig. 11. The ECD values during milling without tool inclination are calculated according to Eq. (2) [4] and [39]:

$$D_{eff} = 2 \cdot \sqrt{a_p \cdot (d - a_p)} \quad (2)$$

$$R_e = R_n \cos\left(\frac{\pi}{2} - \theta\right) \quad (3)$$

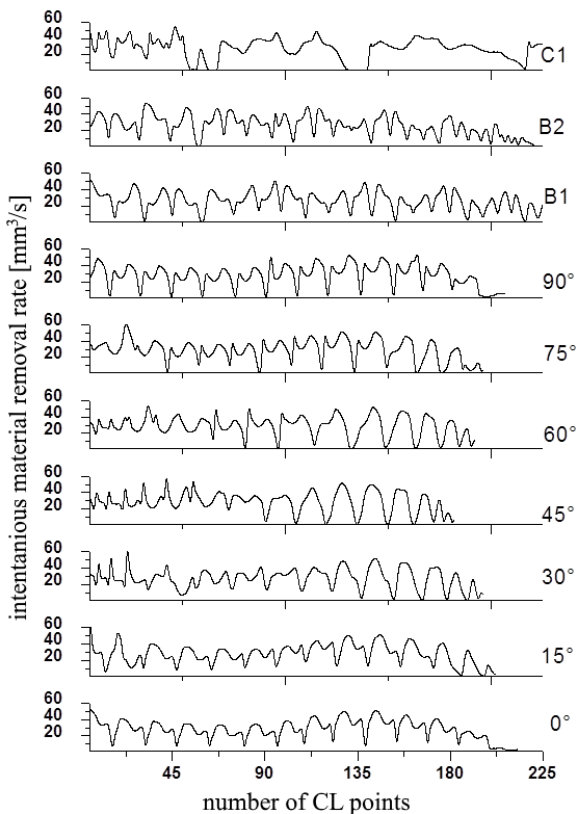


Fig. 13. IMRR values for tool-path strategies

In Eq. (2), the effective radius (the formula for  $R_e$  is given in Eq. (3), a horizontal distance measured from the rotation centre to the cutter contact point, of the ball-end milling tool varies according to the gradient  $\theta$  of the part surface [4]. It is seen that the IMRR and ECD results are very similar, as shown in Figs. 11 and 12. IMRR and ECD values were compared for the various cutting strategies as seen in Figs. 13 and 14. In free-form ball-end milling, depths of cut, ECD, and IMRR values are always changing at every CL point; therefore, different levels of form-errors are left on the sculptured surface. Fig. 11a shows variation of ECD values according to the nominal tool diameter value. ECD, IMRR, and cutting forces values showed similar tendencies.

## 2 RESULTS AND DISCUSSION

### 2.1 Analysis of Machining Time

Tool-path strategy has a considerable effect on the times required to machine curved surfaces. Complex

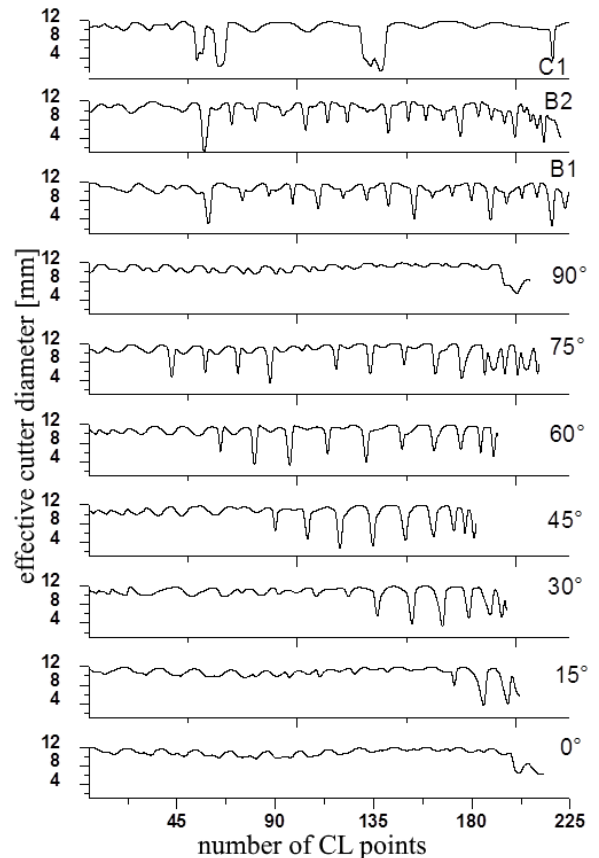


Fig. 14. ECD values for tool-path strategies for nominal cutter diameter (12 mm)

part surfaces generally need very long G code lines, resulting in extreme cutting times. Shorter cutting time means greater machining efficiency. Although various cutter paths have different cutting lengths, they remove a similar amount of chip. Removing an almost identical amount of workpiece material in a shorter time reduces the milling time, but has the negative effects of increasing forces, temperature, torque, cutter deflection and form errors. The machining time is measured for each strategy in all experiments as shown in Fig. 15. The 60° zig-zag strategy shows higher machining time and length cut in comparison to the other strategies. Furthermore, compared with the 60° zig-zag strategy, machining time could be reduced by employing a profile strategy (B1) at about 61 % and by using a spiral strategy at nearly 63 %. The results represent the effect of the path strategies on milling time.

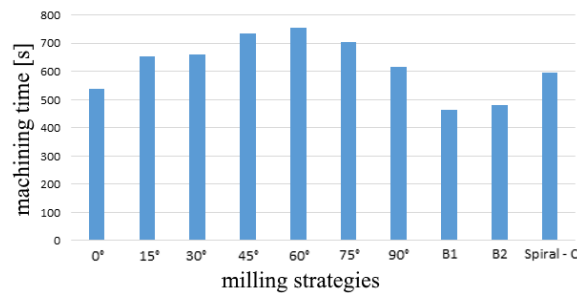


Fig. 15. Machining time for cutter path strategies

### 2.2 Analysis of Cutter Deflection, Forces and IMRR

Milling forces are the main factors governing dimensional accuracy, surface quality, machine vibration, spindle power requirements, energy consumption and cutter life. Proper selection of the cutter path strategy is crucial in achieving the desired machined surfaces.

Therefore, cutting force measurements are carried out to determine the effects of using different tool path strategies in the milling of convex surfaces. Different tool-path strategies are compared in terms of cutting force and tool deflection. The same surface was machined with various tool-paths. The experimental measurements and simulation results agree with each other. This permits engineers to analyse the milling process in advance, and to select the optimum path strategies.

Fig. 16 shows cutting forces and deflections from experiments using the different strategies. It is observed that when milling with a 75° zig-zag, the highest resultant cutting force and tool deflection

values are observed, followed by a 45° zig-zag and spiral and strategies, respectively. Employing profiling strategy (B1) achieves the lowest cutting force magnitude. Since the comparison between strategies takes place in the same machining conditions, tool-chip contact area is one of the reasons for cutting force differences between different strategies.

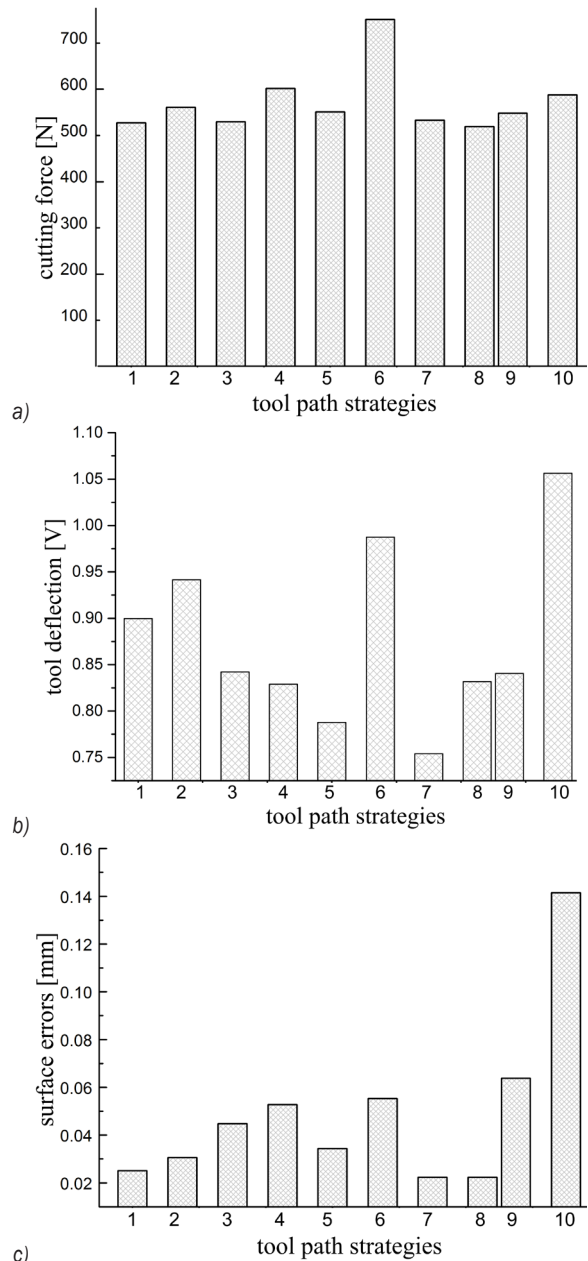


Fig. 16. Cutting forces(a), deflection (b) and max. surface errors values(c) for tool-path strategies

The minimum deflection of the tool occurs for the 90° zig-zag and profiling strategy (B1). The maximum removed volume values were shown as

seen in Fig. 17 for per cutter tooth and between two CL points. When the minimum force and minimum cutter deflection are taken into consideration, the 90° zig-zag strategy seems to be more productive. MRR and machining forces are closely related. MRR increases at nearly the same rates as increases in milling forces. The force calculation based on chip volume is very important to obtain accurate IMRR values during the roughing step. Milling forces obtained from experiments and the IMRR values from the B-rep approach were compared with each other. The IMRR and corresponding force profiles are very similar.

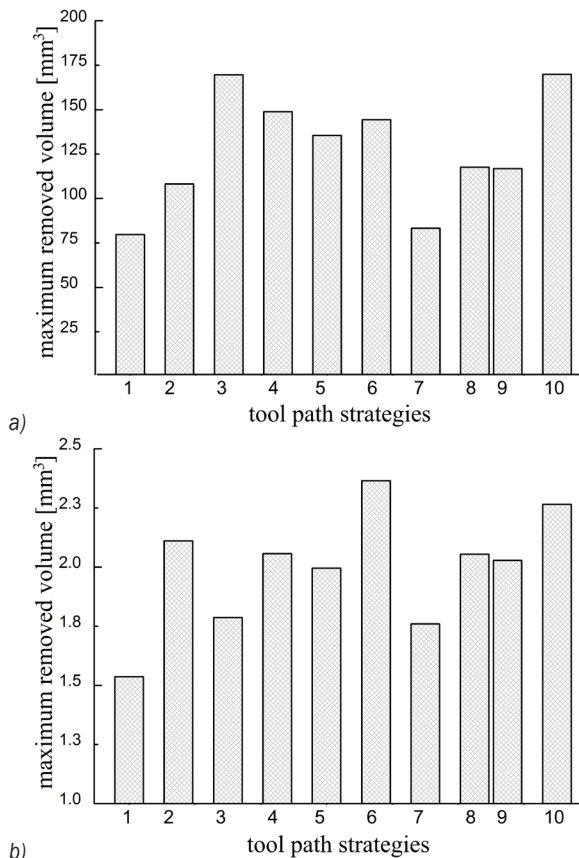


Fig. 17. a) Maximum removed volume values for CL points, and b) cutter per tooth

### 2.3 Analysis of Machining Errors

Errors in milled surfaces result from different factors, such as tool wear, thermal distortion, deflection of the machine tool and cutter, lubrication system, etc. Cutter deflection is the most critical of these parameters for surface form error. The influence of cutter strategies on surface form error was researched empirically. The surface dimensional error depends on the value and direction of the tool deflection. Cantilever beam

models were published in the literature. Assuming that the cutter behaves as a cantilever beam, Eq. (4) can be used to compute the resulting deflection [4]:

$$\delta = \left( \frac{64F}{3\pi E} \right) \left( \frac{L^3}{D^4} \right). \quad (4)$$

Some studies within the literature [40] and [41] examined milling errors caused by cutter deflection when machining a sculptured part using a ball-end milling tool. Wei et al. [41] examined a flexible model for estimating the form error in three-axis ball-end milling of the sculptured surface. In their work, the deflection-dependent cutting-edge engagement was determined by using an iterative procedure, and the form error was obtained from the balanced tool deflection and associated surface inclination angle. In these studies, tool deflection values were obtained using enhanced analytical force models. In this study, surface error results derived from the CAD model and NC simulation system. Tool-path lines, simulation output, real machined surface, and comparison of modelled and real machined surface are presented in Figs. 18 and 19 for the spiral and 0° zig-zag machining strategy, respectively. Firstly, the original CAD model created in the CATIA environment and the CAD data for the machined surface obtained via fringe projection were converted to the same coordinate system.

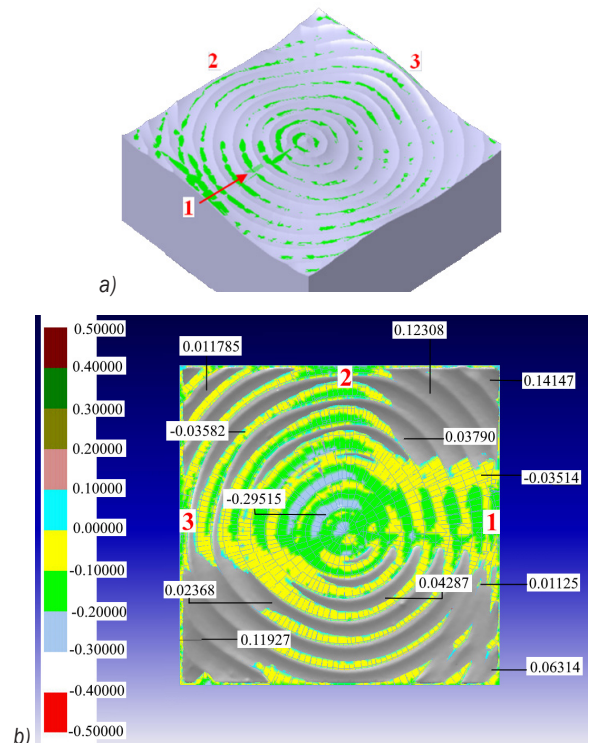


Fig. 18. Machining surface errors for spiral strategy

Then, the differences between the two CAD models were analysed. In addition, CAD data from B-rep simulation results and the desired target surface are compared with each other. The proposed simulation/analysis approach gives very good results in determining the location of manufacturing form errors. Cutting force values/machining errors and related cutter deflection/machining errors are shown in Fig 16. It is seen that the experimental measurements and simulation results agree with each other for path strategies. Deflection, force, and machining error values showed similar tendencies. Maximum surface errors value occurs in the spiral milling strategy as shown in Table 4.

**Table 4.** Maximal surface error values for path strategies

Tool Path Strategies	Max. Errors [ $\mu\text{m}$ ]	
Zig-Zag	0°	25.1
	15°	30.58
	30°	44.76
	45°	52.77
	60°	34.32
	75°	55.31
	90°	22.38
Concentric	on Part surface- B1	22.38
	on Plane- B2	63.87
Spiral	Spiral-C1	141.47

### 3 CONCLUSIONS

For this surface geometry, the 90° zig-zag tool-path gives better results in terms of surface error and tool deflection. Examined in detail, the highest form error values and cutter deflection are observed in the spiral and 75° zig-zag machining strategies. Deflection values are similar to the trends observed in the milling surface form errors. When the cutting strategies were compared, the cutter-work piece contact area, MRR, and ECD parameters were found to be excessive and subject to sudden changes. Therefore, application of these tool-path strategies results in the highest deflection, force, and form error. The results show that the minimum cutting force, machining errors and cutter deflection occur for the 0° and 90° zig-zag machining strategies.

The aim of this paper is to examine the effect of tool path strategies on cutting forces, tool deflection, real IMRR values, CWE, surface form errors and cycle times when milling a complex free-form surface. A B-rep solid modeling-based simulation and optimization system was developed and integrated with commercial CAD/CAM software for 3-axis ball-end milling. The 60° zig-zag strategy shows higher machining time and length cut in comparison to the other strategies. Furthermore, compared to the 60° zig-zag strategy, machining time could be reduced by employing profile strategy (B1) at about 61 % and by using the spiral strategy at nearly 63 %. Cutting forces and deflection values were obtained from experiments using the different strategies. It is observed that when milling with 75° zig-zag, the highest resultant cutting force and tool deflection values are observed, followed by 45° zig-zag and spiral and strategies, respectively. Employing profiling strategy (B1) achieves the lowest cutting force magnitude. Since the comparison between strategies takes place in the same machining conditions, the tool-chip contact area is one of the reasons for cutting force variations between different strategies. When the force and cutter deflection are taken into consideration, the 90° zig-zag strategy seems to be more productive.

MRR and machining forces are closely connected parameters. MRR increases at nearly the same rates as milling forces, IMRR, ECD and corresponding force profiles were found to be very similar for different strategies. Cutting force values/machining errors and the relationship between cutter deflection/machining errors were shown in Fig. 16. Deflection, force and machining errors showed similar variations. The in-house simulation system gave good results

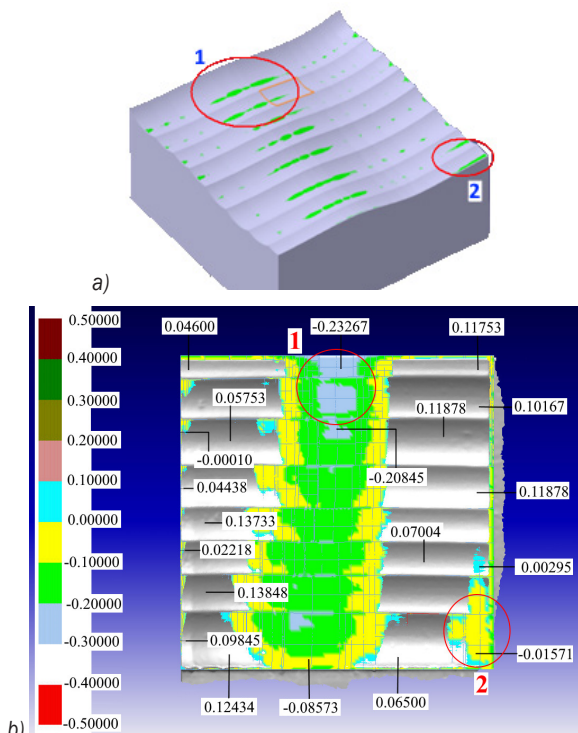


**Fig. 19.** Surface errors for 0° zig-zag milling strategy

in determining the location of manufacturing form errors, as seen in Figs. 18 and 19. As results, the maximum surface error was obtained from the profile tool-path and 45° zig-zag strategy, and there are proportional relationships between cutting force, deflection and form errors. It was observed that the profiles of deflection, IMRR values, cutting forces, machining errors, and ECD values match very well for cutting strategies. The results permit machinists or technicians to better evaluate the milling process for the selection of an efficient tool-path strategy.

#### 4 REFERENCES

- [1] Marshall, S., Griffiths, J.G. (1994). A survey of cutter path construction techniques for milling machines. *International Journal of Production Research*, vol. 32, no. 12, p. 2861-2877, DOI:10.1080/00207549408957105.
- [2] Dragomatz, D., Mann, S. (1997). A classified bibliography of literature on NC milling path generation. *Computer-Aided Design*, vol. 29, no. 3, p. 239-247, DOI:10.1016/S0010-4485(96)00060-7.
- [3] Gologlu, C., Sakarya, N. (2008). The effects of cutter path strategies on surface roughness of pocket milling of 1.2738 steel based on Taguchi method. *Journal of Materials Processing Technology*, vol. 206, no. 1-3, p. 7-15, DOI:10.1016/j.jmatprotec.2007.11.300.
- [4] Kurt, M., Bagci, E. (2011). Feedrate optimisation/scheduling on sculptured surface machining: a comprehensive review, applications and future directions. *The International Journal of Advanced Manufacturing Technology*, vol. 55, no. 9-12, p. 1037-1067, DOI:10.1007/s00170-010-3131-3.
- [5] Lasemi, A., Xue, D., Gu, P. (2010). Recent development in CNC machining of freeform surfaces: A state-of-the-art review. *Computer-Aided Design*, vol. 42, no. 7, p. 641-654, DOI:10.1016/j.cad.2010.04.002.
- [6] Chen, Y., Gao, J., Deng, H.G., Zheng, D., Chen, X., Kelly, R. (2013). Spatial statistical analysis and compensation of machining errors for complex surfaces. *Precision Engineering*, vol. 37, no. 1, p. 203-212, DOI:10.1016/j.precisioneng.2012.08.003.
- [7] Habibi, M., Arezoo, B., Nojehdeh, M.V. (2011). Tool deflection and geometrical error compensation by tool path modification. *International Journal of Machine Tools and Manufacture*, vol. 51, no. 6, p. 439-449, DOI:10.1016/j.ijmactools.2011.01.009.
- [8] Desai, K.A., Rao, P.V.M. (2008). Effect of direction of parameterization on cutting forces and surface error in machining curved geometries. *International Journal of Machine Tools and Manufacture*, vol. 48, no. 2, p. 249-259, DOI:10.1016/j.ijmactools.2007.08.007.
- [9] Albertí, M., Ciurana, J., Rodríguez, C.A. (2007). Experimental analysis of dimensional error vs. cycle time in high speed milling of aluminum alloy. *International Journal of Machine Tools and Manufacture*, vol. 47, no. 2, p. 236-246, DOI:10.1016/j.ijmactools.2006.04.009.
- [10] Erdim, H., Lazoglu, I., Kaymakci, M. (2007). Free-form surface machining and comparing feedrate scheduling strategies. *Machining Science and Technology*, vol. 11, no. 1, p. 117-133, DOI:10.1080/10910340601172206.
- [11] Kaymakci, M., Lazoglu, I. (2008). Tool path selection strategies for complex sculptured surface machining. *Machining Science and Technology*, vol. 12, no. 1, p. 119-132, DOI:10.1080/10910340801913979.
- [12] Brooks, Z., Nath, C., Kurfess, T.R. (2016). Investigating surface metrology of curved wall surface during milling of SS304 with different tool path strategies. *The International Journal of Advanced Manufacturing Technology*, vol. 86, no. 5-8, p. 1963-1972, DOI:10.1007/s00170-015-8323-4.
- [13] Gok, A., Gologlu, C., Demirci, H.I. (2013). Cutting parameter and tool path style effects on cutting force and tool deflection in machining of convex and concave inclined surfaces. *The International Journal of Advanced Manufacturing Technology*, vol. 69, no. 5-8, p. 1063-1078, DOI:10.1007/s00170-013-5075-x.
- [14] Shajari, S., Sadeghi, M.H., Hassanpour, H., Jabbaripour, B. (2012). Influence of machining strategies on surface roughness in ball end milling of inclined surfaces. *Advanced Materials Research*, vols. 488-489, p. 836-840, DOI:10.4028/www.scientific.net/AMR.488-489.836.
- [15] Vila, C., Abellán-Nebot, J.V., Siller-Carrillo, H.R. (2015). Study of different cutting strategies for sustainable machining of hardened steels. *Procedia Engineering*, vol. 132, p. 1120-1127, DOI:10.1016/j.proeng.2015.12.604.
- [16] Shajari, S., Sadeghi, M.H., Hassanpour, H. (2014). The influence of tool path strategies on cutting force and surface texture during ball end milling of low curvature convex surfaces. *The Scientific World Journal*, p. 1-14, DOI:10.1155/2014/374526.
- [17] Ižol, P., Vrabec, M., Maňková, I. (2016). Comparison of milling strategies when machining freeform surfaces. *Materials Science Forum*, vol. 862, p. 18-25, DOI:10.4028/www.scientific.net/MSF.862.18.
- [18] Matras, A., Kowalczyk, R. (2014). Analysis of machining accuracy during free form surface milling simulation for different milling strategies. *Proceedings of the SPIE*, vol. 9290, p. 1-7, DOI:10.1117/12.2075081.
- [19] Hassanpour, H., Shajari, S., Rasti, A., Sadeghi, M.H. (2015). Investigation of milling strategies effect on microhardness of a typical curved surface. *Modares Mechanical Engineering*, vol. 15, no. 2, p. 34-40.
- [20] Pahole, I., Studenčnik, D., Gotlih, K., Ficko, M., Balič, J. (2011). Influence of the milling strategy on the durability of forging tools. *Strojniški vestnik - Journal of Mechanical Engineering*, vol. 57, no. 12, p. 898-903, DOI:10.5545/sv-jme.2010.078.
- [21] Schützer, K., Abele, E., Stroh, C., Gyldenfeldt, C. (2007). Using advanced CAM-systems for optimized HSC-machining of complex free form surfaces. *Journal of the Brazilian Society of Mechanical Sciences and Engineering*, vol. 29, no. 3, p. 313-316, DOI:10.1590/S1678-58782007000300012.
- [22] Lazoglu, I., Manav, C., Murtezaoglu, Y. (2009). Tool path optimization for free form surface machining. *CIRP Annals - Manufacturing Technology*, vol. 58, no. 1, p. 101-104, DOI:10.1016/j.cirp.2009.03.054.
- [23] Zhang, X.F., Xie, J., Xie, H.F. (2012). Experimental investigation on various tool path strategies influencing surface quality and

- form accuracy of CNC milled complex freeform surface. *The International Journal of Advanced Manufacturing Technology*, vol. 59, no. 5-8, p. 647-654, DOI:10.1007/s00170-011-3515-z.
- [24] Wei, Z.C., Wang, M.J., Tang, W.C. (2013). Form error compensation in ball-end milling of sculptured surface with z-level contouring tool path. *The International Journal of Advanced Manufacturing Technology*, vol. 67, no. 9-12, p. 2853-2861, DOI:10.1007/s00170-012-4698-7.
- [25] Cao, Q.Y., Zhao, J., Zhu, L. (2016). The effect of curvature radius of sculptured surface on finish milling tool path selection. *The International Journal of Advanced Manufacturing Technology*, vol. 89, no. 9-12, p. 3349-3357, DOI:10.1007/s00170-016-9273-1.
- [26] Tan, L., Yao, C., Ren, J., Zhang, D. (2017). Effect of cutter path orientations on cutting forces, tool wear, and surface integrity when ball end milling TC17. *The International Journal of Advanced Manufacturing Technology*, vol. 88, no. 9-12, p. 2589-2602, DOI:10.1007/s00170-016-8948-y.
- [27] Uhlmann, E., Abackerli, A.J., Schützer, K., Lepikson, H.A., Helleno, A.L. Papa, M.C.O., del Conte, E.G., Mewis, J. (2014). Simulation and analysis of error impact on freeform surface milling. *The International Journal of Advanced Manufacturing Technology*, vol. 70, no. 1-4, p. 607-620, DOI:10.1007/s00170-013-5280-7.
- [28] Scandiffio, I., Diniz, A.E., de Souza, A.F. (2016). Evaluating surface roughness, tool life, and machining force when milling free-form shapes on hardened AISI D6 steel. *The International Journal of Advanced Manufacturing Technology*, vol. 82, no. 9-12, p. 2075-2086, DOI:10.1007/s00170-015-7525-0.
- [29] Tunc, L., Stoddart, D. (2017). Tool path pattern and feed direction selection in robotic milling for increased chatter-free material removal rate. *The International Journal of Advanced Manufacturing Technology*, vol. 89, no. 9-12, p. 2907-2918, DOI:10.1007/s00170-016-9896-2.
- [30] Scandiffio, I., Diniz, A.E., de Souza, A.F. (2017). The influence of tool-surface contact on tool life and surface roughness when milling free-form geometries in hardened steel. *The International Journal of Advanced Manufacturing Technology*, vol. 92, no. 1-4, p. 615-626, DOI:10.1007/s00170-017-0093-8.
- [31] Cao, Q., Xue, D., Zhao, J., Li, Y. (2011). A cutting force model considering influence of radius of curvature for sculptured surface machining. *The International Journal of Advanced Manufacturing Technology*, vol. 54, no. 5-8, p. 821-835, DOI:10.1007/s00170-010-2980-0.
- [32] Miao, Y., Song, X., Jin, T., Shan, Y. (2016). Improving the efficiency of solid-based NC simulation by using spatial decomposition methods. *The International Journal of Advanced Manufacturing Technology*, vol. 87, no. 1-4, p. 421-435, DOI:10.1007/s00170-016-8450-6.
- [33] Li, J.G., Ding, J., Gao, D. (2010). Quadtree-array-based workpiece geometric representation on three-axis milling process simulation. *The International Journal of Advanced Manufacturing Technology*, vol. 50, no. 5, p. 677-687, DOI:10.1007/s00170-010-2530-9.
- [34] Aras, E., Albedah, A. (2014). Extracting cutter/workpiece engagements in five-axis milling using solid modeler. *The International Journal of Advanced Manufacturing Technology*, vol. 73, no. 9-12, p. 1351-1362, DOI:10.1007/s00170-014-5853-0.
- [35] Lee, S.W., Nestler, A. (2012). Virtual workpiece: workpiece representation for material removal process. *The International Journal of Advanced Manufacturing Technology*, vol. 58, no. 5-8, p. 443-463, DOI:10.1007/s00170-011-3431-2.
- [36] Boz, Y., Erdim, H., Lazoglu, I. (2015). A comparison of solid model and three-orthogonal dexefield methods for cutter-workpiece engagement calculations in three- and five-axis virtual milling. *The International Journal of Advanced Manufacturing Technology*, vol. 81, no. 5-8, p. 811-823, DOI:10.1007/s00170-015-7251-7.
- [37] Defne Mühendislik. Design, from <http://www.defnemuhendislik.com/en.html>, accessed on 2015-06-26
- [38] Nehez, K. (2002). *Computer Simulation of the Milling Optimization*. University of Miskolc, Miskolc. (in Hungarian)
- [39] Sadilek, M., Čep, R., Budak, I., Soković, M. (2011). Aspects of using tool axis inclination angle. *Strojniški vestnik - Journal of Mechanical Engineering*, vol. 57, no. 9, p. 681-688, DOI:10.5545/sv-jme.2010.205.
- [40] Lim, E.M., Menq, C.H. (1997). Integrated planning for precision machining of complex surfaces. Part 1: Cutting-path and feed rate optimization. *International Journal of Machine Tools and Manufacture*, vol. 37, no. 1, p. 61-75, DOI:10.1016/0890-6955(95)00109-3.
- [41] Wei, Z.C., Wang, M.J., Cai, Y.J., Zhu, J.N., Wang, L. (2013). Form error estimation in ball-end milling of sculptured surface with z-level contouring tool path. *The International Journal of Advanced Manufacturing Technology*, vol. 65, no. 1-4, p. 363-369, DOI:10.1007/s00170-012-4175-3.

# Hysteresis Modelling and Compensation of Pneumatic Artificial Muscles using the Generalized Prandtl-Ishlinskii Model

Jiangping Mei – Shenglong Xie – Haitao Liu\* – Jiawei Zang

Tianjin University, Key Laboratory of Mechanism Theory and Equipment Design, China

The pneumatic artificial muscle (PAM) has attracted extensive attention from both industrial and academic fields due to its high power/weight ratio and significant compliance. However, the inherent hysteresis nonlinearities, including force-length and length-pressure hysteresis, have significant influence on the accuracy of trajectory tracking control. This paper presents a generalized Prandtl-Ishlinskii (GPI) model and its inversion for the asymmetric hysteresis characterization and compensation of the PAM. By using the Levenberg-Marquardt (L-M) method, the parameters in the proposed GPI model are identified, based on which the simulation result of the GPI model and the measured experimental data are compared to validate the identification. To compensate for the nonlinear length-pressure hysteresis, a feedforward/feedback combined control scheme is developed to realize highly accurate trajectory tracking control of the PAM. The experimental results show that the inverse GPI model has a good capability of compensating the asymmetric length-pressure hysteresis.

**Keywords:** hysteresis nonlinearity, generalized Prandtl-Ishlinskii (GPI) model, trajectory tracking control, Levenberg-Marquardt method

## Highlights

- The generalized Prandtl-Ishlinskii model is used to characterize the length-pressure hysteresis of a pneumatic artificial muscle.
- The numbers of generalized play operator in the proposed model are much smaller than those in the classical Prandtl-Ishlinskii model.
- The Levenberg-Marquardt method shows great efficiency for the identification of the parameters in the proposed model.
- The generalized Prandtl-Ishlinskii model can accurately describe the asymmetric hysteresis and has high accuracy in trajectory tracking of the pneumatic artificial muscle.

## 0 INTRODUCTION

The pneumatic artificial muscle (PAM), also called pneumatic muscle actuator (PMA) or fluidic muscle, is a tube-like pneumatic actuator, which consists of a flexible cylinder rubber surrounded by a braided mesh shell (see Fig. 1) [1].

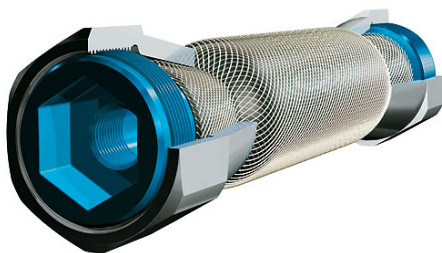


Fig. 1. The pneumatic artificial muscle

As a tensile actuator, the diaphragm of PAM extends in the circumferential direction when internal pressure is applied, resulting in a tensile force and a contraction motion in the longitudinal direction. The PAM has many advantages, including as simple structure, cleanliness, high power/weight ratio, low cost, etc. More importantly, the compliance [2]

of the PAM behaves very similarly to the organic muscle. This characteristic makes it widely used in rehabilitation, medical nursing and agriculture robots [3] and [4]. However, high-accuracy control of a PAM is by no means an easy task, due to the hysteresis phenomenon amongst length, pressure, and force [5], which makes the design of the controller complicated for an accurate trajectory control.

To eliminate the negative effects caused by hysteresis, extensive studies have been witnessed in recent years. The hysteresis models of the PAM can be roughly divided into two classes [6]: operator-based models and differential-based models. Members belonging to the first class use different kinds of mathematical operators to characterize the hysteresis phenomenon, including the Preisach model, Prandtl-Ishlinskii (PI) model and Maxwell-Slip model. Employing the stop operators, Ito et al. [7] and [8] derived the hysteresis model of the PAM to realize the motion control of a parallel manipulator. Minh et al. [1] developed a lumped-parametric quasi-static model based on the Maxwell-slip model to capture the force-length hysteresis, which can be easily used for the control of a PAM. Xie et al. [9] established the PI model to describe the length-pressure hysteresis of a PAM

\*Corr. Author's Address: Tianjin University, Key Laboratory of Mechanism Theory and Equipment Design, Weijin Road, Tianjin, 300072, China, liuht@tju.edu.cn

and derived the inverse model for trajectory tracking of a PAM by using fast-switching valves. Kosaki and Sano [10] described the length-pressure hysteresis using the Preisach model for the control of a parallel manipulator driven by three PAMs. The second class is based on the differential equations to characterize the hysteresis, such as the Duhem model, LuGre model, Bouc-Wen model, etc. In a similar manner, Lin et al. [11] investigated the hysteresis modeling and tracking control methods of the PAM by using the Bouc-Wen model, and designed different feedback control schemes for the compensation of hysteresis in order to reduce the tracking errors. Zhao et al. [12] applied the Duhem model to characterize the force-length hysteretic behaviour of the PAM, based on which a novel cascade position PID controller was designed to regulate the pressure. Zhong et al. [13] constructed the force-length hysteresis model in the form of the Bouc-Wen model, and developed a nonlinear PID control scheme to improve the kinematic performance of a manipulator actuated by PAMs. Aschemann and Schindele [14] adopted the generalized Bouc-Wen model, quasi-static Maxwell-slip model, and Prandtl-Ishlinskii model to establish the force-length hysteresis, and concluded that the first model was the most effective one for the control of a high-speed linear axis actuated by PAMs. Among these studies, the PI model is the most widely used due to the following advantages [11]: (1) the PI model contains a limited number of linear play operators; (2) both the PI model and the inverse PI model have analytical expressions. It must be pointed out that the conventional PI model is unable to describe the asymmetric characteristic of the hysteresis [15] and saturation [16], due to the symmetric property of the linear play operators. To solve this problem, asymmetric hysteresis modelling approaches, especially for smart materials, ferromagnetic materials and smart actuators, are intensively studied. Kuhen [17] proposed a modified PI model that combines linear play operators with dead-zone operators, which is capable of describing the asymmetric hysteresis of magnetostrictive actuators. Gu et al. [18] combined the conventional PI model with a nonlinear non-hysteretic function of the input to capture the asymmetric hysteresis of piezoceramic actuators. Janaideh et al. [19] proposed a generalized PI (GPI) model to characterize the saturated symmetric hysteresis loops of smart actuators. Zhang et al. [20] applied the GPI model to successfully describe the asymmetric hysteresis loops of Vanadium dioxide materials. However, few studies show the effectiveness of these variations of the PI model for PAMs except

for the investigation carried out by Liu et al. [21], in which a modified PI model was used to describe the asymmetric length-pressure hysteresis.

Drawing on the GPI model, this paper deals with the length-pressure hysteresis modelling and inverse GPI model compensation of PAMs. The rest of this paper is organized as follows. First, the experimental setup for measuring the length-pressure hysteresis and trajectory tracking control of a PAM is briefly introduced, followed by the formulation of the analytical forms of the GPI model and its inversion. Then the parameters in the model are identified using the Levenberg-Marquardt method, and the validation of the model is testified in comparison with the experimental measurements. Finally, an inverse-based compensator for trajectory tracking control of the PAM is designed to demonstrate the effectiveness of the model before conclusions are drawn in Section 5.

## 1 MEASUREMENTS OF THE LENGTH-PRESSURE HYSTERESIS OF A PAM

The experimental setup is shown in Fig. 2, and the components are listed in Table 1.



Fig. 2. Experimental setup

A PAM (FESTO DMSP-20-500) from FESTO is used for testing, of which one extremity is connected with the base and the other moves freely. The length and the internal pressure of the PAM are measured using a displacement sensor (Novotechnik TEX-0150) and a pressure transducer (FESTO SDE1-D10), respectively. A proportional pressure regulator (Festo VPPM-6L-L-1-G18-0L10H) is equipped to regulate the required pressure for the PAM. Fig. 3 shows the schematic diagram of the experimental setup.

The experimental process is given as follows. Initially, the PAM is at its full length, and the internal

**Table 1.** Components of the system

Component	Type	Parameters	Company
PAM	DMSP-20-500N	Length 500 mm, Diameter 20 mm Maximal permissible contraction 25 % Maximal additional load 80 kg	Festo
Proportional pressure regulator	VPPM-6L-L-1-G18-0L10H	Regulator range: 0 to 10 bar, Full scale linearity error $\pm 0.5\%$ Full scale repetition accuracy 0.5 %	Festo
Pressure sensor	SDE1-D10-G2-WQ4-L-PU	Max pressure 10 bar, Full scale accuracy $\pm 2\%$	Festo
Displacement sensor	TEX-0150-415-002-205	Measurement range 150 mm, Repeat accuracy $\pm 0.01$ mm	Novotechnik
Data acquisition card	PCI-6230	8 analogue input, 8 analogue output	NI

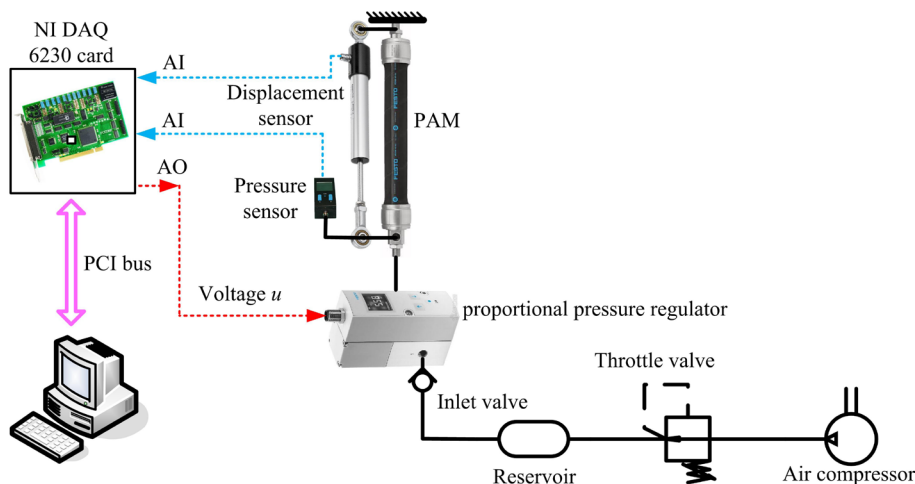


**Fig. 3.** Configuration of the experimental testing system

pressure is zero. The reference pressure signal is designed in the form of triangle-wave with a frequency of 0.2 Hz (see Fig. 4). Its amplitude decreases from 0.6 MPa to 0.1 MPa with an equal interval of 0.1 MPa. During the experiment, the contraction and internal pressure of the PAM are recorded. Fig. 5 shows the corresponding length-pressure hysteresis curve of the PAM, from which it can be seen that the

major hysteresis loop varies from 0 MPa to 0.6 MPa, and five minor hysteresis loops vary from 0 MPa to 0.5 MPa, 0.4 MPa, 0.3 MPa, 0.2 MPa, and 0.1 MPa, respectively. Obviously, given the same internal pressure, the contraction ratios of the PAM are different in the process of stretching and contraction. The measured data of the major hysteresis loop (see Fig. 5, red line) are used to identify the parameters in

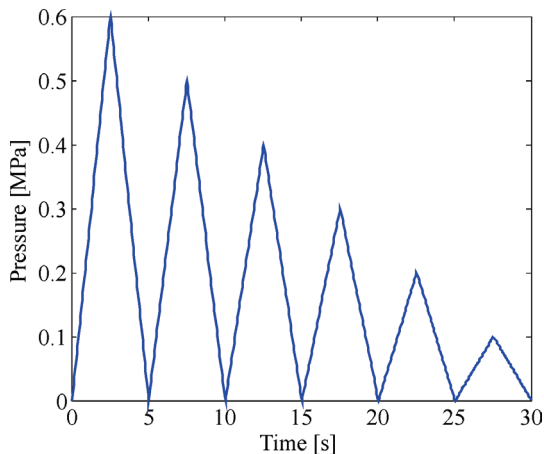


**Fig. 4.** The referenced input signal of pressure

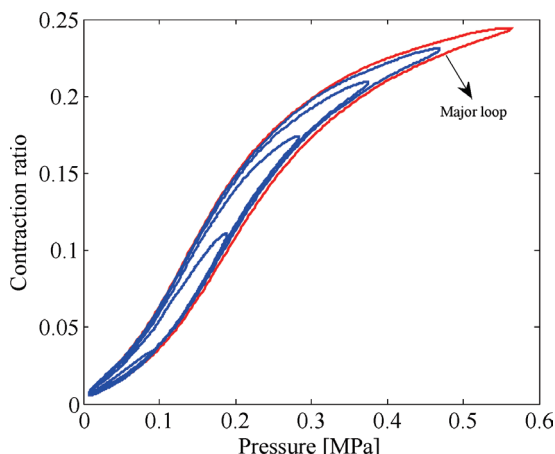


**Fig. 5.** Length/Pressure hysteresis of PAM

the GPI model that will be derived in the following section.

## 2 LENGTH-PRESSURE HYSTERESIS MODELLING

The analytical formulations of the GPI model and its inverse model are presented in this section. The former is used to characterize the length-pressure hysteresis, while the latter is applied as a feedforward compensator for trajectory tracking control.

### 2.1 The Classical PI Model

The classical PI model is a linearly weighted superposition of elementary play operators with different thresholds and weighting values. The input-output relationship of a linear play operator is illustrated in Fig. 6. Its envelop function is a straight line with a slope of one. Fig. 7 shows the superposition of a finite number of linear play operators to characterize the hysteresis in the discrete space. The expression of the  $i$ th linear play operator can be formulated as [22]:

$$y_i(k) = \max \{x(k) - r_i, \min \{x(k) + r_i, y_i(k-1)\}\}, \quad (1)$$

while the initial condition is:

$$y_i(0) = \max \{x(0) - r_i, \min \{x(0) + r_i, y_{i0}\}\}. \quad (2)$$

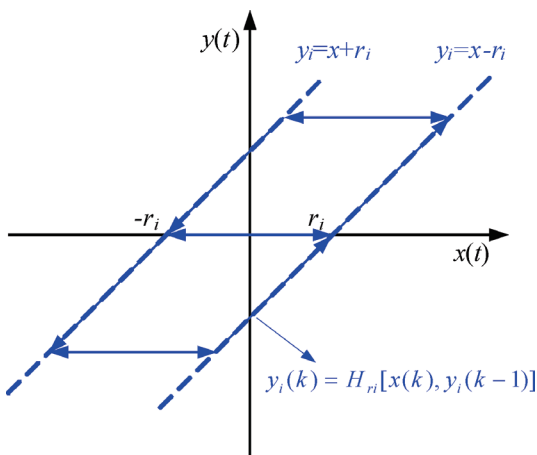


Fig. 6. The linear play operator

The output of the PI model can be written as:

$$y_p(k) = \sum_{i=1}^n \omega_i y_i(k) = \omega^T \mathbf{H}_r[x(k), \mathbf{y}_0] \quad (3)$$

where  $\mathbf{H}_r$  denotes the linear play operator;  $\omega = [\omega_1, \dots, \omega_n]^T$  is the weighting vector;  $\mathbf{r} = [r_1, \dots, r_n]^T$

is the threshold vector;  $x$  and  $y$  are the input and output of the operator, respectively;  $y_0$  is the initial state;  $n$  is the number of play operators. It has been shown that the conventional PI model cannot characterize asymmetric hysteresis loops of the PAM [21].

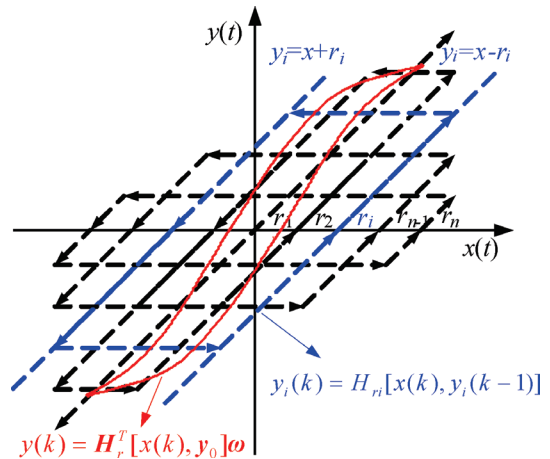


Fig. 7. The PI model

### 2.2 The Generalized PI Model

Due to the limitations of the conventional PI model, the GPI model [23] is employed to describe the length-pressure hysteresis behaviour of a PAM. The GPI model is expressed as a weighted superposition of generalized play operators. The input-output relationship of a generalized play operator is shown in Fig. 8. The  $i$ th generalized play operator can be mathematically expressed as:

$$y_i(k) = \max \{\gamma[x(k)] - r_i, \min \{\gamma[x(k)] + r_i, y_i(k-1)\}\}, \quad (4)$$

where  $\gamma[x(k)]$  is the envelop function of the generalized play operator. In this paper, the hyperbolic-tangent function is chosen to describe the output saturation under certain input, such that the envelop function can be given by:

$$\gamma = c_0 \tanh[c_1 x(k) + c_2] + c_3, \quad (5)$$

where  $c_0 > 0$ ,  $c_1 > 0$ ,  $c_2, c_3$  are constants to be identified. Thus, the GPI model can be formulated as:

$$y_p(k) = q\gamma[x(k)] + \sum_{i=1}^n p(r_i) y_i(k), \quad (6)$$

where  $q$  is a positive constant. According to [23], the threshold value  $r_i$  and the weight of the  $i$ th operator  $p(r_i)$  are given as:

$$r_i = \alpha i, \quad (7)$$

$$p(r_i) = \rho e^{-\tau r_i}, \quad (8)$$

where  $\alpha$ ,  $\rho$  and  $\tau$  are positive constants that need to be identified from experimental data.

Moreover, the inverse of the GPI model can be analytically expressed as:

$$x_p(k) = \gamma^{-1} \left( q'y(k) + \sum_{i=1}^n p'_i x_i(k) \right), \quad (9)$$

where the parameters in this model can be obtained following the conventional PI model and given as

$$x_i(k) = \max \{ y(k) - r'_i, \min \{ y(k) + r'_i, x_i(k-1) \} \}, \quad (10)$$

$$\begin{cases} q' = \frac{1}{q} \\ r'_i = qr'_i + \sum_{j=1}^{i-1} p_j (r_i - r_j) \\ p'_i = \frac{-p_i}{\left( q + \sum_{j=1}^i p_j \right) \left( q + \sum_{j=1}^{i-1} p_j \right)} \end{cases}, \quad (11)$$

where  $x_i(k)$  is the  $i^{\text{th}}$  inverse generalized linear play operator;  $r'_i$  and  $p'_i$  represent the  $i^{\text{th}}$  threshold and weight, respectively.

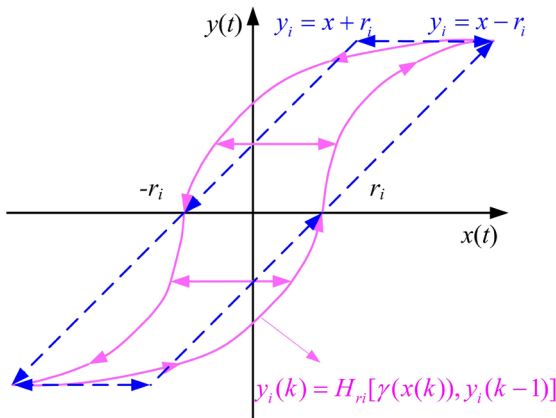


Fig. 8. The generalized play operator

### 3 PARAMETER IDENTIFICATION

In this section, the Levenberg-Marquardt (L-M) method is used to identify the parameters in the GPI model. Then the identified model is validated by comparing the simulation result and measured data.

### 3.1 The Levenberg-Marquardt Method

The nonlinear least-squares algorithm is a widely used technique in parameter estimation, which can be used to find the coefficients by minimizing a weighted cost function of the measured data. For this specific case, the following quadratic cost function is formulated:

$$F = \mathbf{E}^T(\boldsymbol{\Theta})\mathbf{E}(\boldsymbol{\Theta}) = \sum_{k=1}^N (y_i(k) - y_p(k, \boldsymbol{\Theta}))^2, \quad (12)$$

subject to

$$\begin{cases} y_p(k, \boldsymbol{\Theta}) = q\gamma[x_i(k)] + \sum_{i=1}^n p(r_i)y_i(k) \\ c_0 > 0, c_1 > 0, \rho > 0, \tau > 0 \end{cases}, \quad (13)$$

where  $\boldsymbol{\Theta} = [c_0, c_1, c_2, c_3, q, \rho, \tau, \alpha]^T$  is a set of identified parameters in the GPI model;  $\mathbf{E}(\boldsymbol{\Theta})$  is the error vector;  $x_i$  and  $y_i$  are input and output data obtained from the experiment;  $N$  is the number of  $x_i$ ;  $y_p$  is the output of the GPI model. The identification process can be expressed as [24]:

$$\boldsymbol{\Theta}_{k+1} = \boldsymbol{\Theta}_k - \mathbf{H}_k^{-1} \mathbf{J}_k^T \mathbf{E}_k, \quad (14)$$

where  $\mathbf{H}_k$  is the Hessian matrix, which is a square matrix of second-order partial derivatives of the error vector  $\mathbf{E}$  with respect to the parameter vector  $\boldsymbol{\Theta}$ ;  $\mathbf{J}_k$  is the Jacobian matrix that can be presented as:

$$\mathbf{J}_k = \begin{bmatrix} \frac{\partial E_1}{\partial \Theta_1} & \frac{\partial E_1}{\partial \Theta_2} & \dots & \frac{\partial E_1}{\partial \Theta_n} \\ \frac{\partial E_2}{\partial \Theta_1} & \frac{\partial E_2}{\partial \Theta_2} & \dots & \frac{\partial E_2}{\partial \Theta_n} \\ \vdots & \vdots & \dots & \vdots \\ \frac{\partial E_m}{\partial \Theta_1} & \frac{\partial E_m}{\partial \Theta_2} & \dots & \frac{\partial E_m}{\partial \Theta_n} \end{bmatrix},$$

$$\mathbf{E}_k = y_i(k) - y_p(k, \boldsymbol{\Theta}) = [E_1, E_2, \dots, E_n]^T,$$

where  $E_i$  is the error between the  $i^{\text{th}}$  output of the GPI model and the output data obtained from the experiment;  $\Theta_i$  is the  $i^{\text{th}}$  parameter of vector  $\boldsymbol{\Theta}$ ; and  $n=1$  for this particular case.

In order to improve the convergence of the solution, the Hessian matrix in Eq. (14) is expressed by:

$$\mathbf{H}_k = \mathbf{J}_k^T \mathbf{J}_k + \mu \mathbf{I}, \quad (15)$$

where  $\mu$  is called the combination coefficient, which is a damping parameter to approximate the Hessian matrix;  $\mathbf{I}$  is the identity matrix, which is applied to guarantee the approximated Hessian matrix to be

invertible all the time. Then, substituting Eq. (15) into Eq. (14) yields [25]:

$$\Theta_{k+1} = \Theta_k - (J_k^T J_k + \mu I)^{-1} J_k^T E_k, \quad (16)$$

which represents the parameter vector updating rule in each iteration. By using this method, the problem will converge to the optimal solution [24].

Table 2 lists the identified parameters of the GPI model (Eq. (6)) with ten generalized play operators ( $n=10$ ). Fig. 9 shows the comparison of the outputs of the identified GPI model with the measured data. It can be seen that the GPI model is effective in characterizing the asymmetric length-pressure hysteresis loops of the PAM.

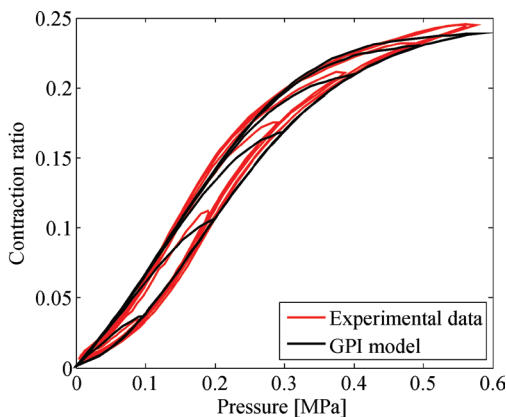


Fig. 9. Model validation result of the GPI model

Table 2. Identified parameters

$c_0$	$c_1$	$c_2$	$c_3$
1.428	0.418	-0.604	0.637
$q$	$\rho$	$\tau$	$\alpha$
0.047	0.042	5.001	0.08

#### 4 INVERSE GPI MODEL FOR COMPENSATION IN POSITION CONTROL OF PAM

To compensate the length-pressure hysteresis, a feedforward/feedback combined control strategy is

developed to realize highly accurate trajectory tracking control of the PAM. The feedforward compensator is designed based on the inverse GPI model in order to reduce the influence of length-pressure hysteresis, while the feedback controller is used to overcome the tracking error caused by creep and vibrations.

#### 4.1 Control Scheme

Given the identified parameters of the GPI model, the inverse GPI model can be obtained using Eqs. (9) to (11), which is then cascaded with the control system as a feedforward hysteresis compensator. The inverse GPI model maps the desired trajectory  $y_d$  into a desired control input signal  $P_d$  applied to the proportional pressure regulator. Hence, the relationship between the desired trajectory  $y_d$  and actual length  $y_r$  can be linearized. Note that the accuracy of the hysteresis model affects the performance of the feedforward controller. Therefore, a feedback loop must be added to form a feedforward/feedback combined controller. The control scheme is illustrated in Fig. 10. In this paper, a conventional PID controller is included in the feedback loop, which has the following form:

$$\Delta P = K_p e(t) + K_i \int_0^t e(\tau) d\tau + K_d \frac{de(t)}{dt}, \quad (17)$$

where  $e(t)$  is the tracking error signal;  $\Delta P$  is the output of PID controller;  $K_p$ ,  $K_i$ , and  $K_d$  are proportional, integral, and derivative gains, respectively, which are given in Table 3.

Table 3. Parameters of PID controller

$K_p$	$K_i$	$K_d$
0.05	0.01	0

#### 4.2 Experimental Results

To testify regarding the performance of the proposed control scheme, an experiment on trajectory tracking

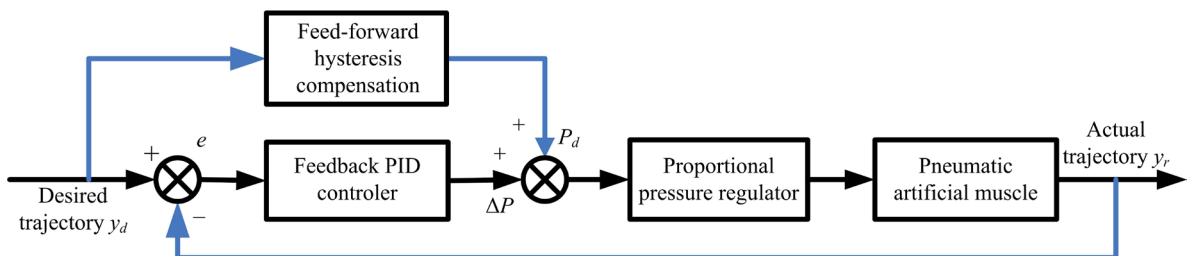


Fig. 10. Feedforward/feedback combined control scheme for pneumatic artificial muscle

control of the PAM is implemented. The desired sinusoidal tracking signal is designed as:

$$y_d(t) = A \sin(2\pi ft + \varphi) + L, \quad (18)$$

where  $y_d(t)$  is the desired trajectory signal output;  $A$  is the amplitude and  $\varphi$  is the initial phase;  $f$  and  $L$  are the frequency and offset of the desired signal, respectively. Table 4 gives the parameters in Eq. (18).

**Table 4.** Parameters of sinusoidal signal

$A$ [mm]	$f$ [Hz]	$\varphi$ [rad]	$L$ [mm]
45	0.2	$\pi/2$	450

**Table 5.** The tracking error of sinusoid trajectory

Maximum error [mm]	Mean absolute error [mm]	RMS error [mm]
2.659	0.7358	0.8701

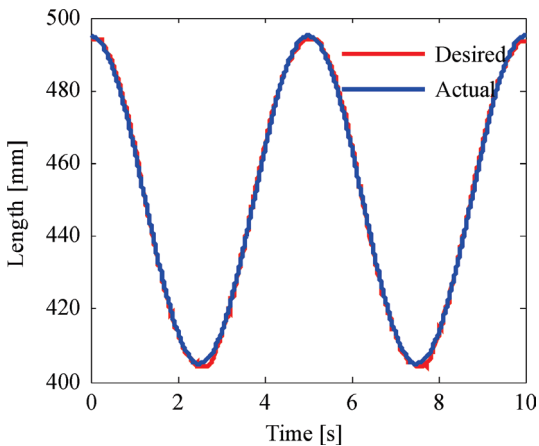


**Fig. 11.** Trajectory tracking responses

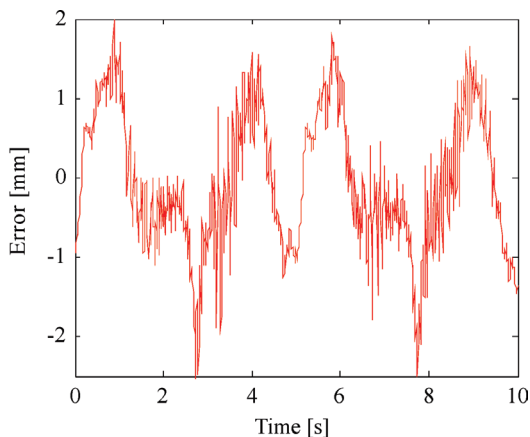


**Fig. 12.** Trajectory tracking errors

The tracking responses and errors of the proposed control scheme are shown in Figs. 11 and 12, respectively. Table 5 lists the statistics of the

trajectory tracking error. Numerical results show that the maximal error is 2.659 mm, and the mean absolute error is only 0.7358 mm. From the experimental results, it can be concluded that the inverse GPI model is very effective to compensate the effects of length-pressure hysteresis in real-time application. This conclusion can also be drawn from the nearly linear relationship between the desired and the actual lengths of the PAM after compensation (see Fig. 13).

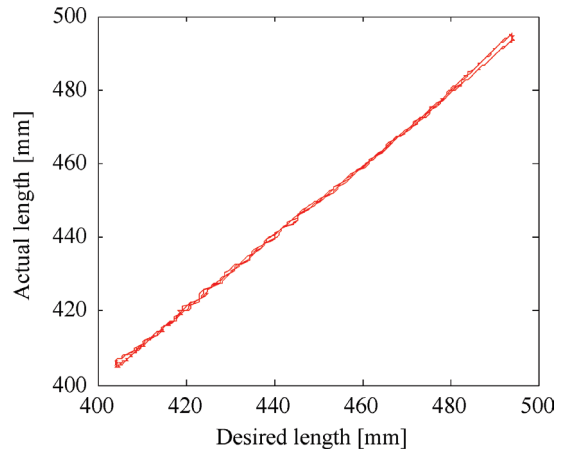


**Fig. 13.** Relationship between the desired length and the actual length after compensation

## 5 CONCLUSIONS

To capture the asymmetric length-pressure hysteresis of the PAM, a generalized Prandtl-Ishlinskii (GPI) model and its inverse model are presented in this paper. Compared to the classical Prandtl-Ishlinskii (CPI) model, the proposed GPI model utilizes the hyperbolic-tangent function as the envelope function of generalized play operators to characterize the asymmetric hysteresis loops. The parameters in the GPI model are identified by using the Levenberg-Marquardt method, making the process of identification convenient and efficient. Based on the inverse GPI model, a feedforward/feedback combined control scheme is developed to compensate the length-pressure hysteresis nonlinearity and realize high accurate trajectory tracking control of the PAM. The experimental results show that the proposed GPI model and its inversion are effective for describing the asymmetric length-pressure hysteresis of the PAM in terms of both major and minor hysteresis loops. However, since the symmetric envelop function is used in the generalized play operator, the capability of this model in characterizing the asymmetric hysteresis loops is limited. Therefore, the feedback controller

combined with the asymmetric GPI model-based feedforward compensator will be investigated in future work to further improve the trajectory tracking performance.

## 6 ACKNOWLEDGEMENTS

This work is supported by National Natural Science Foundation of China under Grant 51405331.

## 7 NOMENCLATURE

$x$  the input of the linear play operator or generalize play operator, [mm]  
 $y$  the output of the linear play operator or generalize play operator, [%]  
 $n$  the number of the linear play operator or generalize play operator  
 $y_i$  the  $i^{\text{th}}$  linear play operator or generalize play operator, [%]  
 $y_p$  the output of PI or GPI model, [%]  
 $\omega$  the weighting vector of PI model  
 $\mathbf{r}$  the threshold vector of PI model  
 $\mathbf{y}_0$  the initial state of the linear play operator or generalize play operator  
 $x_p$  the output of inverse GPI model, [MPa]  
 $x_i$  the  $i^{\text{th}}$  inverse generalize play operator  
 $r_i'$  the  $i^{\text{th}}$  threshold of the inverse GPI model  
 $p_i'$  the  $i^{\text{th}}$  weight of the inverse GPI model  
 $\gamma$  the envelope function of the generalize play operator  
 $c_0$  the constants of envelop function in GPI model  
 $c_1$  the constants of envelop function in GPI model  
 $c_2$  the constants of envelop function in GPI model  
 $c_3$  the constants of envelop function in GPI model  
 $q$  a positive constant of GPI model  
 $r_i$  the threshold value of the  $i^{\text{th}}$  generalize play operator  
 $p(r_i)$  the weight of the  $i^{\text{th}}$  generalize play operator  
 $\alpha$  the positive constant of  $r_i$   
 $\rho$  the positive constant of  $p(r_i)$   
 $\tau$  the positive constant of  $p(r_i)$   
 $F$  the quadratic cost function  
 $\Theta$  identified parameter vector in GPI model  
 $E$  the error vector  
 $x_t$  the input data obtained from experiment, [mm]  
 $y_t$  the output data obtained from experiment, [%]  
 $N$  the number of  $x_t$   
 $H_k$  the Hessian matrix, second-order partial derivatives of the error vector  $E$  with respect to the parameter vector  $\Theta$   
 $J_k$  the Jacobian matrix of the error vector  $E$  with respect to the parameter vector  $\Theta$

$\mu$  the combination coefficient  
 $I$  the identity matrix  
 $e(t)$  the tracking error signal, [mm]  
 $\Delta P$  the output of PID controller, [V]  
 $K_p$  the proportional gain  
 $K_i$  the integral gain  
 $K_d$  the derivative gain  
 $y_r$  the actual trajectory, [mm]  
 $P_d$  the desired control input signal, [V]  
 $y_d$  the desired trajectory signal, [mm]  
 $A$  the amplitude of  $y_d$ , [mm]  
 $f$  the frequency of  $y_d$ , [Hz]  
 $\varphi$  the initial phase of  $y_d$ , [rad]  
 $L$  the offset of  $y_d$ , [mm]

## 8 REFERENCES

- [1] Minh, T.V., Tjahjowidodo, T., Ramon, H., Van Brussel, H. (2011). A new approach to modeling hysteresis in a pneumatic artificial muscle using the Maxwell-slip model. *IEEE/ASME Transactions on Mechatronics*, vol. 16, no. 1, p. 177-186, DOI:10.1109/TMECH.2009.2038373.
- [2] Daerden, F., Lefeber, D. (2002). Pneumatic artificial muscles: actuators for robotics and automation. *European Journal of Mechanical and Environmental Engineering*, vol. 47, no. 1, p. 11-21.
- [3] Tondu, B., Ippolito, S., Guiochet, J., Daidie, A. (2005). A seven-degrees-of-freedom robot-arm driven by pneumatic artificial muscles for humanoid robots. *The International Journal of Robotics Research*, vol. 24, no. 4, p. 257-274, DOI:10.1177/0278364905052437.
- [4] Yeh, T.J., Wu, M.J., Lu, T.J. (2010). Control of McKibben pneumatic muscles for a power-assist, lower-limb orthosis. *Mechatronics*, vol. 20, no. 6, p. 686-697, DOI:10.1016/j.mechatronics.2010.07.004.
- [5] Minh, T.V., Kamers, B., Tjahjowidodo, T., Ramon, H., Van Brussel, H. (2010). Modeling torque-angle hysteresis in a pneumatic muscle manipulator. *Proceedings of the IEEE/ASME International Conference on Advanced Intelligent Mechatronics*, p. 1122-1127, DOI:10.1109/AIM.2010.5695805.
- [6] Hassani, V., Tjahjowidodo, T., Do, T.N. (2014). A survey on hysteresis modeling, identification and control. *Mechanical Systems and Signal Processing*, vol. 49, no. 1-2, p. 209-233, DOI:10.1016/j.ymssp.2014.04.012.
- [7] Ito, A., Kiyoto, K., Furuya, N. (2010). Motion control of parallel manipulator using pneumatic artificial actuators. *Proceedings of IEEE International Conference on Robotics and Biomimetics*, p. 460-465, DOI:10.1109/ROBIO.2010.5723370.
- [8] Ito, A., Washizawa, N., Kiyoto, K., Furuya, N. (2011). Control of pneumatic actuator in consideration of hysteresis characteristics. *Proceedings of IEEE International Conference on Robotics and Biomimetics*, p. 2541-2546, DOI:10.1109/ROBIO.2011.6181687.
- [9] Xie, S.L., Mei, J.P., Liu H.T., Wang, P.F. (2017). Motion control of pneumatic muscle actuator using fast switching valve. *Mechanism and Machine Science, Proceedings of ASIAN*

- MMS & CCMMS. p. 1439-1451, DOI:10.1007/978-981-10-2875-5\_114.
- [10] Kosaki, T., Sano, M. (2011). Control of a parallel manipulator driven by pneumatic muscle actuators based on a hysteresis model. *Journal of Environment and Engineering*, vol. 6, no. 2, p. 316-327, DOI:10.1299/jee.6.316.
- [11] Lin, C.J., Lin, C.R., Yu, S.K., Chen, C.T. (2015). Hysteresis modeling and tracking control for a dual pneumatic artificial muscle system using Prandtl-Ishlinskii model. *Mechatronics*, vol. 28, no. 6, p. 35-45, DOI:10.1016/j.mechatronics.2015.03.006.
- [12] Zhao, J., Zhong, J., Fan J.Z. (2015). Position control of a pneumatic muscle actuator using RBF neural network tuned PID controller. *Mathematical Problems in Engineering*, vol. 2015, art. ID. 810231, DOI:10.1155/2015/810231.
- [13] Zhong, J., Fan, J.Z., Zhu, Y.H., Zhao, J., Zhai, W.J (2014). One nonlinear PID control to improve the control performance of a manipulator actuated by a pneumatic muscle actuator. *Advances in Mechanical Engineering*, vol. 2014, art. ID. 172782, DOI:10.1155/2014/172782.
- [14] Aschemann, H., Schindele, D. (2014). Comparison of model-based approaches to the compensation of hysteresis in the force characteristic of pneumatic muscles. *IEEE Transactions on Industrial Electronics*, vol. 61, no. 7, p. 3620-3629, DOI:10.1109/TIE.2013.2287217.
- [15] Zhang, J., Merced, E., Sepúlveda, N., Tan, X.B (2015). Optimal compression of generalized Prandtl-Ishlinskii hysteresis models. *Automatica*, vol. 57, p. 170-179, DOI:10.1016/j.automatica.2015.04.012.
- [16] Janaideh, M.A., Rakheja, S., Su, C.Y. (2011). An analytical generalized Prandtl-Ishlinskii model inversion for hysteresis compensation in micropositioning control. *IEEE/ASME Transactions on Mechatronics*, vol. 16, no. 4, p. 734-744, DOI:10.1109/TMECH.2010.2052366.
- [17] Kuhnen, K. (2003). Modeling, identification and compensation of complex hysteretic nonlinearities: A modified Prandtl-Ishlinskii approach. *European Journal of Control*, vol. 9, no. 9, p. 407-418, DOI:10.3166/ejc.9.407-418.
- [18] Gu, G.Y., Zhu, L.M., Su, C.Y. (2014). Modeling and compensation of asymmetric hysteresis nonlinearity for piezoceramic actuators with a modified Prandtl-Ishlinskii model. *IEEE Transactions on Industrial Electronics*, vol. 61, no. 3, p. 1583-1595, DOI:10.1109/TIE.2013.2257153.
- [19] Janaideh, M.A., Mao, J., Rakheja, S., Xie, W., Su, C.Y. (2008). Generalized Prandtl-Ishlinskii hysteresis model: Hysteresis modeling and its inverse for compensation in smart actuators. *Proceedings of IEEE Conference on Decision and Control*, p. 5182-5187, DOI:10.1109/CDC.2008.4739202.
- [20] Zhang, J., Merced, E., Sepúlveda, N., Tan, X.B (2013). Optimal compression of a generalized Prandtl-Ishlinskii operator in hysteresis modeling. *Proceedings of ASME Dynamic Systems and Control Conference*, p. V003T36A005-V003T36A005, DOI:10.1115/DSCC2013-3969.
- [21] Liu, Y.X., Zang, X.Z., Lin, Z.K., Liu X.Y. (2017). Modelling length/pressure hysteresis of a pneumatic artificial muscle using a modified Prandtl-Ishlinskii model. *Strojniški vestnik - Journal of Mechanical Engineering*, vol. 63, no. 1, p. 56-64, DOI:10.5545/sv-jme.2016.4027.
- [22] Kuhnen, K., Janocha, H. (2001). Inverse feedforward controller for complex hysteretic nonlinearities in smart-material systems. *Control and Intelligent Systems*, vol. 29, no. 3, p. 74-83.
- [23] Janaideh, M.A., Rakheja, S., Su, C.Y. (2009) A generalized Prandtl-Ishlinskii model for characterizing the hysteresis and saturation nonlinearities of smart actuators. *Smart Materials & Structures*, vol. 18, no. 4, p. 1-9, DOI:10.1088/0964-1726/18/4/045001.
- [24] Li, M., Wu, H., Wang, Y., Handroos, H., Carbone, G. (2017). Modified Levenberg-Marquardt Algorithm for Backpropagation Neural Network Training in Dynamic Model Identification of Mechanical Systems. *Journal of Dynamic Systems, Measurement, and Control*, vol. 139, no. 3, p. 1-14, DOI:10.1115/1.4035010.
- [25] Yamashita, N., Fukushima, M. (2001). On the rate of convergence of the levenberg-marquardt method. *Computing Supplementa*, vol. 15, no. 1, p. 239-249, DOI:10.1007/978-3-7091-6217-0\_18.

# Analysis of Criteria for Determining a TNT Equivalent

Robert Panowicz\* – Marcin Konarzewski – Michał Trypolin

Military University of Technology, Department of Mechanical Engineering, Poland

The ConWep method is one of the most frequently used methods of modelling the effects of a blast wave impulse on a structure. The main goal of the study was to assess a TNT equivalent used in this approach. Six different methods to calculate this parameter for different explosive materials and charge shapes were analysed in this paper. The results error was lower than 20 % only when a TNT equivalent based on comparing the pressure impulses was used. This error can be lower only for spherical charges. In addition, for the tested distances (25 cm to 40 cm), TNT equivalents with an error margin of 5 % were assessed.

**Keywords:** TNT equivalent, ConWep, blast wave

## Highlights

- For assessing the effects of the blast wave on the structure, a ballistic pendulum was used.
- TNT equivalent was determined with the use of six different methods for two explosive materials: Semtex A1 and Composition B.
- Numerical analyses were conducted with ConWep and ALE approaches.
- Validation of the numerical model was performed.
- For the tested distances, TNT equivalents with an error margin of 5 % were assessed.

## 0 INTRODUCTION

Numerical analyses used to predict phenomena are always challenging. In the case of modelling the construction loads caused by blast waves, the challenges are related to the shape of the blast impulse and the method of describing its effects on the structure.

In the simplest cases, the dynamic load of the blast wave is realized through the use of a triangular pressure wave affecting the structure [1]. In such a situation, the maximal value of the wave corresponds to the maximal value of the pressure obtained from experimental tests, and the area under the experimental curve corresponds to the value of a pressure impulse. This method allows expressing the influence of the positive part of the blast wave.

For determining the parameters of the blast wave, experimental dependencies described by Henrych [2] and Sadoskiy [3] are often used.

Kingery and Bulmash [4], based on experimental data conducted with explosive charges made of trinitrotoluene (TNT), proposed dependencies describing the change of the pressure for reduced mass and distance. The results of their studies were implemented in many computer programs [5] to [7], also known as conventional weapon effects (ConWep). Apart from assessing the parameters of the blast wave, they also enable the determination of the influence of the pressure impulse on the structure. The ConWep method is one of the most frequently used methods of

modelling the effects of a blast wave impulse on the structure.

Difficulty appears when an explosive material other than TNT or with a shape other than spherical is used. When using other explosive materials, a so-called TNT equivalent is used. The TNT equivalent parameter is a value representing how much the mass of the charge needs to be multiplied by to obtain the same blast wave propagation. There is no definite method for calculating the TNT equivalent. Cooper used TNT equivalence based on a comparison of the velocities of detonation in accordance with the following equation [8]:

$$TNTEq = D_{exp}^2 / D_{TNT}^2, \quad (1)$$

where  $D$  is the velocity of detonation, subscripts  $exp$  and  $TNT$  are the studied explosive and TNT explosive, respectively.

One of the most frequently used methods of calculating the TNT equivalent is to determine it from the heat of detonation [9]:

$$TNTEq = Q_{exp} / Q_{TNT}, \quad (2)$$

where  $Q$  is the heat of detonation.

This method is recommended by the unified facilities criteria manuals (UFC) [10] in experiments where free air explosions are studied.

Eq. (2) was modified by Locking [9]:

$$NTEq = \frac{Q_{exp}}{(1-d)Q_{TNT} + m \cdot Q_{exp}}, \quad (3)$$

where  $d = 0.76862$  represents the Y-intercept of the straight curve of the heat of detonation TNT equivalent graph, and  $m = 0.7341$  the angular coefficient of the straight curve of the heat of detonation TNT equivalent graph.

Another equation for calculating the TNT equivalence was proposed in study [11] and is presented below:

$$TNT_{eq} = \frac{p_{CJ} + 20.9}{40}, \quad (4)$$

where  $p_{CJ}$  is the pressure of detonation [GPa].

The equations presented so far for determining the TNT equivalence were based on the available or easily obtainable material parameters. The more advanced methods shown below require more calculations or experimental tests to be conducted.

Another method is based on choosing, by trial and error, the TNT mass in such a way that the pressure values at a specified distance are equal [12] and [13]. Then, TNT equivalent is expressed by the following equation:

$$TNT_{eq} = \left( \frac{Z_{exp}}{Z_{TNT}} \right)^3, \quad (5)$$

where  $Z = R/\sqrt[3]{W}$  is the reduced distance from the explosive,  $R$  the distance from the explosive, and  $W$  the mass of the explosive charge.

The authors of study [12], when calculating the TNT equivalent, used an equation related to the equivalent pressure impulse at the specified distance:

$$TNT_{eq} = \left( \frac{W_{exp}}{W_{TNT}} \right)_I, \quad (6)$$

where  $W_{TNT}$  is the mass of TNT causing the equivalent, positive pressure impulse at the same distance as the mass  $W_{exp}$  of the material in question, and  $I$  the impulse.

When using non-spherical charges, it is often assumed that in comparably greater distances the pressure distribution would be similar to the spherical explosive where the detonation occurred centrally. Owing to this fact, the shape of the explosive is often omitted. The shape is indirectly referenced in Eqs. (5) and (6).

It results from the analysis of the detonation process and pressure wave propagation that the TNT equivalence value depends on: detonation speed, pressure, detonation energy and the number of moles of gaseous detonation products [14]. However, many experimental studies show that the adoption of a constant value of this parameter allows for the accurate determination of pressure impulse parameters,

although they may depend on the determination method [15]. In the range of reduced distances  $Z$  from  $8 \text{ m/kg}^{1/3}$  to  $27 \text{ m/kg}^{1/3}$ , the TNT equivalent TATP is equal to 0.7 and 0.55 for determination based on Eqs. (5) and (6), respectively [16]. The results presented in [17] showed that in the case of the C-4 explosive, the TNT equivalent is a nonlinear function of the reduced distance and a logarithm of the equivalent. In contrast, Rigby and Sielicki demonstrated, based on experimental research and numerical analysis, that the TNT equivalent value depends on the mass of the explosive charge mass [18]. However, the constant value of TNT equivalent for PE4 can be assumed to be suitable for both pressure and impulse equivalence, and that this value is also invariant of distance from the explosive.

Another aspect associated with TNT equivalent is a large spread of the published values of this parameter [19]. The typical spread of these values causes a 20 % to 30 % difference in blast wave parameter values.

The aim of the study is verification of the methods presented earlier Eqs. (1) to (6) for assessing the TNT equivalent. On the basis of the acquired TNT equivalent values, the mass of the TNT charges used in the ConWep numerical analyses was determined. In the next step, the numerical results of the ballistic pendulum tilt, which is the effect of blast wave interaction, determined with the use of 2 methods, were compared. The first method, validated and used as a reference, uses an arbitrary Lagrangian-Eulerian (ALE) with fluid-structure interaction (FSI) approach [18] and [6]. The other one, which is approximate, uses a ConWep approach with the determined earlier TNT mass.

The finite element method with an explicit integration was used to perform the numerical analyses. For this purpose, the authors used the LS-Dyna software [6].

The numerical analyses were conducted for spherical and cylindrical explosives with a mass of 50 g, with the explosives placed from 25 cm to 45 cm from the pendulum.

Before the proper analyses, the validation process of the ballistic pendulum numerical model, created with the use of the ALE with an FSI approach, was conducted. A good agreement with the experimental tests was achieved.

In Chapter 1 of the paper, the results of experimental tests used for validating the numerical model shown in Chapter 2 are presented. The results of the numerical analyses are presented in Chapter 3, and then briefly characterized in the summary.

## 1 EXPERIMENTAL TESTS

For assessing the effects of the blast wave on the structure, a ballistic pendulum was used. The test rig consists of the following parts (Fig. 1):

- double T-bar 220,
- two 300 mm × 300 mm steel plates, 10 mm thick, welded to the ends of the T-bar,
- eight distancing elements with a length of 200 mm constructed of threaded rods with a diameter of 24 mm,
- two 300 mm × 300 mm steel, removable plates, 20 mm thick,
- four steel ropes with a diameter of 5 mm,
- a frame consisting of closed steel profiles.

The dimensions of each part were selected in a way that allows the rig to work in the elastic range.

During the experiment, the frontal part of the pendulum was loaded dynamically by the blast wave caused by the detonation of the explosive. For the

test, Semtex A1 cylindrical explosives with a mass of 50 g and with  $L/D = 1$  ratio were used. The charges were placed on a light Styrofoam stand at a distance of 30 cm and 35 cm from the pendulum. The distance was measured from the front plate of the pendulum to the frontal part of the explosive.

For registering the tilt of the pendulum, fast camera Phantom V12 with tagged points (Fig. 2) was used. Recording of the process was conducted with no less than 2000 fps. The tilt of the pendulum, as registered by the camera, is shown in Fig 4. For the case in which the distance between the pendulum and the charge was 30 cm, the maximum tilt was equal to 75 mm. For the 35 cm distance, the maximum tilt was 64 mm.

## 2 NUMERICAL MODEL

In the numerical model, only the core parts of the pendulum were modelled: ropes, double T-bar,

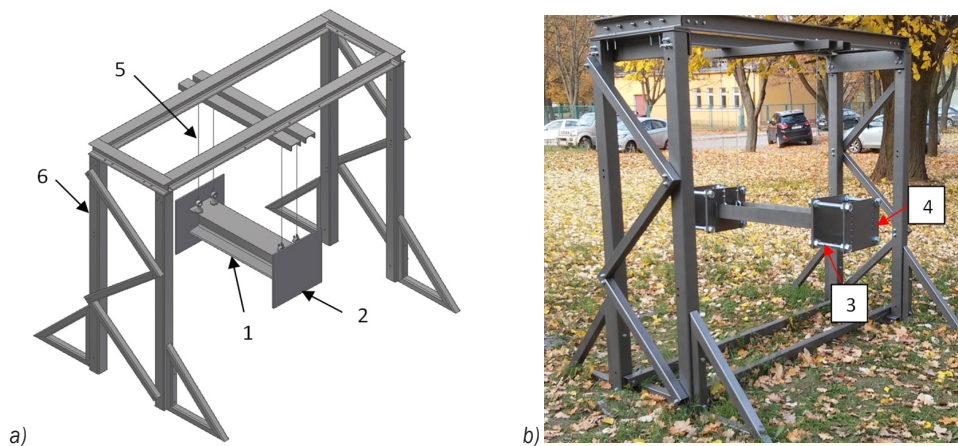


**Fig. 1.** a) Diagram of the test setup; and b) test rig;  
1 double T-bar, 2 steel plate, 3 distancing element, 4 steel, removable plate, 5 rope, 6 frame

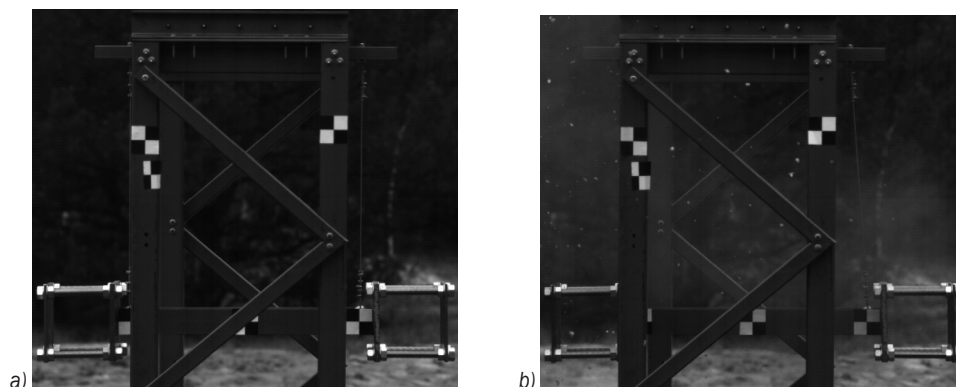


**Fig. 2.** Test rig during the experimental tests; a) initial position, b) tilt during the test with 50 g Semtex A1 cylindrical explosive  $L/D = 1$ , placed in the distance  $d = 30$  cm from the pendulum

plates and distancing elements (Fig. 3). The model consists of 4464 solid finite elements with 1 point of integration and 408 1D bar elements (ropes). For mechanical properties, an elastic material model was used, as shown in Table 1.

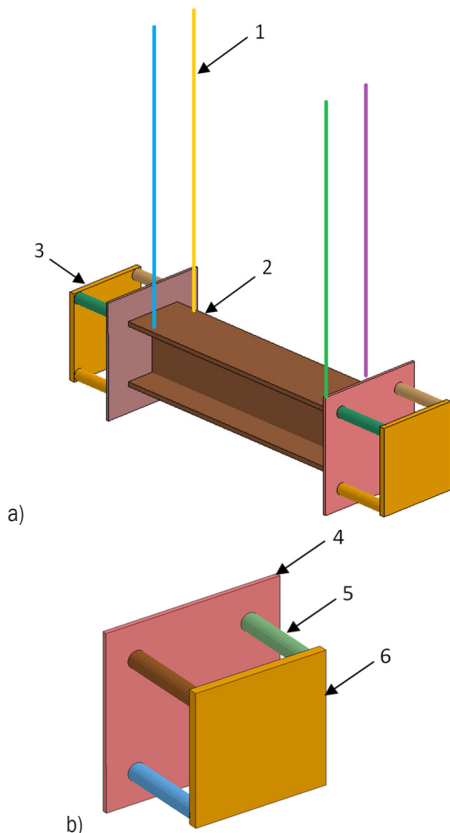


**Fig. 3.** a) Numerical model of the ballistic pendulum; b) close-up of the front part of the pendulum; 1 steel ropes, 2 double T-bar, 3 counter-weight, 4 front plate, 5 distancing elements, 6 removable front plate

The influence of the pressure wave caused by detonation of the explosive charge was realized using two methods. The first, which is considered as a referential one, uses the ALE method and the FSI coupling. This method is often used in many studies because it is characterized by high accuracy [20] and [21].

**Table 1.** Material parameters for elastic constitutive relationship

Parameter	Description	Unit	Value
$\rho$	Density	kg/m <sup>3</sup>	7.89E3
$E$	Young modulus	Pa	2.1E11
$\nu$	Poisson's ratio	-	0.3

The air domain was simulated using the Mie-Gruneisen equation:

$$p = p_0 + \gamma \rho E_{int} \quad (7)$$

where  $p$  is pressure,  $p_0$  initial pressure,  $\gamma$  Gruneisen coefficient,  $E_{int}$  internal energy.

Jones-Wilkins-Lee (JWL) equation was used for describing the behaviour of detonation products:

$$p = A \left( 1 - \frac{\omega}{R_1 V} \right)^{-R_1 V} + B \left( 1 - \frac{\omega}{R_2 V} \right)^{-R_2 V} \quad (8)$$

where  $V = \rho_0 / \rho$ ,  $\rho_0$  is initial density,  $\rho$  density of detonation products, and  $A, B, R_1, R_2, \omega$  are constants.

Material parameters used in the JWL equation are taken from literature [22] and are presented in Table 2.

The validation process of the developed numerical model was based on a comparative analysis of the profiles of experimental and numerical tilts of the ballistic pendulum. When comparing the results of the experimental test and the numerical analysis using the ALE with the FSI approach (Fig. 4), a high compatibility is visible. The maximal error in the considered cases was not higher than 2 % between the tilt obtained from the numerical analysis and the tilt obtained from the experimental test for the variant with the distance of 30 cm between the pendulum and the charge and 3 % with the distance of 35 cm. In both cases depicted, the tilt curves representing the experimental tests lie above the curves representing the numerical tests results.

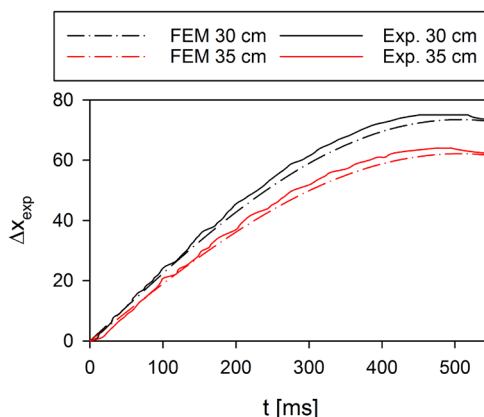


**Fig. 4.** Tilt of the ballistic pendulum for 50 g Semtex A1 cylindrical explosive (solid line – experiment, dashed line – FEM numerical results) for the distances 30 cm and 35 cm from the pendulum

### 3 RESULTS AND DISCUSSION

The numerical tests were conducted using two frequently used explosive materials, Comp B and Semtex A1. For those materials, the influence of

both the shape of the charge and the distance from the pendulum on the maximal tilt of the pendulum was also analysed. The tested charges, spherical and cylindrical, had shapes close to spherical ( $L/D = 1$ ).

As mentioned earlier, the results of analyses performed using the ALE with the FSI approach are considered as a reference.

The mass of the TNT used in the ConWep method calculations was derived from the TNT equivalent Eqs. (1) to (6) for 50 g explosive charges made from Comp B and Semtex A1 and located at a distance of 25 cm to 45 cm from the pendulum ballistic. This corresponds to a distance reduced from  $0.68 \text{ m/kg}^{1/3}$  to  $1.22 \text{ m/kg}^{1/3}$ . The maximum pressure values and pressure impulses needed to determine the TNT equivalents on the basis of Eqs. (5) and (6), respectively, were obtained from the numerical comparisons of the parameters (pressure, impulse) obtained from the numerical analysis using the ALE approach [15].

In the first step, analyses were performed for spherical and cylindrical explosives, made from Comp B and Semtex A1, recording pressure and impulse values at distances from 25 cm to 45 cm, every 5 cm. A number of similar numerical analyses were carried out for TNT charges with different weights. For the initial values, the average TNT mass, obtained using Eqs. (1) to (3), was assumed. The analyses were completed at the time when the relative difference between the pressure or impulse value obtained for the TNT load and test material was less than 2 %.

The results presented in Figs. 5 to 8 show maximal pendulum tilts obtained by ALE with FSI calculations and ConWep with TNT masses presented in Table 3 and distances from 25 cm to 45 cm (distance reduced from  $0.68 \text{ m/kg}^{1/3}$  to  $1.22 \text{ m/kg}^{1/3}$ ).

When analysing the curves showing the maximal tilt of the pendulum in function of the distance of the charge from the pendulum as calculated using numerical simulation with the use of ALE method

with FSI coupling, a clear influence of both the shape and the distance can be observed (Figs. 5 to 8 ALE). The influence is the lowest for the cylindrical charge made of Semtex A1.

The tilt of the pendulum for charges made of Comp B in the cases that used the ConWep method and Eq. (4) overestimates the tilt values regardless of a charge shape (Figs. 5 and 6). In all other cases, the curves are close to each other.

For cylindrical charges at the shortest considered distance (25 cm), the most significant difference between two values is 40 mm (33 %). In the case with the longest distance between the charge and the pendulum, the values decrease to 18 mm (29 %). Similar results were acquired for spherical charges. After excluding method 4, the values drop significantly. For cylindrical charges, the values decrease to 14 % and 6 % for 25 cm and 45 cm, respectively.

**Table 2.** Explosive materials parameters [16]

Parameter	Description	Unit	Semtex	Comp B
$\rho$	Density	[kg/m <sup>3</sup> ]	1400	1710
$D$	Detonation speed	[m/s]	7200	7980
$p_{CJ}$	C-J pressure	[GPa]	28	29.5
$A$	Explosive material constant	[GPa]	609	524.2
$B$	Explosive material constant	[GPa]	12.95	7.678
$R_1$	Explosive material constant	-	4.5	4.2
$R_2$	Explosive material constant	-	1.4	1.1
$\omega$	Explosive material constant	-	0.25	0.34

For both types of charges, the curve representing the ALE with the FSI method has a similar shape, however, the degree of the slope is different. This causes the cases with shortest distance between the pendulum and the charge to have a lower pendulum tilt than the ConWep method, and the longer distance cases to have a higher pendulum tilt than the ConWep method, regardless of the equation used, with the exception of the overall overestimation of Eq. 4. The

**Table 3.** Summary of numerical tests

Symbol	Equation	TNT mass corresponding to the 50 g explosive charge and the TNT equivalent value							
		Spherical Semtex A1 [g]	TNT equiv.	Cylindrical Semtex A1 [g]	TNT equiv.	Spherical Comp B [g]	TNT equiv.	Cylindrical Comp B [g]	TNT equiv.
A	1	54	1.08	54	1.08	66.3	1.326	66.3	1.326
B	2	20.25	0.405	20.25	0.405	55.6	1.112	55.6	1.112
C	3	91.5	1.83	91.5	1.83	63	1.26	63	1.26
D	4	48	0.96	48	0.96	90.4	1.808	90.4	1.808
E	5	80.1	1.602	82.3	1.646	64.15	1.283	70.8	1.416
F	6	65.5	1.31	65.15	1.303	59.6	1.192	59.55	1.191

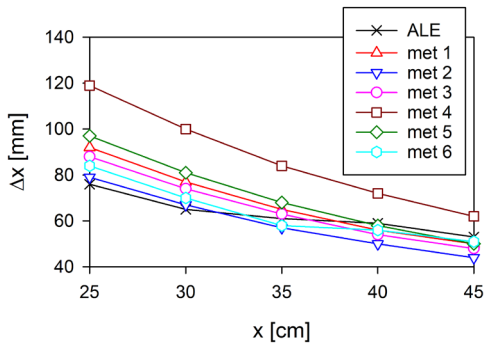


**Fig. 5.** Maximal tilt of the ballistic pendulum when affected by a blast wave caused by detonation of 50 g Comp B cylindrical explosive charge for different methods

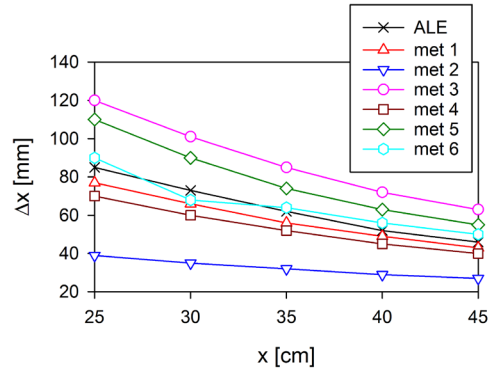


**Fig. 7.** Maximal tilt of the ballistic pendulum when affected by a blast wave caused by detonation of 50 g Semtex A1 cylindrical explosive charge for different methods

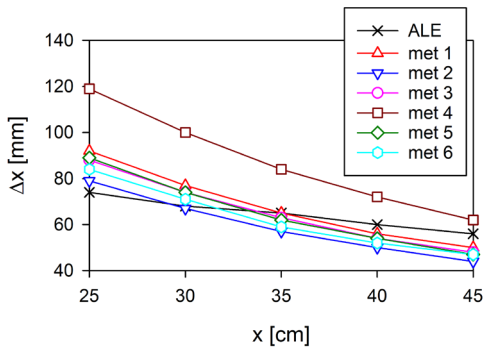


**Fig. 6.** Maximal tilt of the ballistic pendulum when affected by a blast wave caused by detonation of 50 g Comp B spherical explosive charge for different methods

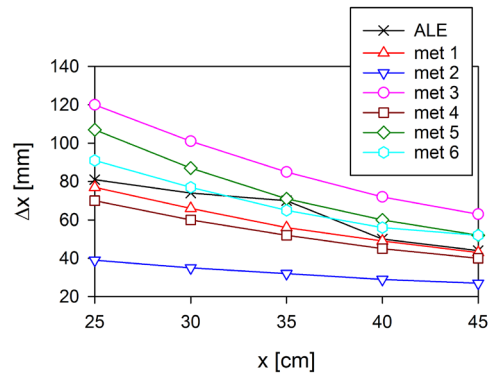


**Fig. 8.** Maximal tilt of the ballistic pendulum when affected by a blast wave caused by detonation of 50 g Semtex A1 spherical explosive charge for different methods

lowest mean error (10.5 %) for the pendulum tilt was achieved with Eq. (3) for cylindrical charges. Both Eqs. (3) and (6) achieve slightly above 11 % of error for spherical charges.

The curves representing Semtex A1 material are more apart from each other (Figs. 7 and 8), with values of 50 mm for a 25 cm distance and 36 mm for a 45 cm distance for both cylindrical and spherical charges.

The method based on the heat of detonation in Eq. (2) for this material results in underestimated tilt values.

The character of the curves presented in Figs. 7 and 8 is similar; therefore, the mean errors of the tilt equal to 6.3 % and 10 % for cylindrical and spherical charges, respectively, are lower when compared to Comp B material results. The highest accuracy in both cases is achieved with the equation based on comparing pressure impulses in Eq. (6).

In all considered cases, the dispersion of pendulum tilt values for shorter distances are

significantly higher than for longer distances (Figs. 5 to 8).

Table 4 shows the values of obtained TNT equivalents with maximal tilt errors not higher than 2 % for Semtex A1 and Comp B for both spherical and cylindrical charges. These values were obtained on the basis of an optimization process in which the objective function was to minimize the relative pendulum tilt, and the variable was TNT mass in the ConWep approximation in Eq. (9). As a reference, the pendulum tilt value obtained using the ALE with the FSI method was used in the calculations. Matlab software was used in the analyses.

$$\delta = \min \frac{\Delta x - \Delta x_{ALE}}{\Delta x_{ALE}}, \quad (9)$$

where  $\Delta x$  is maximal pendulum tilt obtained for ConWep approximation for a given mass of TNT,  $\Delta x_{ALE}$ , maximal pendulum tilt obtained for ALE with the FSI approach for the given explosives.

**Table 4.** TNT equivalence values for spherical and cylindrical charges made of Comp B and Semtex A1 based on optimization tests

Distance [cm]	Reduced distance [m/kg <sup>1/3</sup> ]	Comp B		Semtex A1	
		Cylinder	Sphere	Cylinder	Sphere
25	0.68	1.05	1.05	1.22	1.11
30	0.81	1.05	1.112	1.25	1.3
35	0.95	1.21	1.27	1.26	1.474
40	1.09	1.35	1.4	1.15	1.08
45	1.22	1.4	1.55	1.2	1.08

#### 4 CONCLUSIONS

The conducted tests clearly show that only a pressure impulse method for assessing the TNT equivalent yields errors lesser than 20 %, which is consistent with the results of work [15]. Lower error values can be achieved only with spherical charges. In other cases, it should be taken into account that the error will float around values no lower than 40 %.

Based on the compared data, TNT equivalents with 5 % error were assessed for spherical and cylindrical charges made of Comp B and Semtex A1. The value is a sum that results from comparing the ALE with the FSI methods to the experimental data and between the error of the ConWep method and the ALE with the FSI method.

#### 5 ACKNOWLEDGMENTS

This article was co-funded by The National Centre for Research and Development - project number DOBR-BIO4/022/13149/2013.

#### 6 REFERENCES

- [1] Syed, Z.I., Mohamed, O.A., Rahman, S.A. (2016). Non-linear finite element analysis of offshore stainless steel blast wall under high impulsive pressure loads. *Procedia Engineering*, vol. 145, p. 1275-1282, DOI:10.1016/j.proeng.2016.04.164.
- [2] Henrych J. (1979). *The Dynamic of Explosion and Its Use*. Elsevier Science Ltd., Prague.
- [3] Sadovskiy M. A., (2004). *Mechanical effects of air shockwaves from explosions according to experiments*. Geophysics and Physics of Explosion. Nauka Press, Moscow. (in Russian)
- [4] Kingery, C.N., Bulmash, G. (1984). *Airblast Parameters from TNT Spherical Air Burst and Hemispherical Surface Burst*. BRT Technical Report ARBRL-TR-02555. U.S. Army Armament Research and Development Center, Aberdeen.
- [5] Hyde, D.W. (1991). *Conventional Weapons Program (ConWep)*. U.S. Army Waterways Experimental Station, Vicksburg.
- [6] Hallquist, J.O. (2005). *Ls-Dyna Theory Manual*. Livermore Software Technology Corporation, Livermore.
- [7] Dharmasena, K.P., Wadley, H.N.G., Xue, Z., Hutchinson, J.W. (2008). Mechanical response of metallic honeycomb sandwich panel structures to high-intensity dynamic loading. *International Journal of Impact Engineering*, vol. 35, no. 9, p.1063-1074, DOI:10.1016/j.ijimpeng.2007.06.008.
- [8] Cooper, P.W. (1994). *Comments on TNT Equivalence*. 20<sup>th</sup> International Pyrotechnics Seminar.
- [9] Locking, P.M. (2011). *The Trouble with TNT Equivalence*. 26<sup>th</sup> International Symposium on Ballistics.
- [10] UFC 3-340-02 (2008). *Structures to Resist the Effects of Accidental Explosions*. Unified Facilities Criteria.
- [11] Bajić, Z. (2007). *Determination of TNT Equivalent for Various Explosives*. MSc thesis, University of Belgrade, Faculty of Technology and Metallurgy, Belgrade. (in Serbian)
- [12] Formby, S.A., Wharton, R.K. (1996). Blast characteristics and TNT equivalence values for some commercial explosives detonated at ground level. *Journal of Hazardous Materials*, vol. 50, no. 2-3, p. 183-198, DOI:10.1016/0304-3894(96)01791-8.
- [13] Simoens, B., Lefebvre, M., Minami F. (2011). Influence of Different Parameters on the TNT-Equivalent of an Explosion. *Central European Journal of Energetic Materials*, vol. 8, no. 1, p. 53-67.
- [14] Sochet, I., Gardebas, D., Calderara, S., Marchal, Y., Longuet, B. (2011). Blast wave parameters for spherical explosives detonation in free air. *Open Journal of Safety Science and Technology*, vol. 1, p. 31-42, DOI:10.4236/ojsst.2011.12004.
- [15] Ackland, K., Bornstein H., Lamos, D. (2012). An analysis of TNT equivalencies using AUTODYN. *Journal of Explosion Engineering*, vol. 1, no. 3, p. 80-88.
- [16] Pachman, J., Matyáš, R., Künzel, M. (2014). Study of TATP: blast characteristics and TNT equivalency of small charges. *Shock Waves*, vol. 24, no. 4, p. 439-445, DOI:10.1007/s00193-014-0497-4.
- [17] Bogosian, D., Yokota, M., Rigby, S.E. (2016). TNT equivalence of c-4 and pe4: a review of traditional sources and recent data. *Proceedings of the 24<sup>th</sup> Military Aspects of Blast and Shock*, Halifax, p. 19-23.
- [18] Rigby, S.E., Sielicki, P.W. (2014). An Investigation of TNT Equivalence of Hemispherical PE4 Charges. *Engineering Transactions*, vol. 62, no. 4, p. 423-435
- [19] Locking, P.M. (2011). The trouble with TNT equivalence. *26<sup>th</sup> International Ballistics Symposium*, p. 143-154.
- [20] Panowicz R., Nowak J., Konarzewski M., Niezgoda T. (2015). Parametric studies of directed fragmentation warhead used for combat shaped charges. *Engineering Transactions*, vol. 63, no. 2, p. 181-190.
- [21] Chung Kim Yuen, S., Langdon, G.S., Nurick G.N., Pickering, E.G., Balden, V.H. (2012). Response of V-shape plates to localised blast load: Experiments and numerical simulation. *International Journal of Impact Engineering*, vol. 46, p. 97-109, DOI:10.1016/j.ijimpeng.2012.02.007.
- [22] Włodarczyk, E. (1994). *Introduction to Shock Waves*. PWN, Warsaw. (in Polish)

# Modelling of the Relationship of Adiabatic Shear and Cutting Conditions for Higher Cutting Speed Ranges

Guohe Li\* – Yujun Cai – Houjun Qi – Meng Liu

Tianjin University of Technology & Education, Tianjin Key Laboratory of High-speed Cutting & Precision Machining, China

The serrated chip is a typical characteristic of high-speed cutting due to the occurrence of adiabatic shear. Based on an adiabatic shear sensitivity index proposed via linear perturbation analysis, which considers the pressure-shear condition in machining, the relationship of adiabatic shear and cutting conditions is established. The corresponding relation between the cutting conditions and the deformation conditions is established based on the model of a parallel boundary shear zone. The influence of cutting parameter on adiabatic shear is analysed, and the results show that the adiabatic shear in high speed machining tends to occur under the condition of higher cutting speed, greater depth of cut and smaller rake angle. An orthogonal cutting experiment was performed to validate the proposed model. Furthermore, the influence mechanism of cutting conditions on adiabatic shear is discussed in detail, and one application of the model is introduced.

**Keywords:** high speed machining, adiabatic shear, linear perturbation analysis, cutting parameter

## Highlights

- The relationship of adiabatic shear and cutting conditions was established.
- The influence of cutting parameter on adiabatic shear is analysed.
- An orthogonal cutting experiment was carried out to validate the proposed model.

## 0 INTRODUCTION

High-speed machining (HSM) has a series of advantages, such as smaller cutting force, higher precision, better surface quality, higher productivity, lower cost, and it can be used for difficult-to-process materials. Therefore, it is extensively applied in the fields of aerospace, automotive and moulding, etc., and is widely used [1]. The main difference between high speed cutting and conventional cutting is that the serrated chip is often produced in high speed cutting [2] and [3], and the continuous chip is produced in conventional cutting. Fig. 1 shows diagrams of a continuous chip and serrated chip. Although some scholars ascribed the occurrence of serrated chips to a periodic crack initiated in the free surface of the workpiece ahead of the tool [4] and [5]. Other researchers, including Recht [6], Komandui [7], Davies [8], Molinari [9] and Ma [10], attributed the formation of serrated chips to a repeated thermo-plastic instability occurring in the primary shear zone, particularly for ductile materials [2] and [11]. On one side, the occurrence of adiabatic shear in high speed cutting will increase the tool wear and influence the quality of the finished surface. On the other side, it is beneficial to the rupture of chip and favourable automation machining. Therefore, in order to control the cutting process effectively, more attention should be paid to the adiabatic shear localization in HSM.

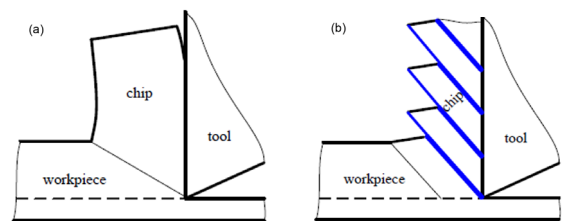


**Fig. 1.** Sketch map of chip:  
a) continuous chip, and b) serrated chip

Extensive research has been conducted on adiabatic shear in the machining of various materials. Sun et al. [12] examined the chip formation during the dry turning of Ti6Al4V in association with dynamic cutting force measurements under different cutting speeds, feed rates, and depths of cut. Huang et al. [13] carried out the perturbation analysis of thermo-viscoplastic instability in chip formation to establish the relation for the segment spacing which was obtained by multiplying the chip flow velocity by the characteristic time of instability. Duan and Zhang [14] presented an in-depth investigation into the formation mechanisms and microstructures of adiabatic shear bands (ASBs) in hardened AISI 1045 steel induced by HSM. A systematic analysis, both experimental and theoretical, showed that a low cutting speed led to deformed ASBs, and a high cutting speed resulted in transformed ASBs. Molinari et al. [15] investigated the role of cutting conditions on adiabatic shear banding and chip serration by combining

finite element calculations and analytical modelling. Miguélez et al. [16] focused on the numerical analysis of adiabatic shear banding in orthogonal cutting of Ti6Al4V alloy. The influence of cutting velocity and feed in chip segmentation was studied. Moreover, the role of friction at the tool-chip interface and the effect of rheological parameters of the constitutive equation were analysed. Gu et al. [17] investigated the damage evolution mechanism of adiabatic shear localized fracture (ASLF) in chip formation under an optical microscope and scanning electron microscope (SEM) through an HSM experiment of hardened AISI 1045 steel at a relatively high cutting speed. They further investigated the induced mechanism of adiabatic shear fracture and the corresponding damage process in high-speed machining through quick-stop tests and chip morphology examinations [18]. On the basis of saturation limit model, the critical fracture energy was predicted by cutting conditions and compared with the experimental results. Ye et al. [3] set up an experimental device, based on the light-gas gun technology, to realize high speed cutting over a wide range of cutting speed from 30 m/s to 200 m/s. High-speed cutting experiments were performed on AISI 1045 steel. The investigation of chip morphology, micro-structure, micro-hardness and the finished surface integrity were carried out. Furthermore, they performed the cutting experiments on Ti6Al4V alloy over a wide range of cutting speed [19]. The transition of chip morphology from continuous to serrated was observed with increasing the cutting speeds. A new theoretical model was developed to predict the segment spacing, in which the momentum diffusion due to unloading within the shear band had been considered. They also proposed an explicit expression of the critical cutting speed for the onset of serrated chip flow, which is given in terms of material properties, uncut chip thickness and tool rake angle, based on dimensional analysis and numerical simulations. It could give reasonable predictions of the critical cutting speeds at which chips change from continuous to serrated chip for various metallic materials over wide ranges of uncut chip thickness and tool rake angle [20]. Recently, Ye et al. [21] systematically analysed the experimental results of high-speed cutting on various typical metallic materials over wide ranges of cutting speeds. By considering the coupling effects of inertial, tool-chip compression and material convection, the critical condition for the onset of serrated chip flow was determined based on a stability analysis of the deformation inside the primary shear zone. It is found that the emergence of the serrated chip flow is dominated by a dimensionless number

that characterized the competition among the effects of inertia, thermal softening, strain hardening, elastic unloading, viscous diffusion and thermal diffusion. Wang et al. [22] studied the formation condition of continuous and saw-tooth chips and various characteristics of the saw-tooth chip, such as cutting speed, feed rate, axial depth of cut, and others. The results showed that the chip of materials with different hardness could be controlled to the continuous chip through the optimization of a combination of cutting speed, feed per tooth, and depth of cut. Wu and Sandy [23] investigated the cutting mechanism of a new emerging high temperature and high strength titanium alloy named TC21 using the finite element method (FEM), a modified high temperature split Hopkinson pressure bar (SHPB) test system was employed to obtain the stress-strain curves of TC21 alloy under different temperatures and strain rates. Jomaa et al. [24] developed a 2D FEM based on a Lagrangian approach for simulating and analysing the serrated chip formation during HSM of the AA7075-T651 alloy. Wang and Liu [25] presented an investigation of chip morphology from the viewpoint of a chip-free surface and cross-section. The research showed that the microstructure of chip-free surface evolves from lamellae to folds and then to dimples. According to the experimental results, a new model of serrated chip formation based on mixed mode of ductile fracture and adiabatic shear was proposed. They further investigated the influence mechanism of stress triaxiality on the serrated chip formation during HSM [26]. The fracture loci of ASBs in serrated chips under different cutting speeds have been obtained and validated by experimental results. The research has proven that the stress triaxiality plays a vital role in serrated chip formation during HSM. They also found that the chip serrated frequencies for the two work-piece materials during HSM are found to be nearly equal to their corresponding AE-dominant frequencies [27]. These pioneering works give important indications to study the influence of cutting parameters on adiabatic shear in HSM.

In the next section, the pressure-shear stress state of the primary shear zone to build the continuum mechanics basic equations of machining is considered. An adiabatic shear sensitivity index is proposed by linear perturbation analysis. In Section 2, the model of deformation conditions in shear plane AB based on the model of parallel boundary shear zone is presented so as to build the corresponding relations between the deformation conditions and the cutting parameters of orthogonal cutting (i.e. cutting speed, depth of cut, and rake angle). In Section 3, AISI 1045 steel is taken as an

example to analyse the influence of cutting parameter on adiabatic shear according to the adiabatic shear sensitivity index. An orthogonal cutting experiment was carried out and the changes of chip with cutting parameters were shown to validate the analysis results in Section 4. The influence mechanism of cutting parameters on adiabatic shear is discussed in detail in Section 5. The concluding remarks of the paper are Section 6.

1 ADIABATIC SHEAR SENSITIVITY INDEX

It is usually thought that the deformation in HSM is a plane strain because the width of cut  $a_w$  is far greater than the depth of cut  $a_c$ . Stable cutting is assumed and the built-up edge is neglected. The narrow zone in Fig. 2, named as CAEFBD, is the primary shear zone with length of  $2l$  and width of  $s$ . Where the CD plane and EF plane are the upper and lower boundaries of the primary deformation zone respectively. The AB plane in the middle of the primary deformation zone, is the shear plane. The deformation in each plane that is parallel to AB is homogeneous. The inclination between the shear plane AB and cutting speed  $V$  is the shear angle  $\phi$ .  $\gamma_1$  is the rake angle of cutting tool.  $\tau_{CD}$ ,  $\tau_{AB}$  and  $\tau_{EF}$ , are the shear stress of CD, AB, and EF plane, respectively.  $\sigma_{AB}$  is the compression stress of shear plane AB.  $F_r$  is the cutting force.  $F_s$  and  $F_{ns}$  are the component forces along and perpendicular to the shear direction, respectively.  $F_r'$  is the reaction force of  $F_r$ .  $F_f$ , and  $F_n$  are the friction force and pressure force on rake face. Therefore, there is a pressure-shear stress state in the primary deformation zone, as shown in Fig. 3.

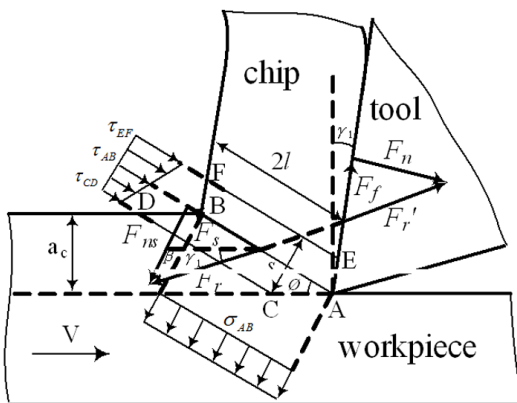


Fig. 2. Model of orthogonal high-speed machining

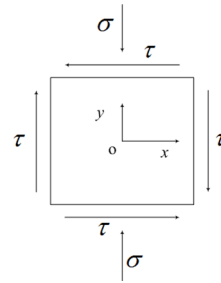


Fig. 3. Stress state of the primary shear zone

According to the stress state of the primary deformation zone, the basic foundations of continuum mechanics in HSM for the coordinate system in Fig. 3 are as follows,

$$\begin{cases} \rho \frac{\partial v_x}{\partial t} = \frac{\partial \tau}{\partial y} \\ \rho \frac{\partial v_y}{\partial t} = \frac{\partial \sigma}{\partial x} \\ \rho c \frac{\partial T}{\partial t} = k \frac{\partial^2 T}{\partial y^2} + \beta \sigma \frac{\partial v_y}{\partial y} + \beta \tau \frac{\partial v_x}{\partial y} \end{cases}, \quad (1)$$

where  $v_x$ ,  $v_y$  are the velocity component,  $\tau$  is the shear stress,  $\sigma$  is the compressive stress,  $T$  is the temperature,  $\rho$  is the density,  $c$  is the thermal capacity,  $k$  is the thermal conductivity,  $\beta$  is the Taylor-Quinney coefficient,  $t$  is time and  $x$ ,  $y$  are coordinate axes. According to material mechanics,  $\dot{\gamma} = (\partial v_x / \partial y) + (\partial v_y / \partial x)$  and  $\dot{\epsilon} = (\partial v_x / \partial x) + (\partial v_y / \partial y)$ , and in the primary deformation zone,  $\partial v_y / \partial x = 0$  and  $\partial v_x / \partial x = 0$ , so  $\dot{\gamma} = \partial v_x / \partial y$ , and  $\dot{\epsilon} = \partial v_y / \partial y$ . The constitutive relation is expressed as  $\tau = f(\gamma, \dot{\gamma}, T)$ . Thus, the equation can be expressed by,

$$\begin{cases} \rho \frac{\partial^2 \gamma}{\partial t^2} = \frac{\partial \tau}{\partial y} \\ \rho \frac{\partial^2 \epsilon}{\partial t^2} = \frac{\partial \sigma}{\partial y} \\ \rho c \frac{\partial T}{\partial t} = k \frac{\partial^2 T}{\partial y^2} + \beta \sigma \frac{\partial \epsilon}{\partial t} + \beta \tau \frac{\partial \gamma}{\partial t} \end{cases}. \quad (2)$$

The linear perturbation analysis of Eq. (2) is carried out, and more detail can be seen in [28]. Then the homogeneous system of equations,

$$\begin{cases} [\rho \alpha^2 + (Q_0 + R_0 \alpha) k'^2] \gamma - P_0 k'^2 T_0 = 0 \\ [\rho \alpha^2 + (Q_0 + R_0 \alpha) k'^2] \epsilon - P_0 k'^2 T_0 = 0 \\ [\beta \tau_0 \alpha + \beta \dot{\gamma}_0 (Q_0 + R_0 \alpha)] \gamma + [\beta \sigma_0 \alpha + \beta \dot{\epsilon}_0 (Q_0 + R_0 \alpha)] \epsilon - \\ - (\beta \dot{\gamma}_0 P_0 + \beta \dot{\epsilon}_0 P_0 + \rho c \alpha + k k'^2) T_0 = 0 \end{cases}, \quad (3)$$

$$\begin{vmatrix} \rho\alpha^2 + (Q_0 + R_0\alpha)k'^2 & 0 & -P_0k'^2 \\ 0 & \rho\alpha^2 + (Q_0 + R_0\alpha)k'^2 & -P_0k'^2 \\ \beta\tau_0\alpha + \beta\dot{\gamma}_0(Q_0 + R_0\alpha) & \beta\sigma_0\alpha + \beta\dot{\varepsilon}_0(Q_0 + R_0\alpha) & \beta\dot{\gamma}_0P_0 + \beta\dot{\varepsilon}_0P_0 + \rho c\alpha + kk'^2 \end{vmatrix} = 0. \quad (4)$$

where  $\gamma_*$ ,  $\tau_*$ ,  $T_*$ ,  $\varepsilon_*$ ,  $\sigma_*$  is the amplitude,  $\alpha$  is the growth rate and  $k'$  is the wave number.

To guarantee the existence of non-trivial solutions for  $\gamma_*$ ,  $\varepsilon_*$  and  $T_*$ , the determinant of the coefficients matrix in Eq. (3) should be zero: specifically presented in Eq. (4).

This leads to the characteristic cubic equation:

$$\rho^2 c \alpha^3 + \rho [\beta P (\dot{\gamma}_0 + \dot{\varepsilon}_0) + (k + cR_0)k'^2] \alpha^2 + [kR_0k'^2 + \rho cQ_0 - \beta(\tau_0 + \sigma_0)P_0]k'^2 \alpha + kQ_0k'^4 = 0. \quad (5)$$

This is a spectral equation. A positive real root of  $\alpha$  implies that instability is possible. The criterion condition of the adiabatic shear in high-speed cutting can be given through the discussion of the stability of spectral equation [28], and as follows:

$$B = \frac{\eta P_0 \sqrt{\sigma^2 / 3 + \tau^2}}{\rho c Q_0} - 2 \sqrt{\frac{\eta k P_0 \dot{\gamma}_0}{\rho c^2 Q_0}} \geq 1. \quad (6)$$

Eq. (6) shows that the influence factors of adiabatic shear in HSM are material characteristics and deformation conditions. The value of parameter  $B$  reflects the degree of adiabatic shear evolution and can be taken as the adiabatic shear sensitivity index. The deformation condition of HSM is determined by cutting parameters. If the corresponding relations between the cutting parameters and the deformation conditions can be established, the relationship between cutting parameters and adiabatic shear can be given.

## 2 MODEL OF DEFORMATION CONDITION IN THE PRIMARY SHEAR ZONE

We can use the method of lattice line or streamline to get the distribution of strain rate in machining. The analysis results of these two methods showed that the distribution of the strain rate in the primary shear zone nears to a quadratic curve [29] and [30], as shown in Fig. 4.

If the coordinate of Fig. 5 is adopted, the strain rate distribution in the primary shear zone can be expressed as follows:

$$\dot{\gamma}(z) = \frac{2aV \sin \phi}{\left[ (s/2 - z)^2 + (s/2)^2 \right]^{3/2}}, \quad (7)$$

where  $s$  is the width of the primary shear zone, and

$$a = \frac{s^2}{16 \sin^2 \phi (tg \gamma_1 + ctg \phi)}.$$

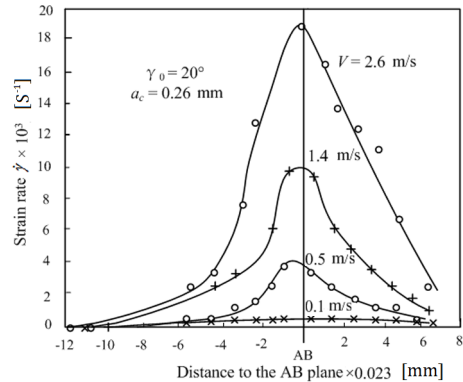


Fig. 4. Strain rate distribution

From Fig. 4, we can see that the strain rate of AB plane is maximum. According to the adiabatic shear theory, the adiabatic shear should occur in AB plane first. Therefore, in this paper, the deformation conditions of AB plane are taken as that leads to the adiabatic shear in HSM.

On the AB shear plane,  $z = s/2$ , so the strain rate of AB plane can be calculated as follows:

$$\begin{aligned} \dot{\gamma}_{AB} &= \frac{2aV \sin \phi}{\left[ \left( \frac{s}{2} - \frac{s}{2} \right)^2 + \left( \frac{s}{2} \right)^2 \right]^{3/2}} = \\ &= \frac{2V \sin \phi \times s^2}{\frac{s^2}{8} \times 16 \sin^2 \phi (tg \gamma_1 + ctg \phi)} = \frac{V \cos \gamma_1}{s \cos(\phi - \gamma_1)}. \quad (8) \end{aligned}$$

When Eq. (8) is used to calculate the strain rate of AB plane, in the first place, the width of the primary shear zone  $s$  and the shear angle  $\phi$  should be known.

If the deformation coefficient is defined as follows,

$$\xi = a_{ch} / a_c, \quad (9)$$

where the  $a_{ch}$  is the thickness of chip and  $a_c$  is the depth of cut. Then, the shear angle can be calculated as follows,

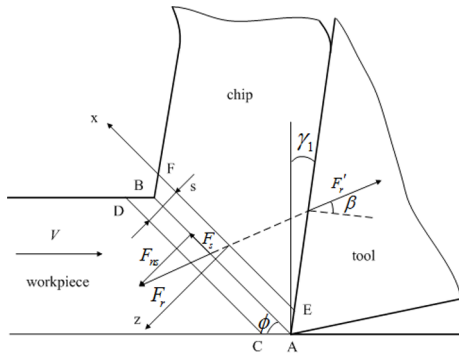


Fig. 5. Coordinate and cutting force

$$tg\phi = \frac{\cos\gamma_1}{\xi - \sin\gamma_1} \quad (10)$$

The thickness of chip usually decreases with the increase of cutting speed, so the deformation coefficient  $\xi$  decreases with the increase of cutting speed (Fig. 6), and it will be close to 1 when the cutting speed is higher because the thickness of chip is impossible less than depth of cut under the condition of continuous chip is produced. Our work [31] on the experiment of hardened AISI 1045 steel and the work of Komanduri and Von Turkovich [32] on Ti6Al4V demonstrated this phenomenon. Therefore, the deformation coefficient is assumed as 1 in this paper, and the shear angle  $\phi$  can be calculated by Eq. (10).

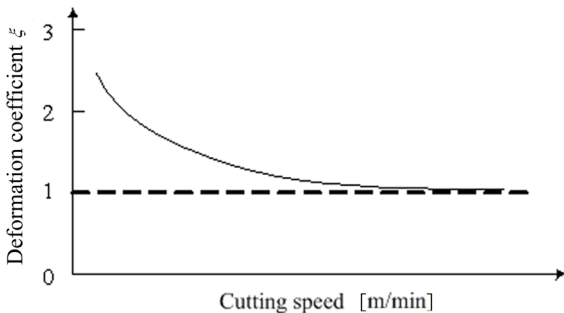


Fig. 6. Change of deformation coefficient with cutting speed

For the width of the primary shear zone, the study of Oxley and Hastings [33] shows that the ratio of it and the length of shear plane is 5.9 for carbon steel; thus, there is,

$$s = a_c / (5.9 \sin\phi) \quad (11)$$

The distribution of strain can be acquired by integrating the distribution of strain rate (Eq. (7)) and the result is,

$$\gamma(z) = \frac{8a(z-s/2) + \sqrt{(z-s/2)^2 + (s/2)^2}}{s^2 \sqrt{(z-s/2)^2 + (s/2)^2}} \quad (12)$$

On the shear plane AB,  $z=s/2$ , we get the strain of AB plane as follow,

$$\gamma_{AB} = \frac{1}{2} \frac{\cos\gamma_1}{\sin\phi \cos(\phi - \gamma_1)} \quad (13)$$

The distribution of temperature in the primary shear zone can be obtained through the method of non-uniform volume moving heat source, the detail of this method can be found in reference [34]. According to this method, the temperature of AB plane can be obtained by:

$$T_{AB} = T_0 + \frac{\tau(z)}{\rho c V \sin\phi} \int_0^{s/2} R(z) \dot{\gamma}(z) dz, \quad (14)$$

where  $T_0$  is the ambient temperature,  $\tau(z)$  is the shear stress, and it can be calculated by the constitutive relationship  $\tau(z) = f(\gamma(z), \dot{\gamma}(z), T(z))$ .  $R(z)$  is the coefficient of heat transmission, which can be calculated with the temperature at the same time.

According to the relationship between the cutting force and the shear angle in Fig. 7, it can be seen that,

$$F_r = \frac{F_s}{\cos(\phi + \beta - \gamma_1)} = \frac{\tau A_c}{\sin\phi \cos(\phi + \beta - \gamma_1)}, \quad (15)$$

and

$$F_{ns} = F_r \sin(\phi + \beta - \gamma_1) \quad (16)$$

Thus, the compression stress can be expressed as follows:

$$\begin{aligned} \sigma &= \frac{F_{ns}}{A_s} = \frac{F_r \sin(\phi + \beta - \gamma_1) \sin\phi}{A_c} = \\ &= \tau \cdot tg(\phi + \beta - \gamma_1). \end{aligned} \quad (17)$$

According to Merchant's formula of shear angle, there is,

$$\phi + \beta - \gamma_1 = \pi / 4. \quad (18)$$

Therefore, the expression of compression stress becoming,

$$\sigma_{AB} = \tau_{AB}, \quad (19)$$

where  $\tau_{AB} = f(\gamma_{AB}, \dot{\gamma}_{AB}, T_{AB})$  and can be calculated by a constitutive relationship.

### 3 INFLUENCE OF CUTTING PARAMETERS ON ADIABATIC SHEAR IN HSM

Now, the influence of cutting parameters on adiabatic shear in HSM can be analysed based on the model proposed. Where AISI 1045 steel is taken as an example and its constitutive relationship is expressed by the Johnson-Cook model, considering that the  $\tau = \sigma / \sqrt{3}$  and  $\gamma = \sqrt{3}\epsilon$ , its expression is as follows,

$$\tau = \frac{1}{\sqrt{3}} \left[ \bar{A} + \bar{B} \left( \frac{\dot{\gamma}}{\dot{\gamma}_r} \right)^n \right] \left[ 1 + \bar{C} \ln \left( \frac{\dot{\gamma}}{\dot{\gamma}_r} \right) \right] \left[ 1 - (T^*)^m \right], \quad (20)$$

where  $\bar{A}, \bar{B}, \bar{C}, n$  and  $m$  are parameters of constitutive relationship and their value are shown in Table 1 [35],  $\dot{\gamma}_r$  is the reference strain rate.  $T^* = (T - T_r) / (T_m - T_r)$  is the homogenization temperature,  $T_r$  is room temperature and  $T_m$  is melting point. The density of AISI 1045 steel is 7860 kg/m<sup>3</sup>, and its melting point is 1460 °C. The heat capacity and thermal conductivity are functions of temperature and can be calculated by,

$$c [\text{Jkg}^{-1}\text{K}^{-1}] = 420 + 0.504T [^\circ\text{C}], \quad (21)$$

$$k [\text{Wm}^{-1}\text{K}^{-1}] = 45.48 - 0.0203T [^\circ\text{C}]. \quad (22)$$

**Table 1.** Parameters of J-C constitutive relation for AISI 1045 steel

Constitutive parameters	$\bar{A}$ [MPa]	$\bar{B}$ [Mpa]	$\bar{C}$	$n$	$m$
value	553.1	600.8	0.0134	0.234	1

The influences of cutting parameters, including cutting speed, depth of cut, and rake angle, are analysed. Each time one parameter is changed to study its effect while others are fixed and the results are shown in Fig. 7. Fig. 7a gives the influence of cutting speed on adiabatic shear. It can be seen that the adiabatic shear will occur when the cutting speed is larger. The influence of depth of cut is similar with that of cutting speed, as shown in Fig. 7b. Fig. 7c indicates that the adiabatic shear will appear easier when the rake angle is smaller. At the same time, the influence of cutting speed is the biggest, the influence of depth of cut is the second, and that of rake angle is the least. The influence mechanism of these phenomena will be discussed in Section 5.

### 4 EXPERIMENT VALIDATION

An orthogonal cutting experiment was carried out for the validation of the prediction results. The work-piece is a cylindrical tube of AISI 1045 steel with an

inside diameter of 151.75 mm and thickness of 2.5 mm. Fig. 8 shows the experiment device. A cemented carbides YT15 cutting tool (TCMT110204 insert and STFCR1616H11 holder) was adopted. The experiment was done on a CA6140 lathe by dry cutting. The tool was replaced after each experiment for keeping the tool sharp. The range of cutting speed of  $V = 48.7$  m/min to 480.7 m/min, three depths of cut of  $a_c = 0.11$  mm,  $a_c = 0.15$  mm and  $a_c = 0.2$  mm; three rake angles of  $\gamma_1 = 10^\circ$ ,  $\gamma_1 = 0^\circ$ , and  $\gamma_1 = -10^\circ$  were selected as the cutting conditions.

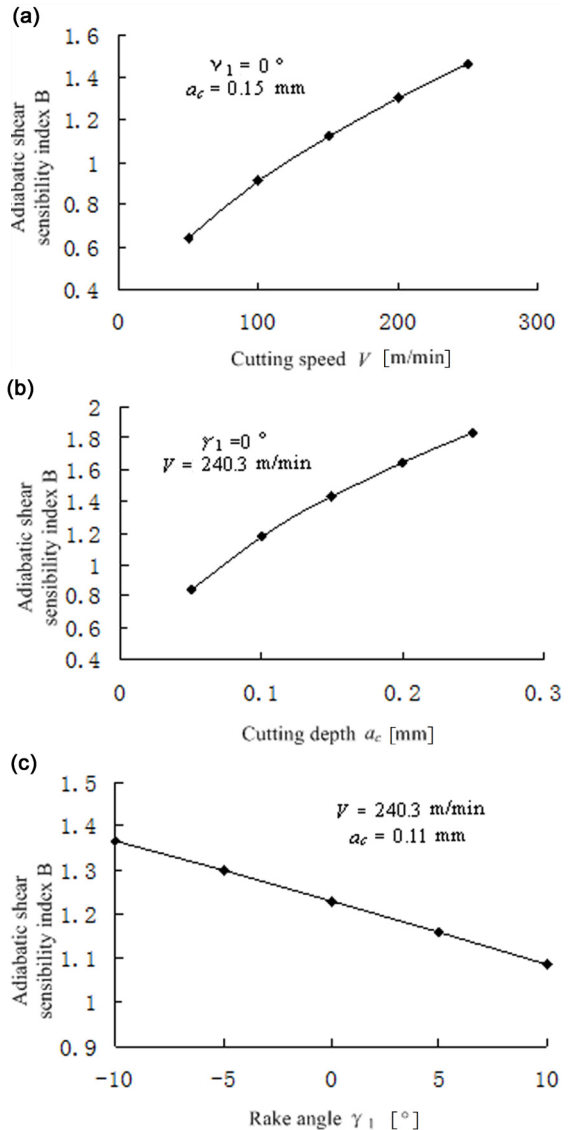


**Fig. 7.** Influence of cutting conditions on adiabatic shear in HSM: a) influence of cutting speed, b) influence of depth of cut, and c) influence of rake angle

The collected chip was fixed vertically in the admixture of epoxy resins and solidified agent (ratio

is 1:1) and then the samples (as shown in Fig. 9) were ground to the midsection of the chip. A Neuphot-II type optical microscope was used to observe the chip after grinding, polishing, and eroding.

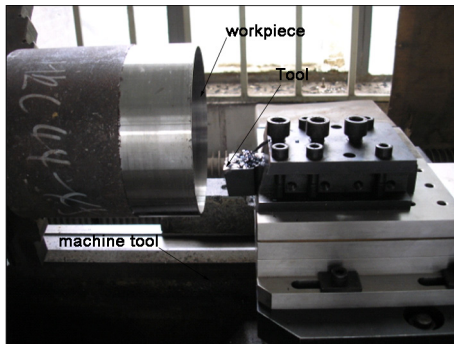


Fig. 8. Experiment device

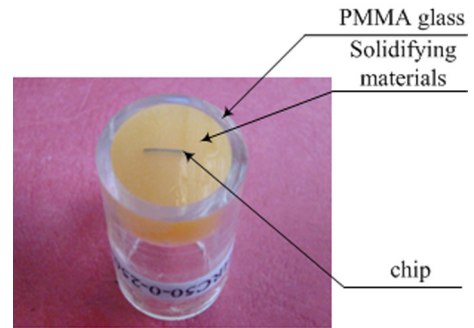


Fig. 9. Observation sample

The influences of cutting conditions on chip morphology are shown in Figs. 10 to 12. It is clear that larger cutting speed, greater depth of cut and smaller

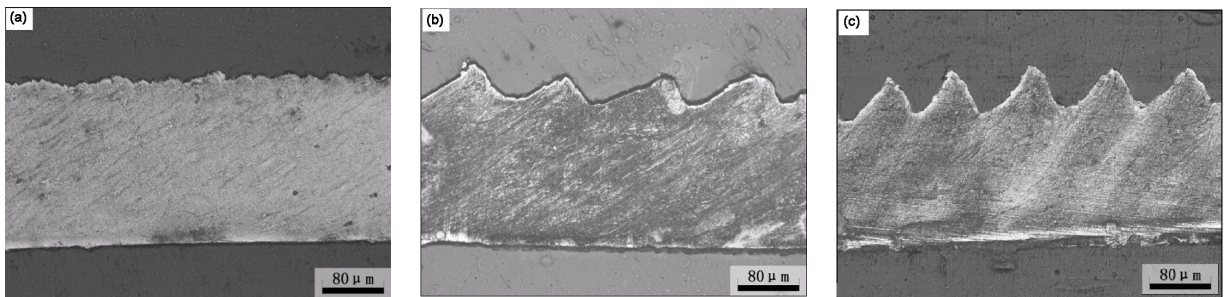


Fig. 10. Influence of cutting speed ( $\gamma_1 = 0^\circ$ ,  $a_c = 0.15$  mm: a)  $V = 96.1$  m/min, b)  $V = 151.4$  m/min, and c)  $V = 240.3$  m/min)

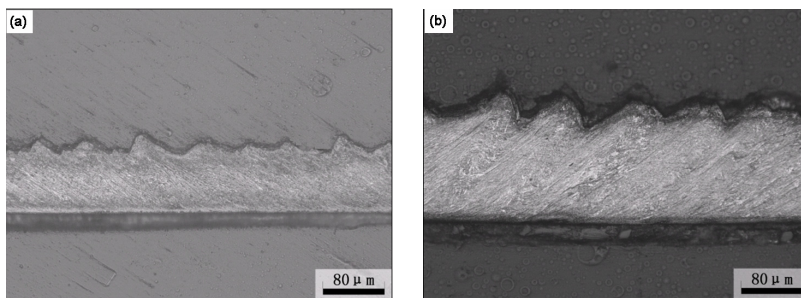


Fig. 11. Influence of depth of cut ( $\gamma_1 = 0^\circ$ ,  $V = 240.3$  m/min: a)  $a_c = 0.07$  mm, b)  $a_c = 0.11$  mm)

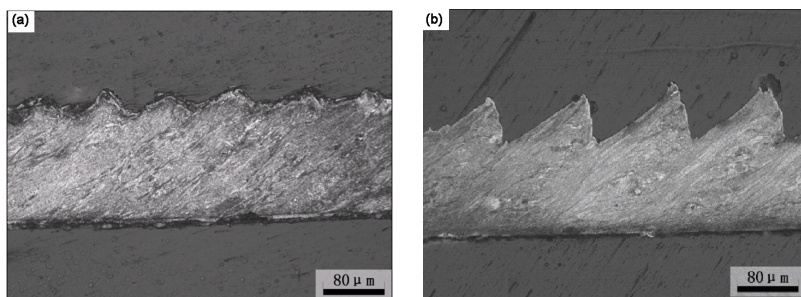


Fig. 12. Influence of rake angle ( $V = 240.3$  m/min,  $a_c = 0.11$  mm: a)  $\gamma_1 = 10^\circ$ , b)  $\gamma_1 = -10^\circ$ )

rake angle will promote the occurrence of adiabatic shear and lead to the forming of serrated chips. These are consistent with the analysis results and show the effectiveness of the proposed model.

### 5 DISCUSSION

The adiabatic shear localization under simple shear is usually explained by the theory of thermoplastic instability (Fig. 13), namely that the competition between strain hardening and thermal softening controls the occurrence of adiabatic shear. When strain hardening exceeds thermal softening, the plastic deformation is steady. Otherwise, the plastic deformation is unstable and the further plastic deformation occurs at smaller stresses until fracture.

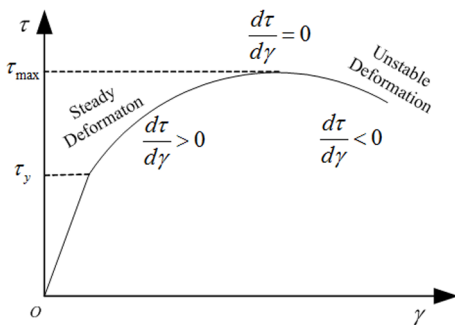


Fig. 13. Thermoplastic instability curve

The influence of cutting parameters on adiabatic shear can be explained by the proposed model. According to Eq. (6), the influence of strain and strain rate on adiabatic shear easily can be explained easily. The results are shown in Fig. 14.

According to Eqs. (8) and (13), the strain rate increases with the increase of cutting speed and the strain decreases with the increase of rake angle. Therefore, the adiabatic shear in machining occurs under the condition of larger cutting speed and smaller rake angle. These influence also can be explained by the above thermoplastic instability theory.

The influence of depth of cut is difficult to explain with the existing theory. Because as the depth of cut increases, the strain decreases according to the cutting theory, and the strain rate also decreases according to Eqs. (8) and (11). According to the theory of thermoplastic instability, the adiabatic shear should occur under smaller depths of cut. This is in conflict with the experiment result. From Fig. 13, it can be seen that in the zone of unstable plastic deformation, the stress increases with the decrease of strain. According to proposed model (Eq. (6)), this

will lead to the increase of adiabatic shear sensitivity index *B*, which means the adiabatic shear will occur under larger depths of cut.

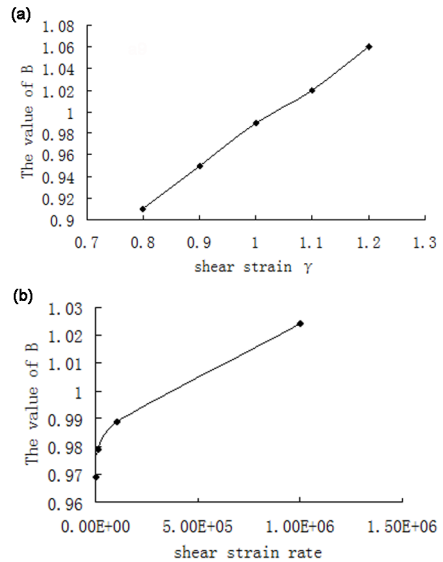


Fig. 14. Influences of deformation conditions on adiabatic shear: a) influence of strain, and b) influence of strain rate

The existing research on adiabatic shear in machining mostly focuses on the influence of cutting speed. Using the proposed model in this paper, not only can the system analysis of the influence of cutting parameters (including cutting speed, depth of cut and rake angle) on adiabatic shear be conducted but a reasonable explanation for these influences can also be given.

Furthermore, researches show that the evolution of adiabatic shear leads to the change of serrated chip, from partial to complete separation. This change will lead to the reduction of tool life, degradation of the machined surface integrity and the reduction of part accuracy. As mentioned in Section 1, the value of adiabatic shear sensitivity index *B* reflects the degree of adiabatic shear evolution. The relationship between cutting conditions and adiabatic shear sensitivity index *B* is also established. If the relationship between the evolution of adiabatic shear and the tool life, or machined surface integrity, etc., can be revealed in the future, the optimization of cutting parameters can be realized by combining the proposed model. Therefore, the proposed model can not only deepen the understanding of adiabatic shear in HSM, but also in favour of the optimization of cutting parameters.

## 6 CONCLUSIONS

- Based on an adiabatic shear sensitivity index proposed by linear perturbation analysis which considers the pressure-shear condition in machining, the relationship of adiabatic shear and cutting conditions are built. The corresponding relation between the cutting conditions and the deformation conditions is established based on the model of parallel boundary shear zone. The proposed model is validated by experiments.
- The adiabatic shear in HSM tends to occur under the condition of higher cutting speed, greater cutting depth and smaller rake angle. Furthermore, the influence of cutting speed is the biggest, the influence of cutting depth is the second, and that of rake angle is the least.
- The proposed model not only can reveal the mechanism of adiabatic shear in high-speed cutting, but can also be used in the optimization of cutting parameters.

## 7 ACKNOWLEDGEMENT

This work is supported by the Innovation Team Training Plan of Tianjin Universities and colleges (Grant No. TD12-5043), Tianjin Science and Technology Innovation System and Platform Construction Plan (14TXGCCX00011), Tianjin Universities "Training Plan of Subject-Leading Personnel" (RC14-02), the project of excellent young teachers (RC14-17) and that of young scholar broad (201307760011). This work is also supported by National-Local Joint Engineering Laboratory of Intelligent Manufacturing Oriented Automobile Die & Mould.

## 8 REFERENCES:

- [1] Ai, X. (2003). *Technology of High Speed Machining*. National Defense Industry Press, Beijing, p. 1-5.
- [2] Barry, J., Byrne, G. (2002). The mechanisms of chip formation in machining hardened steel. *Journal of Manufacturing Science and Engineering*, vol. 124, no. 3, p. 528-535, DOI:10.1115/1.1455643.
- [3] Ye, G.G., Xue, S.F., Ma, W., Jiang, M.Q., Ling, Z., Tong, X.H., Dai, L.H. (2012). Cutting AISI 1045 steel at very high speeds. *International Journal of Machine Tools and Manufacture*, vol. 56, p. 1-9, DOI:10.1016/j.ijmactools.2011.12.009.
- [4] Vyas, A., Shaw, M.C. (1999). Mechanics of saw-tooth chip formation in metal cutting. *Journal of Manufacturing Science and Engineering*, vol. 121, no. 2, p. 163-172, DOI:10.1115/1.2831200.
- [5] Astakhov, V.P. (1964). *Geometry of Single-Point Turning Tools and Drills*. Springer London Ltd, London.
- [6] Recht, R.F. (1964). Catastrophic thermoplastic shear. *Journal of Applied Mechanics*, vol. 31, no. 2, p. 189-193, DOI:10.1115/1.3629585.
- [7] Komandui, R., Schroeder, T., Hazra J., von Turkovich, B.F., Flom, D.G. (1982). On the catastrophic shear instability in high-speed machining of an AISI4340 steel. *Journal of Engineering for Industry*, vol. 104, no. 2, p. 121-131, DOI:10.1115/1.3185807.
- [8] Davies, M.A., Burns, T.J., Evans, C.J. (1997). On the dynamics of chip formation in machining hard metals. *CIRP Annals*, vol. 46, no. 1, p. 25-30, DOI:10.1016/S0007-8506(07)60768-9.
- [9] Molinari, A., Musquar, C., Sutter, G. (2002). Adiabatic shear banding in high speed machining of Ti-6Al-4V: experiments and modeling. *International Journal of Plasticity*, vol. 18, no. 4, p. 443-459, DOI:10.1016/S0749-6419(01)00003-1.
- [10] Ma, W., Li, X.W., Dai, L.H., Ling, Z. (2012). Instability criterion of materials in combined stress states and its application to orthogonal cutting process. *International Journal of Plasticity*, vol. 30-31, p. 18-40, DOI:10.1016/j.ijplas.2011.09.003.
- [11] Sheikh-Ahmad, J.Y., Quarless, V., Bailey, J.A. (2004). On the role of micro-cracks on flow instability in low speed machining of CP titanium. *Machining Science and Technology*, vol. 8, no. 3, p. 415-430, DOI:10.1081/MST-200039867.
- [12] Sun, S., Brandt, M., Dargusch, M.S. (2009). Characteristics of cutting forces and chip formation in machining of titanium alloys. *International Journal of Machine Tools & Manufacturing*, vol. 49, no. 7-8, p. 561-568, DOI:10.1016/j.ijmactools.2009.02.008.
- [13] Huang, J., Kalaitzidou, K., Sutherland, J.W., Aifantis, E.C. (2011). Validation of a predictive model for adiabatic shear band formation in chips produced via orthogonal machining. *Journal of Mechanical Behavior of Materials*, vol. 18, no. 4, p. 243-264, DOI:10.1515/JMBM.2007.18.4.243.
- [14] Duan, C.Z., Zhang, L.C. (2012). Adiabatic shear banding in AISI 1045 steel during high speed machining: Mechanisms of microstructural evolution. *Materials Science and Engineering: A*, vol. 532, p. 111-119, DOI:10.1016/j.msea.2011.10.071.
- [15] Molinari, A., Soldani, X., Miguélez, M.H. (2013). Adiabatic shear banding and scaling laws in chip formation with application to cutting of Ti-6Al-4V. *Journal of the Mechanics and Physics of Solids*, vol. 61, no. 11, p. 2331-2359, DOI:10.1016/j.jmps.2013.05.006.
- [16] Miguélez, M.H., Soldani, X., Molinari, A. (2013). Analysis of adiabatic shear banding in orthogonal cutting of Ti alloy. *International Journal of Mechanical Sciences*, vol. 75, p. 212-222, DOI:10.1016/j.ijmecsci.2013.06.011.
- [17] Gu, L.Y., Wang, M.J., Duan, C.Z. (2013). On adiabatic shear localized fracture during serrated chip evolution in high speed machining of hardened AISI 1045 steel. *International Journal of Mechanical Sciences*, vol. 75, p. 288-298, DOI:10.1016/j.ijmecsci.2013.07.004.
- [18] Gu, L.Y., Kang, G.Z., Chen, H., Wang, M.J. (2016). On adiabatic shear fracture in high-speed machining of martensitic-precipitation-hardening stainless steel. *Journal of Materials Processing Technology*, vol. 234, p. 208-216, DOI:10.1016/j.jmatprotec.2016.03.010.

- [19] Ye, G.G., Xue, S.F., Jiang, M.Q. (2013). Modeling periodic adiabatic shear band evolution during high speed machining Ti-6Al-4V alloy. *International Journal of Plasticity*, vol. 40, p. 39-55, DOI:10.1016/j.ijplas.2012.07.001.
- [20] Ye, G.G., Chen, Y., Xue, S.F., Dai, L.H. (2014). Critical cutting speed for onset of serrated chip flow in high speed machining. *International Journal of Machine Tools & Manufacture*, vol. 86, p. 18-33, DOI:10.1016/j.ijmactools.2014.06.006.
- [21] Ye, G.G., Jiang, M.Q., Xue, S.F., Ma, W., Dai, L.H. (2017). On the instability of chip flow in high-speed machining. *Mechanics of Materials*, in press, p. 1-16, DOI:10.1016/j.mechmat.2017.02.006.
- [22] Wang, C.Y., Xie, Y.X., Zheng, L.J., Qin, Z., Tang, D., Song, Y. (2014). Research on the chip formation mechanism during the high-speed milling of hardened steel. *International Journal of Machine Tools & Manufacture*, vol. 79, p. 31-48, DOI:10.1016/j.ijmactools.2014.01.002.
- [23] Wu, H.B., To, S. (2015). Serrated chip formation and their adiabatic analysis by using the constitutive model of titanium alloy in high speed cutting. *Journal of Alloys and Compounds*, vol. 629, p. 368-373, DOI:10.1016/j.jallcom.2014.12.230.
- [24] Jomaa, W., Mechri, O., Lévesque, J., Songmene, V., Bocher, P., Gakwaya, A. (2017). Finite element simulation and analysis of serrated chip formation during high-speed machining of AA7075-T651 alloy. *Journal of Manufacturing Processes*, vol. 26, p. 446-458, DOI:10.1016/j.jmapro.2017.02.015.
- [25] Wang, B., Liu, Z.Q. (2014). Serrated chip formation mechanism based on mixed mode of ductile fracture and adiabatic shear. *Proceedings of the Institution of Mechanical Engineers, Part B: Journal of Engineering Manufacture*, vol. 228, no. 2, p. 181-190, DOI:10.1177/0954405413497941.
- [26] Wang, B., Liu, Z.Q. (2016). Evaluation on fracture locus of serrated chip generation with stress triaxiality in high speed machining of Ti6Al4V. *Materials and Design*, vol. 98, p. 68-78, DOI:10.1016/j.matdes.2016.03.012.
- [27] Wang, B., Liu, Z.Q. (2017). Acoustic emission signal analysis during chip formation process in high speed machining of 7050-T7451 aluminum alloy and Inconel 718 superalloy. *Journal of Manufacturing Processes*, vol. 27, p. 114-125, DOI:10.1016/j.jmapro.2017.04.003.
- [28] Li, G.H., Wang, M.J., Duan, C.Z. (2009). Adiabatic shear critical condition in the high-speed cutting. *Journal of Materials Processing Technology*, vol. 209, no. 3, p. 1362-1367, DOI:10.1016/j.jmatprotec.2008.03.050.
- [29] Thé, J.H.L., Scrutton, R.F. (1979). Stress-state in the shear zone during steady state machining. *Journal of Engineering for Industry*, vol. 101, no. 2, p. 211-216, DOI:10.1115/1.3439497.
- [30] Tay, A.O., Stevenson, M.G., de Vahl Davis, G., Oxley, P.L.B. (1976). Numerical method for calculating temperature distributions in machining, from force and shear angle measurements. *International Journal of Machine Tool Design & Research*, vol. 16, no. 4, p. 335-349, DOI:10.1016/0020-7357(76)90043-3.
- [31] Li, G.H., Wang, M.J., Duan, C.Z., (2011). Experimental Study of Adiabatic Shear Critical Conditions in Orthogonal Cutting of hardened 45 Steel. *Journal of Dalian University of Technology*, vol. 51, no. 4, p. 518-524.
- [32] Komanduri, R., Von Turkovich, B.F. (1981). New observation on the mechanism of chip formation when machining titanium alloys. *Wear*, vol. 69, no. 2, p. 179-188, DOI:10.1016/0043-1648(81)90242-8.
- [33] Oxley, P.L.B., Hastings, W.F. (1977). Predicting the strain rate in the zone of intense shear in which the chip is formed in machining from the dynamic flow stress properties of the work material and the cutting conditions. *Proceedings of the Royal Society A*, vol. A356, no. 1686, p. 395-410, DOI:10.1098/rspa.1977.0141.
- [34] Li, G.H., Wang, M.J. (2009). Calculating of the temperature distribution of primary shear zone in orthogonal high speed cutting based on the non-uniform volume moving heat source. *Materials Science Forum*, vol. 626-627, p. 105-110, DOI:10.4028/www.scientific.net/MSF.626-627.105.
- [35] Karpat, Y., Özel, T. (2005). Predictive analytical and thermal modeling of orthogonal cutting process-Part I: Predictions of tool forces, stresses, and temperature distributions. *Journal of Manufacturing Science and Engineering*, vol. 128, no. 2, p. 435-443, DOI:10.1115/1.2162590.

# Vsebina

## Strojniški vestnik - Journal of Mechanical Engineering

letnik 63, (2017), številka 11  
Ljubljana, november 2017  
ISSN 0039-2480

Izhaja mesečno

### Razširjeni povzetki (extended abstracts)

Simon Oman, Marko Nagode: Vijačna zveza prirobničnega konzolnega nosilca: porazdelitev delovne sile po vijakih	SI 93
Jozef Kuczmaszewski, Ireneusz Zagorski, Olga Gziut, Stanislaw Legutko, Grzegorz M. Krolczyk: Fragmentacija odrezkov pri rezkanju magnezijeve zlitine AZ91HP	SI 94
Eyup Bagci, Ercüment U. Yüncüoğlu: Vpliv strategije rezkanja na sile, stopnjo odvzema materiala, odklon orodja in površinske napake pri grobi obdelavi kompleksnih površin	SI 95
Jiangping Mei, Shenglong Xie, Haitao Liu, Jiawei Zang: Modeliranje in kompenzacija histerez pri pnevmatičnih umetnih mišicah po posplošenem modelu Prandtl-Ishlinskii	SI 96
Robert Panowicz, Marcin Konarzewski, Michał Trypolin: Analiza kriterijev za določanje TNT ekvivalenta	SI 97
Guohe Li, Yujun Cai, Houjun Qi, Meng Liu: Modeliranje odvisnosti med adiabatnim strigom in rezalnimi parametri v območju visokih rezalnih hitrosti	SI 98



# Vijačna zveza prirobničnega konzolnega nosilca: porazdelitev delovne sile po vijakih

Simon Oman\* – Marko Nagode

Univerza v Ljubljani, Fakulteta za strojništvo, Slovenija

Za spajanje nosilcev v jeklenih konstrukcijah se pogosto uporabljajo vijačni spoji. Ker je večina jeklenih konstrukcij obremenjena dinamično, se za spajanje posameznih delov navadno uporablja prednapeto vijačno zvezo. Pri prednapeti vijačni zvezi se zaradi ustvarjenega tlaka med spojnim površinama in koeficienta trenja med njima obremenitve prenašajo preko trenja. V takšni povezavi zdrsi navadno niso dovoljeni, kar pomeni, da mora biti ustvarjena sila trenja v najbolj neugodnem obremenitvenem primeru večja od tangencialne sile, ki zaradi zunanje obremenitve deluje na spoj. To se doseže s pravilno določitvijo potrebne sile prednapetja in posledično potrebnega momenta privitja posameznih vijakov v spoju. Poleg tangencialne sile lahko na spoj deluje tudi sila v normalni smeri stičnih površin, ki jo imenujemo delovna sila. Delovna sila povzroči zmanjšanje kontaktnega tlaka in posledično zmanjšanje sile trenja. Zaradi tega dejstva je pri določitvi sile prednapetja potrebno upoštevati tudi delovno silo. Delovna sila se pri prirobničnih konzolnih nosilcih, ki so obremenjeni upogibno, po posameznih vijakih spoja ne porazdeli enakomerno. Porazdelitev je odvisna od številnih parametrov pri čemer so najbolj pomembni: geometrija prirobnice, postavitve vijakov na prirobnici ter debelina oz. togost prirobnice. Za določitev delovne sile po posameznih vijakih prirobničnega konzolnega nosilca obstaja kar nekaj analitičnih metod, ki pa v določenih primerih niso dovolj natančne. V tem prispevku je zato predstavljena alternativna metoda za določitev delovne sile po posameznih vijakih takšnega prednapetega spoja. Za ovrednotenje predstavljene metode so rezultati obstoječih analitičnih metod primerjani z rezultati alternativne metode in rezultati dobljenimi s pomočjo metode s končnimi elementi (MKE).

Predstavljena metoda pri določitvi delovnih sil upošteva obliko in s tem togost nosilca, ki je navadno privarjen na prirobnico, ne upošteva pa togosti prirobnice. Temelji na enostavni ideji transformacije natezno tlačnih napetosti po prerezu nosilca na najbolj obremenjenem mestu (spoj s prirobnico) v dve nasproti usmerjeni normalni sili, katerih prijemališča so določena glede na ravnotežje momentov. Ena od sil prirobnico nosilca potiska k podpori, druga pa prirobnico vleče proč od podpore. Glede na velikost obeh sil in njuni prijemališči se nato glede na oddaljenost prijemališča od mesta vijakov določi delovna sila. Glede na predpostavko metode se delovna sila prerezoporedi le na vijake, ki so v coni nateznih napetosti nosilca. Po predpostavki metode nosilec v tlačni coni prirobnico pritiska ob podporo in zato vijaki, ki so v tej coni niso dodatno obremenjeni.

Primerjava rezultatov predstavljene alternativne metode, obstoječih analitičnih metod in MKE analize je napravljena na dveh primerih nosilca (IPE 120 profil in T-profil) ter dveh debelinah prirobnice (12 mm in 20 mm). Spoj prirobnice s podporo je v vseh primerih izveden z osmimi vijaki M16. Primerjava rezultatov kaže na precejšnje odstopanje rezultatov med posameznimi metodami. Izkaže se, da vse obstoječe metode predpostavljajo, da se največja delovna sila pojavi v vijakih, ki se nahajajo na skrajnem robu prirobnice. Rezultati alternativne metoda za razliko od obstoječih metod kažejo, da se največja sila pojavi v drugi vrsti vijakov, kar sovпада z rezultati MKE analize.

Za potrditev ustreznosti rezultatov je bil opravljen tudi eksperiment na primeru IPE 120 nosilca z identičnimi pogoji kot so bili upoštevani pri analitičnih izračunih in MKE analizi. Dobljeni eksperimentalni rezultati so zaradi relativno majhne dodatne sile na vijakih, ki nastane kot posledica zunanje obremenitve, nekoliko manj zanesljivi, vendar kažejo zelo podobno sliko kot rezultati MKE analize.

Glede na dobljene rezultate lahko zaključimo, da je predstavljena alternativna metoda za določitev delovne sile po vijakih, za primer obravnavanega prirobničnega konzolnega nosilca od analitičnih metod najbolj natančna. Pri tem je potrebno izpostaviti, da morajo biti za natančno določitev delovne sile izpolnjeni naslednji pogoji:

- vrednost sile prednapetja tako velika, da v okolici prepreči nastanek špranje med stičnima površinama,
- upogibna togost prirobnice mnogo manjša od aksialne togosti vijakov,
- upogibna togost podporne plošče mnogo večja od upogibne togosti prirobnice.

V primeru, da se pri dimenzioniranju takšnega spoja upošteva standarde in priporočila, so vsi zgoraj navedeni pogoji izpolnjeni in s tem predstavljena metoda uporabna.

**Ključne besede:** vijačna zveza, prirobnični spoj, delovna sila, prednapeti vijak, konstrukcijsko jeklo, MKE

# Fragmentacija odrezkov pri rezkanju magnezijeve zlitine AZ91HP

Jozef Kuczmaszewski<sup>1</sup> – Ireneusz Zagorski<sup>1</sup> – Olga Gziut<sup>1</sup> – Stanislaw Legutko<sup>2</sup> – Grzegorz M. Krolczyk<sup>3,\*</sup>

<sup>1</sup> Tehniška univerza v Lublinu, Fakulteta za strojništvo, Poljska

<sup>2</sup> Tehniška univerza v Poznaniu, Fakulteta za strojništvo in management, Poljska

<sup>3</sup> FTehniška univerza v Opolah, Fakulteta za strojništvo, Poljska

Glavni cilj eksperimentov je bila določitev varnih, a učinkovitih tehnoloških parametrov procesa istosmerne rezkanja. Članek obravnava korelacijo med količino različnih frakcij odrezkov ter parametri  $v_c$ ,  $f_z$  in cepilni kot  $\gamma_o$ . Poznavanje odvisnosti med omenjenimi parametri je izjemnega pomena za najboljšo uspešnost in varnost obdelovalnega procesa. Sekundarni cilj študije je analiza frakcij odrezkov, ki se oblikujejo pri rezkanju magnezijevih zlitin.

Fragmentacija odrezkov ni zaželena, saj lahko privede do nenadzorovanega vžiga manjših frakcij odrezkov med rezkanjem, kakor tudi do onesnaženja kinematičnih parov in delovnega prostora rezkalnega stroja. Standard ISO 3685:1993 priporoča razvoj sistema za razvrščanje odrezkov, ki bo uporaben za vsak realen proces rezkanja. Bistvo problema, ki je razdelan v tem članku, je določitev takšnih parametrov rezkanja, ki prinašajo minimalno količino prašne frakcije.

Uporabljen sta bila konstantna rezalna parametra: radialna globina reza  $a_e = 14$  mm in aksialna globina reza  $a_p = 6$  mm. V študiji so bili preučeni variabilni tehnološki parametri procesa rezkanja:  $f_z = (0,05 \text{ do } 0,3)$  mm/zob,  $v_c = (400 \text{ do } 1200)$  m/min in cepilni kot  $\gamma_o = (5 \text{ do } 30)^\circ$ . Preizkusi so bili opravljeni z magnezijevo zlitino AZ91HP in s trdokovinskim stebelastim rezkarjem velikosti 16 mm.

Razvrstitev v glavne in vmesne frakcije je bila opravljena na podlagi oblike in velikosti odrezkov. 'Glavna frakcija' je frakcija A, 'vmesne frakcije' pa so manjše frakcije. V preizkusih so bili zbrani podatki o odstotnem deležu posameznih frakcij odrezkov pri različnih vrednostih rezalne hitrosti  $v_c$  in podajanja  $f_z$ .

Rezultati:

- Frakcij odrezkov je manj (fragmentacija je manjša) pri cepilnem kotu orodja  $\gamma_o = 30^\circ$ .
- Rezultati kažejo, da je treba uporabiti največjo možno globino reza in vrednost podajanja na zob (pod pogojem, da so izpolnjene kakovostne zahteve).
- Spremenljivost dimenzij odrezkov je neposredno povezana z dekohezijo (ločevanjem) obdelane plasti v obliki različnih glavnih in vmesnih frakcij odrezkov.

Raziskavo bi bilo treba razširiti še na ostale kakovosti magnezijevih zlitin, vključno z obdelovalnimi zlitinami, kot je AZ31. Rezultatov iz tega članka namreč ni mogoče neposredno ekstrapolirati na ostale kakovosti magnezijevih zlitin. Preučiti bi bilo treba tudi vpliv ostalih geometrijskih lastnosti (npr. kota vijačnice  $\lambda_s$ ) na stopnjo fragmentacije odrezkov. Čeprav rezultati kažejo, da rezalne hitrosti v preizkušenem območju (do 1200 m/min) ne privedejo do vžiga odrezkov, pa vselej velja, da je treba pri rezkanju magnezijevih zlitin poskrbeti za ustrezne varnostne postopke.

Avtorji so v članku osvetlili vplive rezalne hitrosti  $v_c$ , hitrosti podajanja  $f_z$  in cepilnega kota orodja  $\gamma_o$  na nastanek različnih frakcij odrezkov, odstotni delež posameznih frakcij odrezkov in celotne dimenzije odrezkov. Poleg tega so bile pod mikroskopom preučene morfološke lastnosti odrezkov.

Vnetljivost odrezkov magnezijevih zlitin je pomemben dejavnik pri rezkanju, ki je predmet mnogih študij in je relevanten za industrijo. Rezalne parametre, ki so opisani v članku, je mogoče uporabiti tudi v realnih aplikacijah. Pomemben prispevek članka je določitev odvisnosti med pogoji visokohitrostnega odrezavanja in nastalimi frakcijami odrezkov.

**Ključne besede:** visokohitrostno suho rezkanje, magnezijeve zlitine, odrezovalnost, magnezijevi odrezki, geometrija stebelastega rezkarja, kazalniki odrezovalnosti

# Vpliv strategije rezkanja na sile, stopnjo odvzema materiala, odklon orodja in površinske napake pri grobi obdelavi kompleksnih površin

Eyup Bagci\* – Ercüment U. Yüncüoğlu

Tehniška univerza Yıldız, Fakulteta za ladjedelništvo in pomorstvo, Turčija

Visokozmogljiva obdelava ukrivljenih površin je izjemno pomembna za sodobno industrijo. Proizvajalci so zato razvili različne metode in orodja CAM za izboljšanje učinkovitosti pri rezkanju oblikovnih površin. Določitev primernih strategij poti orodja in parametrov rezkanja je ključna za visoko produktivnost, boljšo hrapavost površine, manjše rezalne sile, odklon orodja in površinske napake.

Cilj predstavljene raziskave je analiza vpliva strategij poti orodja na dinamični odklon orodja, rezalne sile, čas obdelave, efektivni premer rezkarja (ECD), površino stika med rezkarjem in obdelovancem (CWE), trenutno stopnjo odvzema materiala (IMRR) in napake pri grobi obdelavi oblikovnih površin. Vrednosti ECD, CWR in IMRR v vsaki točki rezkarja (CL) so bile pridobljene s simulacijskim sistemom B-rep. Meritve dinamičnega odklona rezkarja so bile opravljene z dvema natančnima induktivnima senzorjema pomika, ki sta bila zamaknjena za 90°.

Sistem za simulacijo in optimizacijo B-rep je bil razvit in integriran s komercialno programsko opremo CAD/MCA za triosno rezkanje s stebelastimi rezkarji. Proces odrezavanja je bil simuliran s polnimi modeli obdelovanca, surovca in rezkarja, ustvarjenimi s pomočjo funkcij za modeliranje v komercialnem sistemu CAD/CAM, in potni orodja, ustvarjenimi v programu za CAM, ki je del istega sistema. Rezultati eksperimentov jasno prikazujejo vpliv strategij poti rezkarja na čas obdelave in njihov pomen pri skrajševanju časa in posledično zmanjševanju stroškov obdelave. Pri rezkanju s stebelastim rezkarjem se vrednosti globine reza, ECD in IMRR spreminjajo v vsaki točki rezkarja, zato na obdelani površini nastajajo različne oblikovne napake.

Uporabljene so bile različne cik-cak, profilne in spiralne strategije poti orodja. Poleg treh poti orodja je bila uporabljena tudi strategija cik-cak s šestimi različnimi rezalnimi koti. Vsakič je bilo uporabljeno konstantno podajanje 3 mm, vrednosti hitrosti vretena, podajanja in globine reza pa so znašale 600 vrt/min., 96 mm/min in 0,08 mm. Ker je bila primerjava strategij opravljena pri enakih pogojih obdelave, je eden od razlogov za spreminjanje rezalne sile pri različnih strategijah stična površina med orodjem in odrezkom. Najmanjše rezalne sile, odklon orodja in napake na površini so bili ugotovljeni pri strategiji cik-cak s kotom 90°. Največja napaka površine je bila ugotovljena pri profilni poti orodja in strategiji cik-cak s kotom 45°, rezalne sile, odkloni in napake oblike pa so sorazmerni.

Vrednosti odstranjenega volumna na zob in točke CL so bile izračunane s simulacijskim sistemom B-Rep. Izračun sil na podlagi količine odrezkov je zelo pomemben za točno ugotavljanje vrednosti IMRR pri grobi obdelavi. Narejena je bila primerjava sil pri rezkanju, ki so bile ugotovljene eksperimentalno, in vrednosti IMRR iz simulacije B-rep. Vrednost IMRR se povečuje praktično enako kot sile pri rezkanju. Ugotovljeno je bilo, da se profili odklona, vrednosti IMRR, rezalne sile, napake pri obdelavi in vrednosti ECD dobro ujemajo pri različnih strategijah obdelave. Hišni sistem za simulacijo NC se je dobro izkazal pri določanju velikosti in položaja oblikovnih napak na površini. Operaterji in tehnologi bodo tako lahko bolje vrednotili proces rezkanja za izbiro učinkovite strategije poti orodja.

**Ključne besede:** rezkanje, površine proste oblike, stopnja odvzema materiala, napake pri obdelavi, odklon, strategija obdelave

# Modeliranje in kompenzacija histerez pri pnevmatičnih umetnih mišicah po posplošenem modelu Prandtl-Ishlinskii

Jiangping Mei – Shenglong Xie – Haitao Liu\* – Jiawei Zang

Ministrstvo za šolstvo, Univerza v Tianjinu, Državni laboratorij za teorijo mehanizmov in konstrukcijo, Kitajska

Pnevmatične umetne mišice (PAM) so s svojim velikim razmerjem med močjo in maso ter dobro podajnostjo pritegnile veliko pozornosti tako v industriji kot v akademskih krogih. Inherentne nelinearnosti v obliki histerez (sila/dolžina, dolžina/tlak) pri PAM pomembno vplivajo na točnost krmiljenja gibanja po trajektoriji in v zadnjih letih je bilo zato opravljenih veliko študij za odpravo negativnih vplivov histerez. Modele histerez pri PAM je v grobem mogoče razdeliti v modele na podlagi operatorjev in modele na podlagi diferencialnih enačb. Modeli iz prve skupine, kot so modeli Preisach, Prandtl-Ishlinskii (PI) in Maxwell-Slip, uporabljajo za karakterizacijo histerez različne matematične operatorje. V drugo skupino modelov na podlagi diferencialnih enačb spadajo modeli Duhem, LuGre, Bouc-Wen in drugi. Najbolj razširjen je model PI, saj ima prednost omejenega števila elementov in analitične inverzije. Omeniti je treba, da klasični model PI ne omogoča popisa asimetričnih lastnosti histereze in nasičenja zaradi simetričnosti linearnih operatorjev zračnosti. Za razrešitev tega problema se intenzivno preučujejo asimetrični pristopi k modeliranju histerez, še posebej za pametne materiale, feromagnetne materiale in pametne aktuatorje. Le nekaj raziskav pa osvetljuje učinkovitost uporabe modela PI pri PAM.

Članek obravnava posplošen model Prandtl-Ishlinskii (GPI) in njegov inverzni model za popis asimetrične histereze dolžina/tlak pri PAM. Predlagani model GPI za razliko od klasičnega modela Prandtl-Ishlinskii (CPI) uporablja hiperbolično tangentno funkcijo kot ovojnično funkcijo posplošenih operatorjev zračnosti za karakterizacijo asimetričnih histereznih zank, saj je omenjena funkcija primernejša za ta namen.

Pred eksperimentalno verifikacijo predlaganega modela GPI je treba opraviti identifikacijo parametrov, kar pa v tem primeru nikakor ni preprosto zaradi velikega števila dimenzij, močne nelinearnosti in več omejitev. Za reševanje problema identifikacije parametrov pri modelih histereze je bilo razvitih več algoritmov, kot so optimizacija z rojem delcev, genetski algoritmi, evolucijska strategija s prilagojeno kovariančno matriko idr. V tem članku je bila za identifikacijo parametrov modela GPI uporabljena metoda Levenberg-Marquardt z iskanjem minimuma kvadratne stroškovne funkcije, s katero je identifikacija prikladnejša in učinkovitejša. Rezultati identifikacije parametrov kažejo, da je model GPI primeren za karakterizacijo velikih in malih asimetričnih histereznih zank dolžina/tlak pri PAM.

Za kompenzacijo histereze dolžina/tlak je bila razvita strategija krmiljenja z upoštevanjem motnje in povratno zanko, ki omogoča krmiljenje PAM po trajektoriji z veliko točnostjo. Zasnovan je bil kompenzator z upoštevanjem motnje na podlagi inverznega modela GPI, ki zmanjšuje vpliv histereze dolžina/tlak. Inverzni model GPI preslika želeno trajektorijo v vhodni krmilni signal za proporcionalni tlačni regulator in na ta način je linearizirana odvisnost med želeno trajektorijo in dejansko dolžino. Ker točnost modela histereze vpliva na uspešnost krmilnika z upoštevanjem motnje, je bila krmilniku dodana povratna zanka za zmanjšanje napake sledenja, ki jo povzročajo vibracije in lezenje. Iz rezultatov eksperimentov sledi sklep, da predlagani model GPI in njegov inverz učinkovito kompenzirata vplive histereze dolžina/tlak pri realnočasovnih aplikacijah. Ker pa je v posplošenem operaterju zračnosti uporabljena simetrična ovojnična funkcija, je sposobnost tega modela za karakterizacijo asimetričnih histereznih zank omejena. Krmilnik s povratno zanko v kombinaciji s kompenzatorjem z upoštevanjem motnje na podlagi asimetričnega modela GPI bo zato predmet prihodnjih raziskav, s ciljem dodatnega izboljšanja krmiljenja po trajektoriji.

**Ključne besede:** pnevmatična umetna mišica (PAM), nelinearnost zaradi histereze, posplošeni model Prandtl-Ishlinskii (GPI), krmiljenje po trajektoriji, metoda Levenberg-Marquardt, identifikacija parametrov

## Analiza kriterijev za določanje TNT ekvivalenta

Robert Panowicz\* – Marcin Konarzewski – Michał Trypolin

Tehniška vojaška univerza, Oddelek za strojništvo, Poljska

Napovedovanje pojavov z numerično analizo je vedno povezano z določenimi izzivi. Pri modeliranju obtežbe konstrukcij zaradi udarnih valov tako poseben izziv predstavljata določanje oblike tlačnega impulza in izbira metode za opis njegovega vpliva na konstrukcijo. Pri določanju parametrov udarnega vala se najpogosteje uporablja programska oprema ConWep (angl. *Conventional Weapon Effects*, učinki klasičnih orožij), ki deluje na podlagi eksperimentalno določenih odvisnosti. Težave nastopijo, kadar eksplozivna snov ni TNT ali kadar polnitev ni sferične oblike, saj v ConWep-u ni ustreznih podatkov. Pri simulacijah drugih eksplozivnih snovi se zato uporablja t. i. TNT ekvivalent oz. masa TNT-ja, ki bi povzročila enakovreden udarni val. Na voljo je več metod za računanje TNT ekvivalenta, nobena od njih pa ni dokončna. V članku so preverjene različne metode za določanje TNT ekvivalenta za določitev najnatančnejše metode za prihodnjo rabo.

Z enačbami za določitev TNT ekvivalenta, ki so opisane v študiji, je bila določena masa polnitev TNT-ja za numerično analizo ConWep. V naslednjem koraku so bili primerjani numerični rezultati simulacije odklona balističnega nihala zaradi delovanja udarnega vala po dveh metodah. Prva metoda, ki je validirana in uporabljena kot referenčna metoda, uporablja ALE s pristopom FSI. Druga, aproksimativna metoda uporablja pristop ConWep s predhodno določeno maso TNT-ja. Numerična analiza je bila opravljena po metodi končnih elementov z eksplicitno integracijo. Avtorji so v ta namen uporabili programsko opremo LS-Dyna. Numerična analiza je bila opravljena za eksplozivno polnitev kroglaste in valjaste oblike z maso 50 g, oddaljenost eksploziva od nihala pa je bila od 25 cm do 45 cm. Pred analizo je bila opravljena validacija numeričnega modela balističnega nihala, ustvarjenega s pomočjo ALE in pristopa FSI. Ugotovljeno je bilo dobro ujemanje z rezultati eksperimentov. Sprednji del nihala je bil med eksperimentom dinamično obremenjen z udarnim valom, ki ga je povzročila detonacija eksploziva. V preizkusih je bil uporabljen eksploziv Semtex A1 cilindrične oblike z maso 50 g ter razmerjem med dolžino in premerom 1. Polnitve so bile postavljene na lahko stojalo iz stiroporja na oddaljenosti 30 cm in 35 cm od nihala, merjeno od prednje plošče nihala do prednjega dela eksploziva.

Raztros vrednosti odklona nihala je bil v vseh obravnavanih primerih bistveno večji pri manjših kot pri večjih oddaljenostih. Preizkusi so pokazali, da je napaka ocene TNT ekvivalenta le pri metodi tlačnega impulza manjša od 20 %, kar se ujema z rezultati dela. Napaka je manjša takrat, ko je eksplozivna polnitev sferične oblike, v ostalih primerih pa je treba upoštevati, da se velikost napake začne pri 40 %. Največjo natančnost pri računanju TNT ekvivalenta torej ponuja omenjena metoda tlačnega impulza. Uporabniki morajo upoštevati, da gre še vedno le za grobo oceno vedenja eksploziva in da je zato treba računati z napakami.

**Ključne besede: TNT ekvivalent, ConWep, udarni val, eksploziv, ALE, MKE**

# Modeliranje odvisnosti med adiabatnim strigom in rezalnimi parametri v območju visokih rezalnih hitrosti

Guohe Li\* – Yujun Cai – Houjun Qi – Meng Liu

Tehniška in pedagoška fakulteta v Tianjinu, Državni laboratorij za visokohitrostno odrezavanje in natančno obdelavo, Kitajska

Visokohitrostna obdelava z odrezavanjem ponuja vrsto prednosti, kot so manjše rezalne sile, večja natančnost, kakovostnejša površina, večja produktivnost, manjši stroški in možnost obdelave težavnih materialov. Zato se je uveljavila v letalski in vesoljski industriji, v avtomobilski industriji in orodjarstvu, odpirajo pa se tudi vedno nove priložnosti za uporabo te tehnologije.

Glavna razlika med visokohitrotnim in konvencionalnim odrezavanjem je v obliki odrezkov: pri visokohitrotnem odrezavanju se tvorijo nazobčani, pri konvencionalnem odrezavanju pa tekoči odrezki. Večina raziskovalcev pripisuje oblikovanje nazobčenih odrezkov ponavljajočim se termoplastičnim nestabilnostim, še posebej pri duktilnih materialih. Pojav adiabatnega striga pri visokohitrotnem odrezavanju po eni strani povečuje obrabo orodja in vpliva na kakovost obdelane površine, po drugi strani pa prispeva k lomljenju odrezkov in je zato zaželen za obdelavo na avtomatih.

Za učinkovito upravljanje procesa odrezavanja je zato treba posvetiti več pozornosti lokalizaciji adiabatnega striga pri visokohitrostni obdelavi. Na osnovi indeksa občutljivosti adiabatnega striga iz linearne perturbacijske analize, ki upošteva strižne pogoje pri odrezavanju, je bila opredeljena odvisnost med adiabatnim strigom in rezalnimi parametri. Odvisnost med rezalnimi parametri in deformacijami je bila določena na podlagi modela vzporedne mejne strižne cone. Vpliv rezalnih parametrov na adiabatni strig je bil analiziran s spreminjanjem enega parametra, medtem ko so bili ostali parametri konstantni. Izkazalo se je, da adiabatni strig nastopa pri večjih rezalnih hitrostih, vpliv globine reza je podoben vplivu rezalne hitrosti, pojav adiabatnega striga pa je večji pri manjšem cepilnem kotu. Največji je vpliv rezalne hitrosti, na drugem mestu je vpliv globine reza in na tretjem mestu cepilni kot. Za validacijo predlaganega modela je bil opravljen eksperiment z ortogonalnim odrezavanjem, pri katerem je bilo opazovano spreminjanje morfologije odrezka z rezalnimi parametri.

Rezultati eksperimenta se ujemajo z rezultati analize in dokazujejo učinkovitost predlaganega modela. Podrobno je bil raziskan tudi mehanizem vpliva rezalnih parametrov na adiabatni strig. Po predlaganem modelu se hitrost preoblikovanja povečuje s povečevanjem rezalne hitrosti, raztezek pa se zmanjšuje s povečevanjem cepilnega kota. Adiabatni strig se tako pojavi v razmerah večje rezalne hitrosti in manjšega cepilnega kota. S povečevanjem globine reza se po teoriji odrezavanja zmanjšujejo raztezki, enako pa tudi hitrost deformacij. Napetosti v območju nestabilnih plastičnih deformacij se povečujejo z zmanjševanjem raztezkov. Po modelu se torej poveča indeks občutljivosti adiabatnega striga  $B$ , t. j. adiabatni strig se pojavi pri večji globini reza. Obstoječe raziskave adiabatnega striga pri obdelavi so osredotočene predvsem na vpliv rezalne hitrosti, predlagani model pa ne omogoča le systemske analize vpliva rezalnih parametrov (vključno z rezalno hitrostjo, globino reza in cepilnim kotom) na adiabatni strig, temveč jih tudi smiselno pojasnjuje. Vrednost indeksa občutljivosti adiabatnega striga  $B$  odraža stopnjo razvoja adiabatnega striga. Določena je tudi odvisnost med rezalnimi parametri in indeksom občutljivosti adiabatnega striga  $B$ .

Ko bodo razkrite še odvisnosti med razvojem adiabatnega striga in obstojnostjo orodja, integriteto obdelane površine itd., bo v kombinaciji s predlaganim modelom možna tudi optimizacija rezalnih parametrov in predlagani model tako ne pogloblja le razumevanja adiabatnega striga pri visokohitrotnem odrezavanju.

**Ključne besede:** visokohitrostno odrezavanje, adiabatni strig, nazobčan odrezek, linearna perturbacijska analiza, indeks občutljivosti, rezalni parameter

## DOKTORSKE DISERTACIJE

Na Fakulteti za strojništvo Univerze v Ljubljani je obranil svojo doktorsko disertacijo:

- dne 3. oktobra 2017 **Blaž STARC** z naslovom: »Modifikacija in posodabljanje kompleksnih sistemov v dinamiki podstruktur« (mentor: prof. dr. Miha Boltežar, somentor: doc. dr. Gregor Čepo);

Doktorska naloga predstavi numerično modeliranje dinamskih sistemov z metodami modalne sinteze komponent. Poudarek dela je na modeliranju enostranskih kontaktnih stanj in določevanju odziva reduciranega sistema tekom obratovanja. Na primeru kompleksne strukture je predstavljena primerjava štirih klasičnih metod modalne sinteze komponent. Uporaba metod omogoči razdelitev kompleksne strukture na reducirane podstrukture ter s tem hitrejšo identifikacijo vpliva strukturnih modifikacij na

dinamski odziv sistema. Izkazani rezultati prikazujejo tako učinkovitost uporabljenih metod kot tudi fizikalno konsistentnost, ki je bila potrjena na osnovi eksperimenta. Metode modalne sinteze komponent so uporabljene kot osnova za modeliranje odziva struktur s spreminjajočimi kontaktnimi pogoji. Skupaj z razvitim modelom variabilnega kontakta so definirane nove formulacije dogodkovnih integracijskih shem, ki omogočajo preklap med tremi možnimi stanji kontakta. Za vsako kontaktno stanje je prikazan postopek definicij reduciranih sistemskih matrik kot tudi postopek posodabljanja začetnih pogojev za izvedbo prehoda med reduciranim naborom gibalnih enačb. Učinkovitost predlagane formulacije je prikazana na realnem primeru, ki služi tudi za validacijo razvite numerične formulacije.

# Information for Authors

All manuscripts must be in English. Pages should be numbered sequentially. The manuscript should be composed in accordance with the Article Template given above. The maximum length of contributions is 10 pages. Longer contributions will only be accepted if authors provide justification in a cover letter. For full instructions see the Information for Authors section on the journal's website: <http://cn.sv-jme.eu>.

## SUBMISSION:

Submission to SV-JME is made with the implicit understanding that neither the manuscript nor the essence of its content has been published previously either in whole or in part and that it is not being considered for publication elsewhere. All the listed authors should have agreed on the content and the corresponding (submitting) author is responsible for having ensured that this agreement has been reached. The acceptance of an article is based entirely on its scientific merit, as judged by peer review. Scientific articles comprising simulations only will not be accepted for publication; simulations must be accompanied by experimental results carried out to confirm or deny the accuracy of the simulation. Every manuscript submitted to the SV-JME undergoes a peer-review process.

The authors are kindly invited to submit the paper through our web site: <http://ojs.sv-jme.eu>. The Author is able to track the submission through the editorial process - as well as participate in the copyediting and proofreading of submissions accepted for publication - by logging in, and using the username and password provided.

## SUBMISSION CONTENT:

The typical submission material consists of:

- A **manuscript** (A PDF file, with title, all authors with affiliations, abstract, keywords, highlights, inserted figures and tables and references),
- Supplementary files:
  - a **manuscript** in a WORD file format
  - a **cover letter** (please see instructions for composing the cover letter)
  - a ZIP file containing **figures** in high resolution in one of the graphical formats (please see instructions for preparing the figure files)
  - possible **appendices** (optional), cover materials, video materials, etc.

Incomplete or improperly prepared submissions will be rejected with explanatory comments provided. In this case we will kindly ask the authors to carefully read the Information for Authors and to resubmit their manuscripts taking into consideration our comments.

## COVER LETTER INSTRUCTIONS:

Please add a **cover letter** stating the following information about the submitted paper:

1. **Paper title**, list of **authors** and their **affiliations**.
2. **Type of paper**: original scientific paper (1.01), review scientific paper (1.02) or short scientific paper (1.03).
3. A **declaration** that neither the manuscript nor the essence of its content has been published in whole or in part previously and that it is not being considered for publication elsewhere.
4. State the **value of the paper** or its practical, theoretical and scientific implications. What is new in the paper with respect to the state-of-the-art in the published papers? Do not repeat the content of your abstract for this purpose.
5. We kindly ask you to suggest at least two **reviewers** for your paper and give us their names, their full affiliation and contact information, and their scientific research interest. The suggested reviewers should have at least two relevant references (with an impact factor) to the scientific field concerned; they should not be from the same country as the authors and should have no close connection with the authors.

## FORMAT OF THE MANUSCRIPT:

The manuscript should be composed in accordance with the Article Template. The manuscript should be written in the following format:

- A **Title** that adequately describes the content of the manuscript.
- A list of **Authors** and their **affiliations**.
- An **Abstract** that should not exceed 250 words. The Abstract should state the principal objectives and the scope of the investigation, as well as the methodology employed. It should summarize the results and state the principal conclusions.
- 4 to 6 significant **key words** should follow the abstract to aid indexing.
- 4 to 6 **highlights**: a short collection of bullet points that convey the core findings and provide readers with a quick textual overview of the article. These four to six bullet points should describe the essence of the research (e.g. results or conclusions) and highlight what is distinctive about it.
- An **Introduction** that should provide a review of recent literature and sufficient background information to allow the results of the article to be understood and evaluated.
- A **Methods** section detailing the theoretical or experimental methods used.
- An **Experimental section** that should provide details of the experimental set-up and the methods used to obtain the results.
- A **Results** section that should clearly and concisely present the data, using figures and tables where appropriate.
- A **Discussion** section that should describe the relationships and generalizations shown by the results and discuss the significance of the results, making comparisons with previously published work. (It may be appropriate to combine the Results and Discussion sections into a single section to improve clarity.)
- A **Conclusions** section that should present one or more conclusions drawn from the results and subsequent discussion and should not duplicate the Abstract.
- **Acknowledgement** (optional) of collaboration or preparation assistance may be included. Please note the source of funding for the research.
- **Nomenclature** (optional). Papers with many symbols should have a nomenclature that defines all symbols with units, inserted above the references. If one is used, it must contain all the symbols used in the manuscript and the definitions should not be repeated in the text. In all cases, identify the symbols used if they are not widely recognized in the profession. Define acronyms in the text, not in the nomenclature.
- **References** must be cited consecutively in the text using square brackets [1] and collected together in a reference list at the end of the manuscript.
- **Appendix(-ices)** if any.

## SPECIAL NOTES

**Units:** The SI system of units for nomenclature, symbols and abbreviations should be followed closely. Symbols for physical quantities in the text should be written in italics (e.g.  $v$ ,  $T$ ,  $n$ , etc.). Symbols for units that consist of letters should be in plain text (e.g.  $\text{ms}^{-1}$ ,  $\text{K}$ ,  $\text{min}$ ,  $\text{mm}$ , etc.). Please also see: <http://physics.nist.gov/cuu/pdf/sp811.pdf>.

**Abbreviations** should be spelt out in full on first appearance followed by the abbreviation in parentheses, e.g. variable time geometry (VTG). The meaning of symbols and units belonging to symbols should be explained in each case or cited in a **nomenclature** section at the end of the manuscript before the References.

**Figures** (figures, graphs, illustrations digital images, photographs) must be cited in consecutive numerical order in the text and referred to in both the text and the captions as Fig. 1, Fig. 2, etc. Figures should be prepared without borders and on white grounding and should be sent separately in their original formats. If a figure is composed of several parts, please mark each part with a), b), c), etc. and provide an explanation for each part in Figure caption. The caption should be self-explanatory. Letters and numbers should be readable (Arial or Times New Roman, min 6 pt with equal sizes and fonts in all figures). Graphics (submitted as supplementary files) may be exported in resolution good enough for printing (min. 300 dpi) in any common format, e.g. TIFF, BMP or JPG, PDF and should be named Fig1.jpg, Fig2.tif, etc. However, graphs and line drawings should be prepared as vector images, e.g. CDR, AI. Multi-curve graphs should have individual curves marked with a symbol or otherwise provide distinguishing differences using, for example, different thicknesses or dashing.

**Tables** should carry separate titles and must be numbered in consecutive numerical order in the text and referred to in both the text and the captions as Table 1, Table 2, etc. In addition to the physical quantities, such as  $t$  (in italics), the units [s] (normal text) should be added in square brackets. Tables should not duplicate data found elsewhere in the manuscript. Tables should be prepared using a table editor and not inserted as a graphic.

## REFERENCES:

A reference list must be included using the following information as a guide. Only cited text references are to be included. Each reference is to be referred to in the text by a number enclosed in a square bracket (i.e. [3] or [2] to [4] for more references; do not combine more than 3 references, explain each). No reference to the author is necessary.

References must be numbered and ordered according to where they are first mentioned in the paper, not alphabetically. All references must be complete and accurate. Please add DOI code when available. Examples follow.

## Journal Papers:

Surname 1, Initials, Surname 2, Initials (year). Title. Journal, volume, number, pages, DOI code.

- [1] Hackenschmidt, R., Alber-Laukant, B., Rieg, F. (2010). Simulating nonlinear materials under centrifugal forces by using intelligent cross-linked simulations. *Strojniški vestnik - Journal of Mechanical Engineering*, vol. 57, no. 7-8, p. 531-538, DOI:10.5545/sv-jme.2011.013.

Journal titles should not be abbreviated. Note that journal title is set in italics.

## Books:

Surname 1, Initials, Surname 2, Initials (year). Title. Publisher, place of publication.

- [2] Groover, M.P. (2007). *Fundamentals of Modern Manufacturing*. John Wiley & Sons, Hoboken.

Note that the title of the book is italicized.

## Chapters in Books:

Surname 1, Initials, Surname 2, Initials (year). Chapter title. Editor(s) of book, book title. Publisher, place of publication, pages.

- [3] Carbone, G., Ceccarelli, M. (2005). Legged robotic systems. Kordić, V., Lazinica, A., Merdan, M. (Eds.), *Cutting Edge Robotics*. Pro literatur Verlag, Mammendorf, p. 553-576.

## Proceedings Papers:

Surname 1, Initials, Surname 2, Initials (year). Paper title. Proceedings title, pages.

- [4] Štefanič, N., Martinčević-Mikić, S., Tošanović, N. (2009). Applied lean system in process industry. *MOTSP Conference Proceedings*, p. 422-427.

## Standards:

Standard-Code (year). Title. Organisation. Place.

- [5] ISO/DIS 16000-6.2:2002. *Indoor Air - Part 6: Determination of Volatile Organic Compounds in Indoor and Chamber Air by Active Sampling on TENAX TA Sorbent, Thermal Desorption and Gas Chromatography using MSD/FID*. International Organization for Standardization. Geneva.

## WWW pages:

Surname, Initials or Company name. Title, from <http://address>, date of access.

- [6] Rockwell Automation. Arena, from <http://www.arenasimulation.com>, accessed on 2009-09-07.

## EXTENDED ABSTRACT:

When the paper is accepted for publishing, the authors will be requested to send an **extended abstract** (approx. one A4 page or 3500 to 4000 characters). The instruction for composing the extended abstract are published on-line: <http://www.sv-jme.eu/information-for-authors/>.

## COPYRIGHT:

Authors submitting a manuscript do so on the understanding that the work has not been published before, is not being considered for publication elsewhere and has been read and approved by all authors. The submission of the manuscript by the authors means that the authors automatically agree to transfer copyright to SV-JME when the manuscript is accepted for publication. All accepted manuscripts must be accompanied by a Copyright Transfer Agreement, which should be sent to the editor. The work should be original work by the authors and not be published elsewhere in any language without the written consent of the publisher. The proof will be sent to the author showing the final layout of the article. Proof correction must be minimal and executed quickly. Thus it is essential that manuscripts are accurate when submitted. Authors can track the status of their accepted articles on <http://cn.sv-jme.eu>.

## PUBLICATION FEE:

Authors will be asked to pay a publication fee for each article prior to the article appearing in the journal. However, this fee only needs to be paid after the article has been accepted for publishing. The fee is 240.00 EUR (for articles with maximum of 6 pages), 300.00 EUR (for articles with maximum of 10 pages), plus 30.00 EUR for each additional page. The additional cost for a color page is 90.00 EUR. These fees do not include tax.

Strojniški vestnik - Journal of Mechanical Engineering  
Aškerčeva 6, 1000 Ljubljana, Slovenia,  
e-mail: [info@sv-jme.eu](mailto:info@sv-jme.eu)



<http://www.sv-jme.eu>

# Contents

## Papers

- 617 Simon Oman, Marko Nagode:  
**Bolted Connection of an End-Plate Cantilever Beam:  
The Distribution of Operating Force**
- 628 Jozef Kuczmaszewski, Ireneusz Zagorski, Olga Gziut, Stanislaw Legutko,  
Grzegorz M. Krolczyk:  
**Chip Fragmentation in the Milling of AZ91HP Magnesium Alloy**
- 643 Eyup Bagci, Ercüment U. Yüncüoğlu:  
**The Effects of Milling Strategies on Forces, Material Removal Rate,  
Tool Deflection, and Surface Errors for the Rough Machining  
of Complex Surfaces**
- 657 Jiangping Mei, Shenglong Xie, Haitao Liu, Jiawei Zang:  
**Hysteresis Modelling and Compensation of Pneumatic Artificial Muscles  
using the Generalized Prandtl-Ishlinskii Model**
- 666 Robert Panowicz, Marcin Konarzewski, Michał Trypolin:  
**Analysis of Criteria for Determining a TNT Equivalent**
- 673 Guohe Li, Yujun Cai, Houjun Qi, Meng Liu:  
**Modelling of the Relationship of Adiabatic Shear and Cutting Conditions  
for Higher Cutting Speed Ranges**